A MICROMECHANICAL COMPUTATIONAL FRAMEWORK FOR DYNAMIC FAILURE MECHANISMS IN POLYCRYSTALLINE MATERIALS AT HIGH STRAIN RATES

by

HAO JIANG

Submitted in partial fulfillment of the requirements

For the degree of Doctor of Philosophy

Thesis Adviser: Dr. Bo Li

Department of Mechanical and Aerospace Engineering

CASE WESTERN RESERVE UNIVERSITY

May, 2019

CASE WESTERN RESERVE UNIVERSITY

SCHOOL OF GRADUATE STUDIES

We hereby approve the dissertation of

HAO JIANG

Candidate for the degree of Doctor of Philosophy*.

Bo Li, Ph.D.
Committee Chair, Advisor
Department of Mechanical and Aerospace Engineering

Vikas Prakash, Ph.D.
Department of Mechanical and Aerospace Engineering

Ozan Akkus, Ph.D.
Department of Mechanical and Aerospace Engineering

John Lewandowski, Ph.D.
Department of Materials Science and Engineering

March 29, 2019

* We also certify that written approval has been obtained

for any proprietary material contained therein.

To my parents
To Boya and Alex

Table of Contents

List of Tables vi

List of Figures vii

Acknowledgements xvi

Acknowledgements xvi

Abstract xviii

Abstract xviii

Chapter 1. Introduction 1

Overview 1

Griffith's theory 8

Layout of the thesis 12

Chapter 2. Polycrystalline reconstruction 14

Voronoi tessellation 15

Grain boundary and voids 20

Orientation and misorientation 24

Chapter 3. Computational framework 29

Continuum mechanics 29

Constitutive model 34

Governing equations and the Optimal Transportation Meshfree (OTM) method 37

Fracture models 43

Chapter 4. Modeling dynamic failure of polycrystalline graphene under tension 53

Introduction 53

Critical energy release rate function 62

Comparison between MD simulation and continuum modeling 66

Influence of strain rate on the tensile strength 74

Chapter 5. Modeling dynamic failure of polycrystalline ceramic materials 81

Introduction 81

Simulations and results 85

Conclusion 117

Chapter 6. Conclusions and future works 119

Complete References 122

List of Tables

4.1	Material properties used in the graphene tensile test	68
4.2	Experimental data of critical fracture stress and Young's modulus for polycrystalline graphene with a pre-crack of length $0.6\mu m$	77
5.1	Parameters used in the SiC compression test	92

List of Figures

1.1 SEM images of SiC fracture surface after compression test. 2

1.2 Idealization of unloaded region near crack flanks. 9

1.3 The fracture energy balance. 10

2.1 Hot sintering process for manufacturing ceramic materials. SEM images show the common microstructures found in the sintered material. 15

2.2 An example of Voronoi tessellation: a) A cubic domain with 100 polyhedron (colored by Voronoi cells) b) Polyhedrons inside the domain. 16

2.3 A $1 \times 1 \times 1\ mm^3$ cube is divided by a) PVT and b) CVT. The Voronoi cell size distributions of a) and b) are plotted in c) and d), respectively. Note the Voronoi cell size is represented by the equivalent diameter of the cell. 19

2.4 The most regular tessellation in 3D space. 20

2.5 Grain size distributions with different regularity parameters. 21

2.6 3D reconstruction of polycrystalline structure: a) grain aggregation (colored by grain orientations) b) polycrystalline structure colored by the magnitude of misorientation angles and c) meshes for the grain boundaries (colored by the magnitude of misorientation angles). 22

2.7 Explicit representations of grain boundaries and other micro-defects(The grid of dots denotes the microstructure of the material while the dashed triangles denote the samples of the discretization in the model). 23

2.8 Grain orientation and grain boundary misorientation. The reference coordinates are in black and the crystal coordinates are in red. 25

2.9 Misorientation distribution before and after applying the Monte-Carlo annealing algorithm in comparison with the target distribution. 28

2.10 Grain boundaries colored by misorientation angles before and after applying the Monte-Carlo annealing algorithm. 28

3.1 Deformation mapping from the reference configuration Ω to the deformed configuration $\boldsymbol{\varphi}(\Omega)$. 31

3.2 Deformation in the crystal elasticity model using the rotation between crystal coordinates and spatial coordinates. 36

3.3 Schematic of the OTM approximation scheme, showing two successive configurations Ω_k and Ω_{k+1} of the domain, mapped by the incremental deformation mapping $\boldsymbol{\varphi}_{k\to k+1}$. The domain is modeled by material points(solid triangles) and nodes(empty circles), where the kinematic information of the body (e.g. displacements, velocities, and accelerations) is carried by the nodes $\mathbf{x}_{a,k+1}$ and the deformation and local state are evaluated at the material points $\mathbf{x}_{p,k+1}$. $N_H(\mathbf{x}_{p,k})$

represents the neighborhood of material point $\mathbf{x}_p$ at time t_k. Only nodes in the neighborhood of the material point $\mathbf{x}_p$ are used to approximate the strain at $\mathbf{x}_p$. 42

3.4 The irreversible interface cohesive law used in the cohesive element at the interface between triangular elements[128]. 44

3.5 Visualization of the ϵ-neighborhood(shadowed area) of the crack set A. Material points in the crack set are marked as black dots. Intact material points are presented as empty circles and grey dots, while the grey dots are in the ϵ-neighborhood of the material point p for calculating its equivalent energy release rate. The dash line shows the real crack trajectory. 50

4.1 Images of suspended graphene sheets used to measure its mechanical properties with an indenter. (A) SEM of a large graphene flake covering an array of circular holes $1mm$ and $1.5mm$ in diameter. Area I shows a hole partially covered by graphene, area II is fully covered, and area III is fractured from indentation. Scale bar, $3mm$. (B) AFM image of one membrane, $1.5mm$ in diameter. The solid line is a height profile along the dashed line. The step height at the edge of the membrane is about $2.5nm$. (C) Schematic of nanoindentation on the suspended graphene sheet. (D) AFM image of a fractured sheet[71]. 55

4.2 (a) SEM image showing the in situ tensile testing with a microdevice. Movement of the nanoindenter tip (shown by the block arrow) was converted to pure tension of the specimen on the sample stage by the inclined beams. Inset is the magnified image of the boxed region showing graphene across the gap of the sample stage. (b,c) SEM images showing graphene on the sample stage before and after tensile testing, respectively. The pre-crack (boxed in (b)) was cut by FIB. The scale bar in (b) and its inset is $5\mu m$ and $500nm$, respectively. (d) Selected engineering stress-strain curves of the cracked graphene samples (♯3 with crack size $518nm$ and ♯5 with crack size 1256 nm) [132]. 57

4.3 (A) Scheme of the experiment. PDMS, polydimethylsiloxane. (B) Side-view image of a moving μ-bullet taken by triple exposure at time steps t_1 to t_3. (C) MLG membrane on a sample holder after α-LIPIT. Three separate impact test regions are highlighted by green backlight. (D) Schematic illustration of penetration steps: (i) prepenetration stage; (ii) conic deformation stage; (iii) fracture stage; and (iv) postpenetration stage, showing the film morphology after penetration and relaxation. Scale bars in (B) and (C), 50 μm. [73] 59

4.4 Specific penetration energy of MLG, PMMA, and gold membranes compared with macroscopic materials at various impact velocities. The

density of each material is represented by a logarithmic color scale. Error bars denote SD.[73] 60

4.5 Molecular dynamic simulation of bi-crystal tensile test: a) a sample with a 20° misorientation angle under unloaded condition, b)-f) various stages of the crack growth at the corresponding strain levels(4.5%, 4.65%, 5%, 5.3%, and 5.6%), colored by the tensile stress in x-direction. 63

4.6 Stress-strain curves from bi-crystal tensile tests with misorientation angles at 10°, 20°, and 30°. The $a-e$ locations pointed out in the stress curve for 20° misorientation correspond with the series of images shown in Figure 4.5. 65

4.7 Critical energy release rate as piece-wise linear functions of misorientation angle. (Note that the maximum misorientation angle is 60° due to the lattice symmetry) 66

4.8 The same sample reconstructed in a) MD simulation and d) the proposed model (with mesh). b) and c) show the detailed configurations at the grain boundary joint for different methods. 68

4.9 Comparison of crack growth between a)-d) MD simulation and e)-h) continuum simulation under the uniaxial tension in the x-direction. The stress field is colored. 70

4.10 Comparison of crack growth between a)-d) MD simulation and e)-h) continuum simulation under the uniaxial tension in the y-direction. The stress field is colored. 71

4.11 Comparison of stress-strain curves a) MD simulation and b) continuum simulation. 73

4.12 The mesh of the notched polycrystalline graphene sample. 75

4.13 The stress-strain curve of the uniaxial tensile test at pulling velocities of $0.5m/s$, $10m/s$ and $100m/s$. 76

4.14 Failure process in the double notched polycrystalline graphene (right) under uniaxial tension at pulling velocity, $v = 0.5m/s$, with the corresponding stress field (left). 78

4.15 Failure process in the double notched polycrystalline graphene (right) under uniaxial tension at pulling velocity, $v = 10m/s$, with the corresponding stress field (left). 79

4.16 Failure process in the double notched polycrystalline graphene (right) under uniaxial tension at pulling velocity, $v = 100m/s$, with the corresponding stress field (left). 80

5.1 Schematic of the uniaxial compression test using Split-Hopkinson pressure bar test. 86

5.2 Stress-time history with high speed camera images of the failure process of SiC under uniaxial dynamic compression. Note the images(right) are

captured with an inter-frame interval of 3 μs while the corresponding stress levels are marked by red dots in the stress curve(left). 87

5.3 Effect of strain rate on the compressive strength of ceramic materials (SiC and AlN) measured by SHPB tests. 88

5.4 Benchmark test with low grain boundary strength, $G_c^{gb} = 10\% G_c^{grain}$, and low strain rate, $\dot{\varepsilon} = 0.001 s^{-1}$: a) meshes of the cubic sample colored in misorientation, and b)-f) failure process. 90

5.5 a) Reconstructed specimen with loading direction and b) Velocity profile of boundary nodes on the loading surface. 91

5.6 Fracture evolution under uniaxial compression: a)Crack initiation, b)Crack propagation, c)Interaction between cracks and d)Comminution. 94

5.7 Stress history for strain rate at $100 s^{-1}$. The a, b, c and d locations pointed out in the stress curve correspond with the series of facture images shown in Fig. 5.6. 95

5.8 Convergence plot of final strength. 97

5.9 Comparison of the crack growth in different discretizations with mesh sizes equal to (a) $20\mu m$; (b) $15\mu m$; (c) $10\mu m$; (d) $6\mu m$. The first three columns are the evolution of the crack surfaces in the sample colored by the misorientation angle to demonstrate intergranular and transgranular fractures. The last column is the deformed configuration as the stress reaches the peak value. 98

5.10 Comparison of strength decaying between simulation results and empirical models. 101

5.11 Comparison of fracture surfaces at the failure strength between uniform and biased void distribution. 102

5.12 Comparison of trans/intergranular ratio at the failure strength between uniform and biased void distributions. 103

5.14 Crack growth in the polycrystallne SiC sample under dynamic compression at strain rate $1000s^{-1}$: a)-d) are taken at uniformly-apart moments from when cracks first appear till the maximum stress is reached. 106

5.15 Crack growth in the polycrystallne SiC sample under dynamic compression at strain rate $5000s^{-1}$: a)-d) are taken at uniformly-apart moments from when cracks first appear till the maximum stress is reached. 107

5.16 Crack growth in the polycrystallne SiC sample under dynamic compression at strain rate $10000s^{-1}$: a)-d) are taken at uniformly-apart moments from when cracks first appear till the maximum stress is reached. 108

5.17 The stress histories at strain rates of $1000s^{-1}$, $5000s^{-1}$ and $10000s^{-1}$. 109

5.13 Strain rate dependence of SiC predicted by the model in comparison with the experimental data. 110

5.18 The growing volume fraction of failed grain boundaries and inner-grain material points with the stress build-up under different strain rate. 112

5.19 Competition of trans- to inter- granular fractures at different strain rates. 112

5.20 Column: comparison of two misorentation distributions. 114

5.21 The normalized critical energy release rate as a function of misorientation angles. 115

5.22 Comparison of strength, transgranular fracture and intergranular fracture between two samples with different misorientation distributions. 116

Acknowledgements

0.1 Acknowledgements

First, I would like sincerely thank my advisor, Dr. Bo Li, for his support and guidance involved in this work. His profound knowledge and insightful new ideas and patient supervision have helped me over the years of my graduate study. His conscientious and diligent attitude towards the research has inspired and encouraged me to become a scholar like him and I am looking forward to continuing working with him in the future. I would also like to thank the members of my dissertation committee, Prof. Vikas Prakash, Prof. Ozan Akkus and Prof. John Lewandowski for taking time to read my thesis and for the many help and comments.

My especial thanks go to Prof. Vikas Prakash who welcomed me and provided me research opportunity when I first came to Case and introduced me to Dr. Bo Li a few years later. I wouldn't be able to finish my Ph.D. without your help.

I would like thanks to all the professors who I had collaboration with before, Prof. John Lewandowski, Prof. Kiju Lee, Prof. Ozan Akkus, and Prof. Philip Feng. Thank you for providing all the interesting projects which broaden my horizons in the engineering world.

I am thankful to my colleagues in the CMHPC lab, in particular, Zongyue, Hao Wang, Renjie, Chinmay, and Zhida. Your companies make life in Cleveland more warm and colorful.

My deepest thank you goes to my parents who raised me and supported me through everything. Also, I sincerely thank my wife Boya who never stops comforting me and encouraging me. Finally, my thanks to my child, Alex. You fill my life with joy and purpose.

A Micromechanical Computational Frameworks for Dynamic Failure Mechanisms in Polycrystalline Materials at High Strain Rates

Abstract

by

HAO JIANG

0.2 Abstract

This dissertation is concerned with a micromechanical computational framework for the direct mesoscale simulation of dynamic failure mechanisms in brittle polycrystalline materials at high strain rates based on the Optimal Transportation Meshfree (OTM) method and the microstructure-informed Eigen-fracture approach. A statistically equivalent polycrystal structure is reconstructed to match the probability distribution functions of the grain size, orientation and grain boundary misorientation measured in experiments. The crystal elasticity model with damage is employed to predict the anisotropic dynamic response of the polycrystalline structure. Interactions between the crack front and the microstructure during the dynamic failure process is indicated in the model by considering the equivalent energy release rate as a function

of the local micro-features. The computational model is implemented to study the failure process of two-dimensional polycrystalline material (graphene) under uniaxial tension and three-dimensional polycrystalline material (SiC) under dynamic compression. In these studies, the proposed model is validated by comparing the predicted crack growth in graphene against the results from Molecular dynamic (MD) simulations and directly comparing the predicted compressive strength of 6H-SiC at various strain rates against Split-Hopkinson pressure bar (SHPB) experiments. Influence of the microstructure on the dynamic compressive failure mechanisms of 6H-SiC, including the effects of porosity and void spatial distribution, the strain-rate dependence as well as the Misorientation distribution, is quantified thoroughly by using the proposed computational scheme. The analyses in the aforementioned studies demonstrate that the ultimate macroscopic strength of brittle polycrystalline materials under dynamic loading is determined by the competition and combination of intergranular and transgranular fractures in the microstructure.

1 Introduction

1.1 Overview

Ceramics materials, such as silicon carbide and aluminum nitride, are brittle polycrystalline materials popular in applications of defense and shielding, due to their low density, high-temperature stability, high hardness, and high compressive strength. Such applications usually require a deep understanding of the material's limitation and their dynamic behavior during the failure process. Meanwhile, understanding deformation and failure mechanisms in brittle polycrystalline materials, such as ceramics and modern two-dimensional semiconductors, under dynamic loading are crucial for improvements and developments in the application of advanced structural materials. Applying the fracture mechanics in the mesoscale level, where each type of defects is considered as the minimum unit instead of atoms, it is evident that the elastic modulus, grain morphology and the fracture toughness of the individual microstructural constituents and interfaces are key elements that govern the failure process in polycrystalline materials.

From the experimental observations over decades, several universal phenomenons regarding the dynamic failure of brittle polycrystalline material are listed as follows:

- The subcritical micro-crack propagates and coalesces before macro crack splits;
- Intergranular fracture is preferred under quasi-static loading conditions, while transgranular fracture becomes dominant as the strain rate increases and fragment size turns to be smaller;
- There exists a critical strain rate (e.g., $1000s^{-1}$) beyond which the ultimate compressive strength is strongly sensitive to the strain rate.

It is generally recognized that the microstructures in real materials play essential roles influencing the modes of fracture and failure, and eventually dictating the macroscopic response of materials. Fig. 1.1 shows the SEM images of SiC fracture surface after compression test, in which both intergranular and transgranular fractures are present. Intergranular fracture is the fracture traveling along the interface between adjacent grains, i.e., grain boundaries while the transgranular fracture is the fracture propagating inside of the grain, i.e., inner grain.

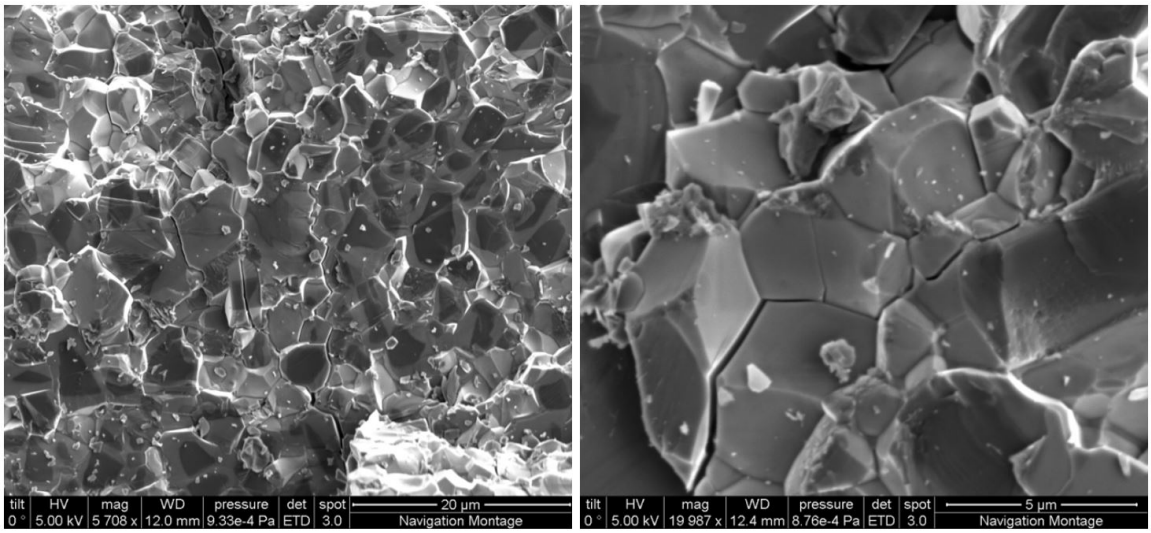

Fig. 1.1. SEM images of SiC fracture surface after compression test.

The preference of one fracture mode to the other indicates that the fracture resistance for each microstructure is unlikely the same, which is definitely true in the microscopic level since the brittle fracture is essentially bond breaking between atoms while each microstructure has its unique atomic structure. Therefore, one can calculate the fracture resistance of a particular microstructure using first principle modelings, such as Density Functional Theory simulation and Molecular Dynamic simulation. To date, it is extremely difficult to characterize the mechanical properties of an individual microstructure. Meanwhile, experimental studies of two-dimensional material, such as grephene and transition metal dichalcogenides(TMDCs), have drawn a lot of attention due to the promising contributions to the fundamental researches. The elastic modulus and the intrinsic strength of the pristine graphene is measured by nanoindentation tests using Atomic Force Microscopy(AFM) [71], while the misorientation angle dependence of the grain boundary strength is also observed in the experiment. The applicability of the classic Griffith theory to the brittle fracture of graphene is also proved through the experimental measurement of the fracture toughness in graphene [132]. In addition, the measurement of bi-crystal graphene provides a quantitative study of the misorientation angle effect on the strength and toughness of the grain boundary [100]. Concepts such as grain boundary design and grain boundary engineering to improve the strength of polycrystalline materials are well-accepted [7,68,120]. The crack propagation through a material microstructure depends on the mechanical state in the vicinity of the crack-tip. Therefore, the local mismatches in fracture toughness of grain interior and grain boundaries significantly influence the crack path. In light of the standpoint above, it is evident that

any numerical fracture model that is able to model crack propagation by incorporating these microstructural features has the potential to describe toughening mechanisms in polycrystals and provide a framework for microstructural design.

Since the late 1980s, spring network method has been widely used in brittle fracture simulations in heterogeneous materials[10,30,31]. Jagota and Bennison[57,58] performed a detailed study on spring-networks and finite element methods for crack propagation simulations revealing a mesh dependency of deformation and crack paths. To avoid these shortcomings, Bolander Jr and Saito[17] proposed a model for random networks based on the Voronoi tessellation which was able to produce homogeneous deformation on uniform straining and showed little bias towards crack propagation directions. Lattice spring models have been used to study brittle fracture and damage in polycrystalline materials. The mechanics of the polycrystalline structure was represented by a spring network on the lattice, where a spring fails if the stored elastic energy in the spring exceeded a critical value. The transition from intergranular (growth along the grain boundary) to transgranular (growth in the grain interior) fracture was observed with increasing grain boundary toughness[126]. Holm[52] study intergranular fracture in polycrystals considering surface formation energies. The influence of low/high-angle grain boundaries and grain boundary micro-cracking on the fracture path was investigated. Kim B-N[63] analyzed two-dimensional crack propagation through a polycrystal as a function of the grain boundary toughness, focusing on the competition between intergranular and transgranular mode of crack propagation.

Another approach to modeling fracture for arbitrary microstructure is the use of cohesive surfaces within a finite element formulation. Zhai and Zhou [130] proposed a micromechanical model in which the cohesive surface formulation of Xu and Needleman [124] is used to study failure modes in composite microstructures. Zavattieri et al. [129] studied intergranular microcrack initiation and evolution in ceramic microstructures under dynamic loading conditions. The traction-displacement relation of the cohesive surface is defined by the particular cohesive rule. Therefore, cracks are only allowed to develop in existing cohesive elements along edges, which can result in an overestimate of the fracture energy when the actual crack paths are not coincident with mesh edges. The results depend not only on the mesh size but also on the mesh shape. This issue can be compensated by remeshing to some degree that is particularly difficult in 3D. It has been noted that the solutions sometimes depend on mesh refinement [41].

Early numerical models for treating discontinuities in finite elements can be traced to the work of Ortiz et al. [93] and Belytschko et al. [11]. They modeled shear bands as 'weak' (strain) discontinuities that could pass through finite elements using a multi-field variational principle. Dvorkin et al. [38] considered 'strong' (displacement) discontinuities by modifying the principle of virtual work statement. A unified framework for analyzing strong discontinuities by taking into account the softening constitutive law and the interface traction-displacement relation was put forth by Simo et al. [112,113]. Applications and extensions of this approach have been proposed by many researchers to date; for a few related studies [5,70,102,114]. In the strong discontinuity approach, the displacement consists of regular and enhanced components, where the enhanced component yields a

jump across the discontinuity surface. An assumed enhanced strain variational formulation is used, and the enriched degrees of freedom are statically condensed on an element level to obtain the tangent stiffness matrix for the element. It is to be noted that, in this approach, the discontinuity surface can only terminate on element boundaries. A comprehensive review and comparison of various embedded discontinuity approaches are provided by Jirásek[60].

To date, the continuum modeling to study discrete crack propagation through a polycrystalline microstructure is still under a developing stage. The computational effort and complexity involved are significant even in two dimensions, and hence the above approach has not received wide attention. The open challenges include:

- Creating a realistic microstructural model based on experimental characterization;
- Adapting the physical fracture criterion in mesoscale;
- Establishing interactions between crack front and microstructures;
- High strain rate modeling compatibility;
- Mesh independence with the crack paths.

To this end, we present a micromechanical computational framework in this work based on the Eigen-fracture scheme and Optimal Transport Meshfree OTM method to model the complexity of microstructure effects on the materials dynamic failure mechanism. The OTM method is employed to overcome challenges in the numerical simulation of large local deformations in solids under extreme loading conditions[74–76]. A direct numerical simulation of the polycrystalline structure is proposed to explicitly account

for the porosity and void distributions, grain sizes, grain orientation, and misorientation distributions. In addition, the critical energy release rate of the material is defined as a function of the local microstructural features (e.g., the misorientation angle) and varies at the grain boundaries and the interior of grains. The interaction between the crack front and topological defects in the microstructure is predicted by comparing the equivalent energy release rate induced by the deformation to the local critical value. Considering the spatial distribution of the fracture property of materials in the polycrystalline structure furnishes an effective means of modeling the intergranular and transgranular fracture patterns simultaneously[116]. In addition, the calculation of the equivalent energy release rate is carried out within a local neighborhood of a material point, which has the effect of eliminating spurious mesh-dependent artifacts. The Eigen-fracture scheme is known to properly converge to Griffith fracture in the limit of vanishingly small mesh sizes. The macroscopic rate-dependency and porosity-strength effect in the brittle polycrystalline materials can be predicted by evaluating the crack propagation in the microstructure interacting with topological defects without introducing any rate-dependency in the models. A mechanistic understanding of the dynamic failure mechanisms in ceramics based on micromechanics can be developed through a detailed description of the competition and combination of intergranular and transgranular fracture patterns in the polycrystalline structures.

1.2 Griffith's theory

In 1913, Inglis[55] provides a linear elastic solution for the stress concentrations around elliptical holes. However, Inglis's formula states the stresses approach infinity at the tip of a perfectly sharp crack. As a result, the predicted strength of materials would be near zero since the bonds there would rupture immediately, even for very small applied loads. In 1920, Griffith[47] employed an energy-balance approach to predict fracture strengths in the glass, while using Inglis's solution, which has become one of the most famous developments in materials science and has been considered to be the birth of the field of fracture mechanics. The general derivation is briefly written as follow.

The strain energy density in the stressed elastic material is

$$W = \frac{1}{V}\int F dx = \int \frac{F}{A}\frac{dx}{L} = \int \sigma d\epsilon, \tag{1.1}$$

where the volume, V can be expressed as the multiplication of area and height, AL, F and dx denote force and displacement while σ and ϵ represent stress and strain. If the material is linear elastic, i.e., $\sigma = E\epsilon$, then the strain energy density is

$$W = \frac{E\epsilon^2}{2} = \frac{\sigma^2}{2E}. \tag{1.2}$$

When a crack has grown into a solid to a depth a, a region of material adjacent to the free surfaces is unloaded, and its strain energy released. Using the Inglis solution, Griffith was able to compute just how much energy this is.

A simple way of visualizing this energy release, illustrated in Fig. 1.2, is to regard two triangular regions near the crack flanks, of width a and height βa, as being completely

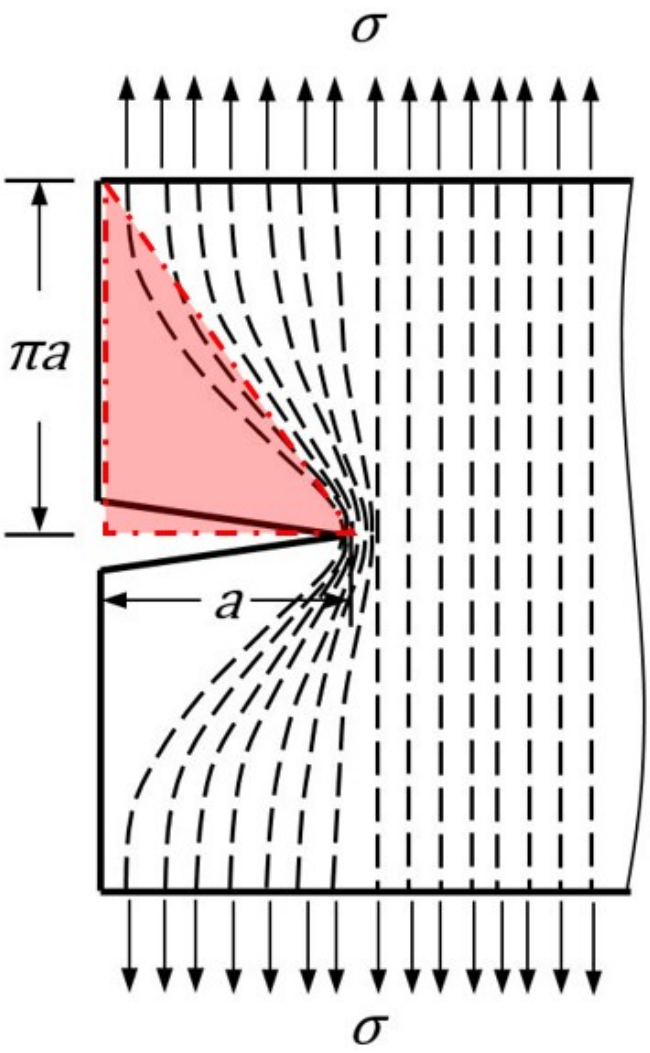

Fig. 1.2. Idealization of unloaded region near crack flanks.

unloaded, while the remaining material continues to feel the full stress σ. The parameter β can be selected so as to agree with the Inglis's solution, and it turns out that for plane stress loading $\beta = \pi$. The total strain energy W released is then the strain energy density times the volume in both triangular regions:

$$W = \frac{\sigma^2}{2E} \cdot \pi a^2. \tag{1.3}$$

Here the dimension normal to the $x-y$ plane is taken to be unity, so W is the strain energy released per unit thickness of the specimen. This strain energy is dissipated by crack growth. But for the crack opening, bonds must be broken, and the essential bond energy is effectively absorbed by the material. The surface energy S associated with a crack of length a is

$$S = 2\gamma a, \tag{1.4}$$

where γ is the surface energy (unit in J/m^2) and factor 2 is needed since two free surfaces have been formed. As shown in Fig. 1.3, the total energy associated with the crack is then the sum of the (positive) energy absorbed to create the new surfaces, plus the (negative) strain energy liberated by allowing the regions near the crack flanks to become unloaded.

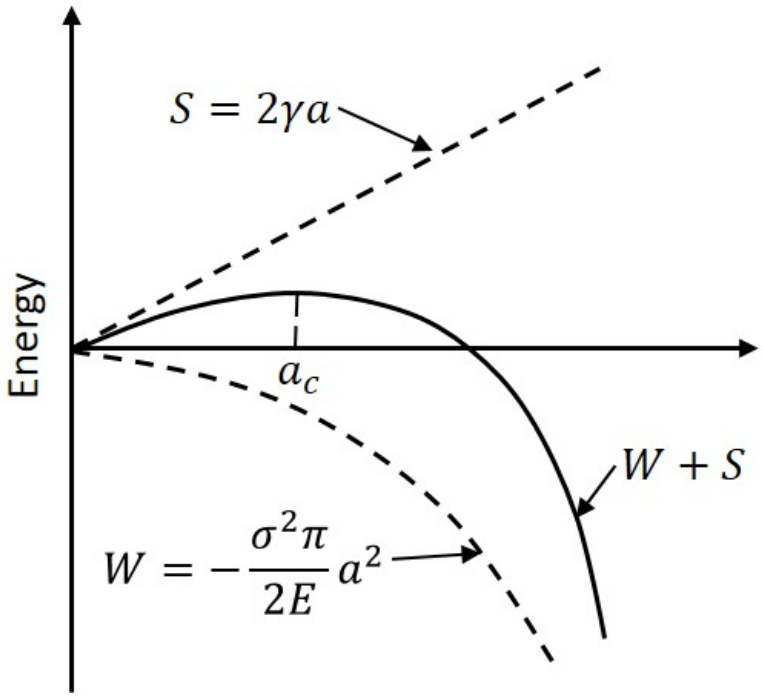

Fig. 1.3. The fracture energy balance.

As the crack grows longer, i.e., a increases, the quadratic dependence of strain energy eventually dominates the surface energy, and beyond a critical crack length ac the system can lower its energy by letting the crack grow still longer. Up to the point where $a = a_c$, the crack will grow only if the stress increased. Beyond that point, crack growth is spontaneous and catastrophic. The value of the critical crack length can be found by setting the derivative of the total energy $W + S$ to zero:

$$\frac{\partial(W+S)}{\partial a} = 2\gamma - \frac{\sigma_f^2}{E}\pi a = 0. \tag{1.5}$$

Since fast fracture is imminent when this condition is satisfied, we write the stress as σ_f.

$$\sigma_f = \sqrt{\frac{2E\gamma}{\pi a}} \tag{1.6}$$

Griffith's original work dealt with very brittle materials, specifically glass rods. When the material exhibits more ductility, consideration of the surface energy alone fails to provide an accurate model for fracture. This deficiency was later remedied, at least in part, independently by Irwin [56] and Orowan [91]. They suggested that in a ductile material a good deal, in fact, the vast majority, of the released strain energy was absorbed not by creating new surfaces, but by energy dissipation due to plastic flow in the material near the crack tip. They suggested that catastrophic fracture occurs when the strain energy is released at a rate sufficient to satisfy the needs of all these energy "sinks" and denoted this critical strain energy release rate by the parameter G_c; the Griffith equation can then be rewritten in the form:

$$\sigma_f = \sqrt{\frac{2EG_c}{\pi a}}. \tag{1.7}$$

This expression describes, in a very succinct way, the interrelation between three important aspects of the fracture process: the material, as evidenced in the critical strain energy release rate G_c; the stress level σ_f ; and the size, a, of the flaw. In a design situation, one might choose a value of a based on the smallest crack that could be easily detected. Then for a given material with its associated value of G_c, the safe level of stress σ_f could be determined. The structure would then be sized so as to keep the working stress comfortably below this critical value.

In 1957, Irwin introduced the critical stress intensity factor, K_c, also known as fracture toughness,

$$K_c = \sigma_f \sqrt{\pi a}. \tag{1.8}$$

Thus, the critical energy release rate can also be written as

$$G_c = \frac{K_c^2}{E}, \tag{1.9}$$

where E is the Young's modulus.

1.3 Layout of the thesis

A brief outline of this dissertation is as follows. Chapter 1 gives the background and overview of the thesis. The aim and objectives are explained with respect to the corresponding research difficulties.

Chapter 2 provides the guidelines and techniques to reconstruct the polycrystalline structures with statistical equivalence to the real materials by integrating a variety of

quantitative information of the materials microstructure, including grain size distribution, grain orientation, and misorientation distributions.

Chapter 3 thoroughly reviews the development of the micromechanical computational framework including the crystal elasticity model, the Optimal Transportation Meshfree (OTM) method and the microstructure informed Eigen-fracture approach.

Chapter 4 reports the reach outcomes of the microstructural effects of 2D polycrystalline graphene during uniaxial tension. The micromechanical computational framework captures the fracture features in the mesoscale, such as the crack locations and the transition between fracture modes by comparison with the MD simulations.

chapter 5 reports a quantitative analysis of the influence of the microstructure on the dynamic compressive failure mechanisms of 6H-SiC, including porosity effect, strain rate dependence and misorientation distribution, by using the micromechanical computational framework. The mesh-independence of the algorithm is validated by refining the mesh of the polycrystalline structure.

Chapter 6 summarizes the work of the thesis and gives some recommendations for future research.

2 Polycrystalline reconstruction

A defect-free material certainly has better mechanical properties than one with defects. However, in reality, defects such as grain boundary and voids are inevitable during the manufacturing process. Fig. 2.1 shows a typical manufacturing process of ceramic materials by sintering method, while grain boundaries and voids are observed in the sintered product by Scanning Electron Microscope(SEM). It is worth mentioning that the voids tend to allocate in the grain boundaries.

In the last decade, with the rapid advancement in the technology on microstructural characterization, such as Electron Backscatter Diffraction(EBSD) Analysis, a variety of quantitative information of the materials microstructure, including grain size distribution, grain orientation, and misorientation distributions, may be integrated into the computational models. This work aims to reconstruct a statistical equivalent polycrystalline structure such that the micro-features included in the simulation have a more practical impact on their contributions to the final strength.

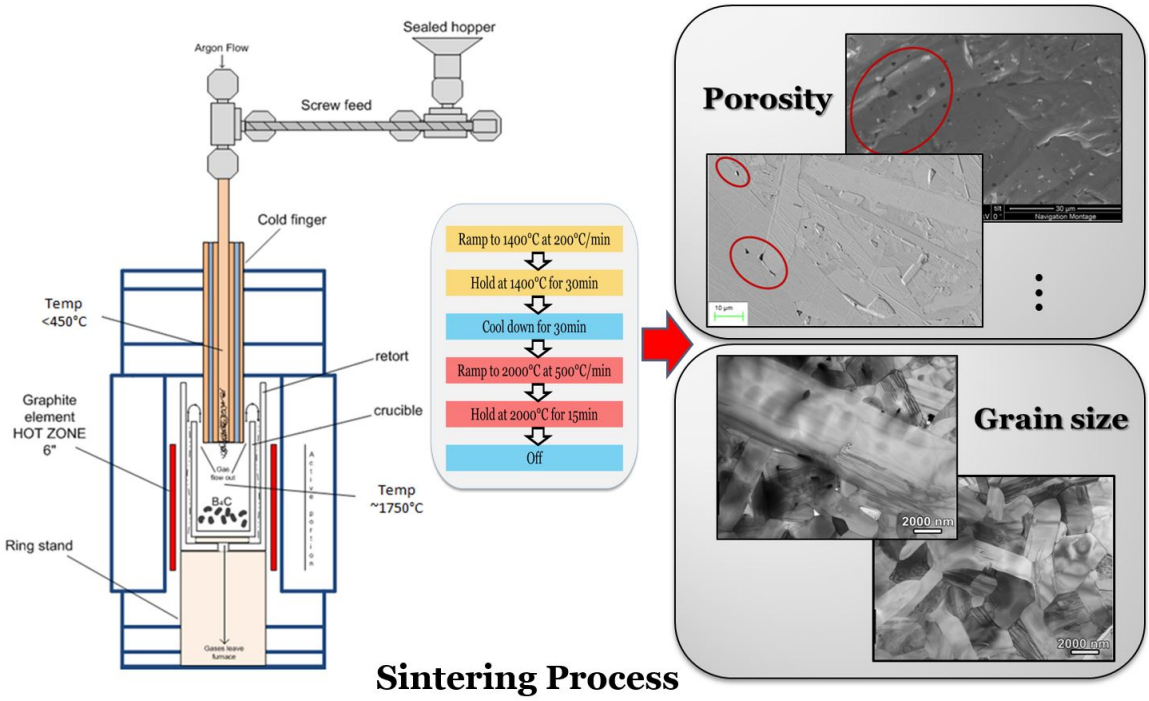

Fig. 2.1. Hot sintering process for manufacturing ceramic materials. SEM images show the common microstructures found in the sintered material.

2.1 Voronoi tessellation

Voronoi tessellation (VT) has been widely used in many applications in areas such as crystallography, computer graphics, epidemiology, geophysics, and meteorology[37,90]. It partitions a given domain into convex polyhedra. Voronoi seeds are a given set of distinct points to partition a domain into corresponding regions. The Voronoi cells are generated by the perpendicular bisectors of the lines linking the seeds. The distance from any point in a Voronoi cell to the corresponding seed is closer than to any other seed.

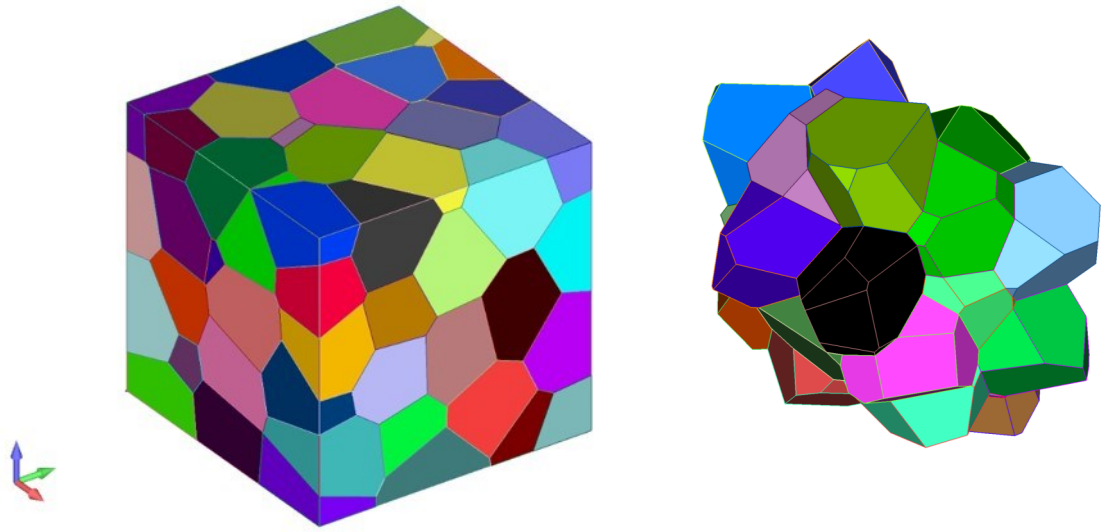

Fig. 2.2. An example of Voronoi tessellation: a) A cubic domain with 100 polyhedron (colored by Voronoi cells) b) Polyhedrons inside the domain.

Fig. 2.2 shows a cubic domain divided by Voronoi tessellation and the Polyhedrons inside the domain. The mathematical presentation of the tessellation can be written as

$$B_i = \{x \in \Omega : \|S_i - x\| < \|S_j - x\| \quad \forall i \neq j, \quad i, j = 1, \cdots, N\}, \tag{2.1}$$

where B_i is a partition of the domain $\Omega \subset \mathbb{R}^d$, $d = 2,3$ corresponding to the seed points S_i, $\|\ \|$ denotes the Euclidean L^2 norm and N is the total number of the seed points. Two adjacent Voronoi cells share a boundary line or surface without intrusion, and the entire domain is occupied by all the Voronoi cells, i.e.,

$$\begin{aligned} &B_i \cap B_j = \emptyset \quad \forall i \neq j; \\ &\bigcup_{i=1}^{N} B_i = \Omega. \end{aligned} \tag{2.2}$$

The Voronoi tessellation resembles a process of solidification or recrystallization where all grains nucleate at each seed simultaneously and grow isotropically at the same

rate. In the past few decades, people have usually employed the VT method to create polycrystalline models for finite element (FE) and meshfree analysis[36,40,44,80,98,104]. For instance Ghosh and Yunshan[45] and Ghosh et al.[46] utilized Voronoi cells to obtain stereologic information for the different morphologies. Liu et al.[79] proposed a method to investigate the damage evolution under uniaxial tension and reversed shear loading conditions, by means of a model combined continuum damage and mechanism-based cavitation, using a Voronoi tessellation to represent the polycrystal microstructure. Bolander Jr and Saito[17] used Voronoi tessellation to discretize homogeneous, isotropic materials prone to fractures such as cement and concrete. Benedetti and Aliabadi[12] modeled intergranular degradation and failure in three-dimensional (3D) polycrystalline microstructures created by the VT method using anisotropic elasticity simulations.

2.1.1 Grain size distribution

The statistical properties of the Voronoi cells, such as the size or shape, can be controlled by the locations of the seeds. If the seeds of the Voronoi tessellation follow the Poisson or random distribution, the generated tessellation is named Poisson-Voronoi tessellation (PVT)[90]. As a result, the number of cell faces, volume, and surface area can be approximated in a log-normal distribution. In addition, there is a special type of Voronoi tessellations, i.e. centroidal Voronoi tessellation (CVT). A Voronoi tessellation is called centroidal when the generating point of each Voronoi cell is also its center of mass. It can be viewed as an optimal partition corresponding to an optimal distribution of seeds. Theoretically, all the centroidal Voronoi cells have an identical size. On the

other hand, studies have shown that CVT based mesh generation is very effective and in a good quality[35]. The definition of a centroidal Voronoi tessellation is the aforementioned definition of Voronoi tessellation with an extra constraint on the location of the seeds. Given the set of Voronoi cells $\{B_i\}_{i=1}^{k}$, the mass center c_i over B_i with mass density $\rho(\vec{x})$ is defined as

$$c_i = \frac{\int_{B_i} \vec{x}\rho(\vec{x})d\vec{x}}{\int_{B_i} \rho(\vec{x})d\vec{x}}. \tag{2.3}$$

Note that the mass density function $\rho(\vec{x}) \geqslant 0$ and $\vec{x}$ is a vector in $\Omega \subset \mathbb{R}^d$. The given seeds $\{S_i\}_{i=1}^{k}$, must satisfy the following condition for a centroidal Voronoi tessellation:

$$S_i = c_i \quad for \quad i = 1, \cdots, k. \tag{2.4}$$

Fig. 2.3 compares the tessellation results by Poisson's Voronoi tessellation and centroidal Voronoi tessellation. In both cases, a $1mm^3$ cube is partitioned into 1000 individual cells. The cell size and shape by PVT in Fig. 2.3(a) is irregular resulting in small edges and sharp corners in the geometry, which will definitely cause difficulties for the mesh creation. Au contraire, the Voronoi cells generated by CVT have similar sizes in a regular shape. The faces of the cells, as seen in Fig. 2.3(b), are usually hexagonal with edges of relevant length. Meanwhile, the size distributions in Fig. 2.3(c) and (d) show a statistical difference between PVT and CVT. The median size for PVT ($0.121mm$) is slightly lower than the one for CVT ($0.124mm$). However, The PVT has a larger standard deviation than CVT, not to mention that the ideal CVT have same cell sizes, as shown in Fig. 2.4.

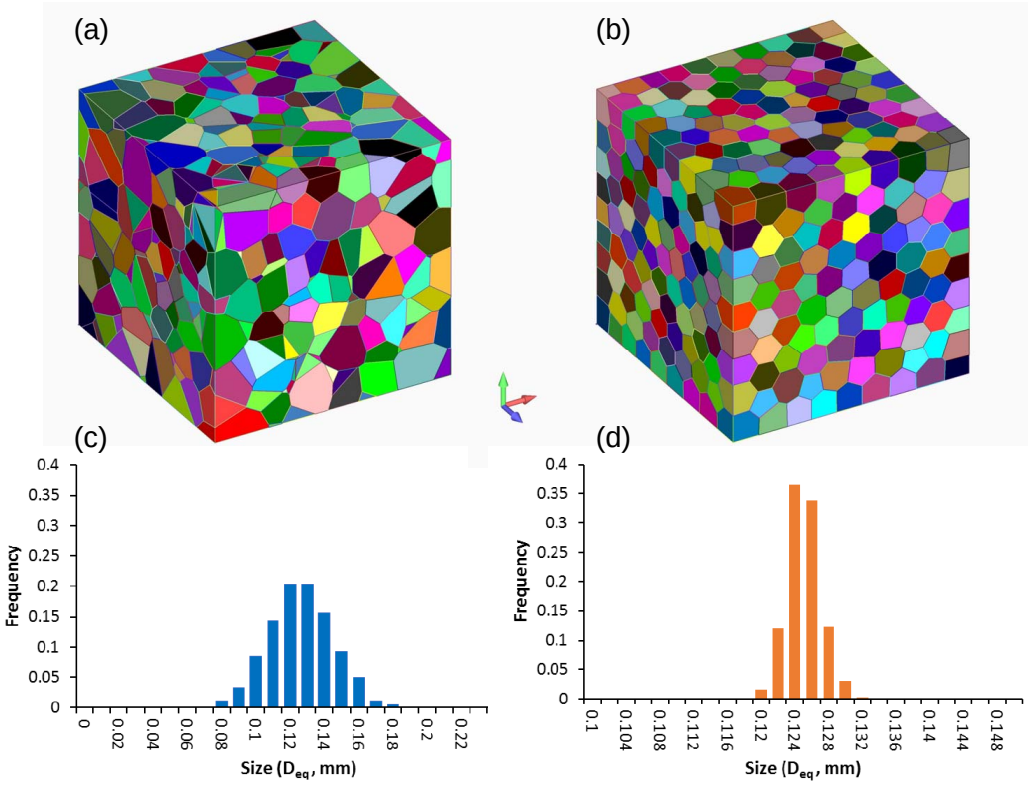

Fig. 2.3. A $1\times1\times1\ mm^3$ cube is divided by a) PVT and b) CVT. The Voronoi cell size distributions of a) and b) are plotted in c) and d), respectively. Note the Voronoi cell size is represented by the equivalent diameter of the cell.

In order to control the cell size distribution, one can control the distribution of seeds in the Voronoi tessellation[131]. For instance, suppose N seeds in a domain of volume V, the mean grain size D_{mean} is given by $D_{mean} \approx V/N$. The seed distance for the most regular tessellation, as seen in Fig. 2.4, must be equal to $d_{reg} = \frac{\sqrt{6}}{2}(\frac{D_{mean}}{\sqrt{2}})^{1/3}$. During the insertion of seeds, a constraint can be introduced:

$$min\|S_i - S_j\| \geq a \cdot d_{reg} \quad \forall i \neq j, \quad 0 < a \leq 1, \tag{2.5}$$

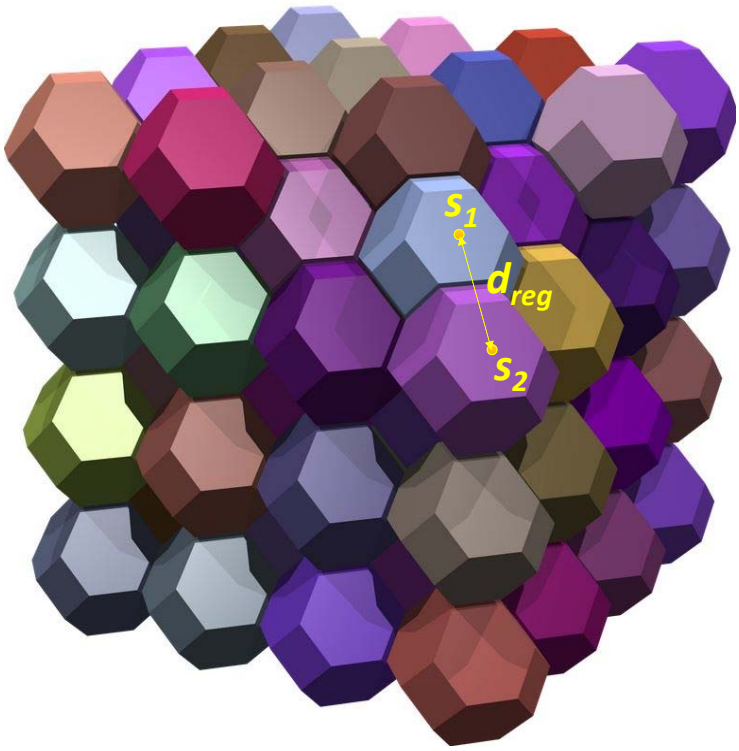

Fig. 2.4. The most regular tessellation in 3D space.

where a is the regularity parameter. Fig. 2.5 shows the probability density function of the grain size distribution versus the values of a.

2.2 Grain boundary and voids

A grain boundary is an interface between two adjacent grains in a polycrystalline material. Grain boundaries can be considered as defects in the crystal structure, and tend to inhibit the electrical and thermal conductivity of the material. Most grain boundaries are preferred sites for the onset of corrosion and for the precipitation of new phases from the solid, which influence the intrinsic strength of the grain boundary. On the

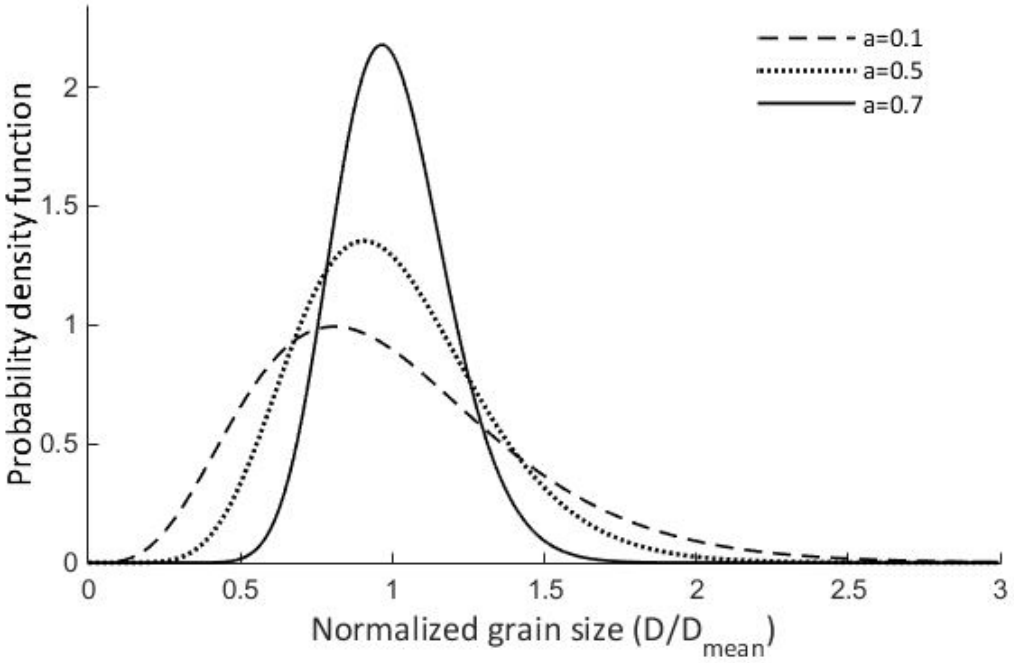

Fig. 2.5. Grain size distributions with different regularity parameters.

other hand, grain boundaries disrupt the motion of dislocations through a material, so reducing crystallite size is a common way to improve mechanical strength, as described by the Hall-Petch relationship. In order to study the grain boundary effects and its failure, it is necessary to represent the grain boundary explicitly in the model. The thickness of the grain boundary is usually few nano-meters. In Molecular Dynamic simulations, grain boundaries are naturally described since the model is at the atomic level. However, in finite element (FE) and meshfree analysis, it is extremely difficult to model the grain boundary at its real length scale. Usually, representative elements are used to approximate grain boundaries. In our computational framework, a triangulation of the Voronoi tessellation can give us the discretized model of a polycrystalline structure. A conforming mesh is generated to assure an explicit discretization of the surfaces of each

grain. In the OTM method, we take the barycenter of each tetrahedron element as the material point and the nodes of the elements as the OTM nodes. The connectivity information of the original mesh becomes the initial neighborhood of the material points. The information on grain orientation and grain boundary misorientation is embedded in the discretization shown in Fig. 2.6(a) and (b). Particularly, the grain boundaries are represented by two thin layers of material points with non-zero misorientation angles as a transition zone as shown in Fig. 2.6(c). All the material points at the inner grain have zero misorientation angles. The nodes on the surfaces of the grains are shared by neighboring grain boundary material points.

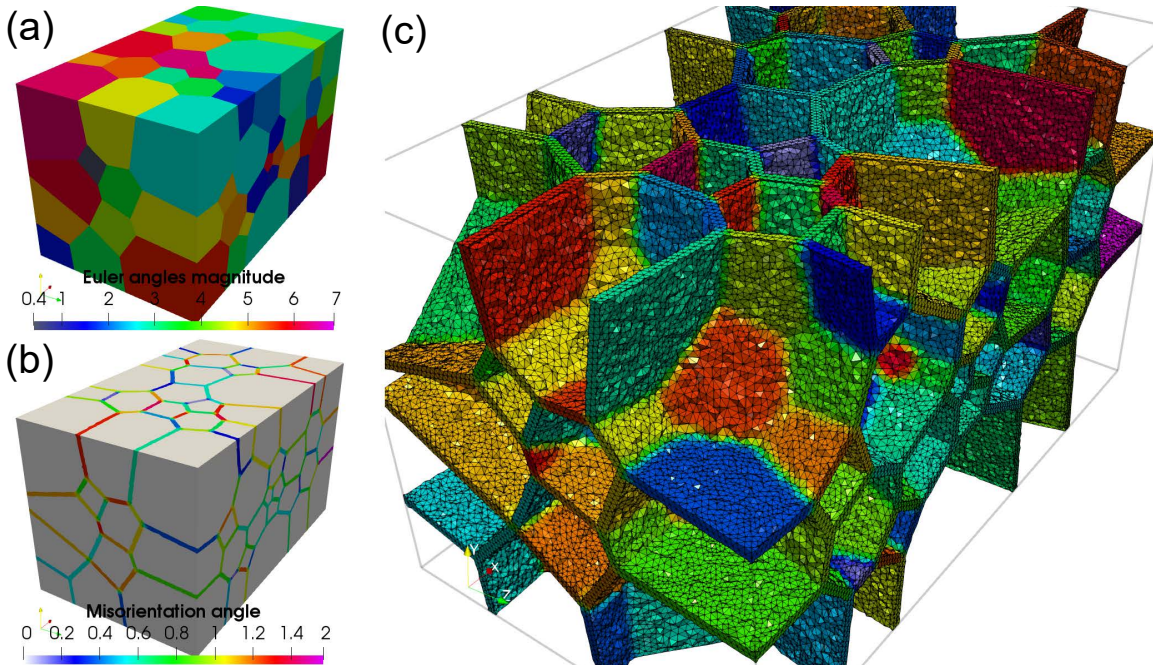

Fig. 2.6. 3D reconstruction of polycrystalline structure: a) grain aggregation (colored by grain orientations) b) polycrystalline structure colored by the magnitude of misorientation angles and c) meshes for the grain boundaries (colored by the magnitude of misorientation angles).

Other micro-defects, such as voids and second phase particles, can also be represented explicitly in this framework when effective material models and properties are assigned to the specific material points in the bulk material as shown in Fig. 2.7. In our direct numerical simulations of the polycrystalline structure, the averaged size of the material points is in $O(1)\mu$m. Thus, the voids can be represented by a single material point or an aggregation of neighboring material points according to their size. The void volume fraction of the material points representing a void is set to be 1, i.e., $\phi = 1$ in Eqn. (3.62).

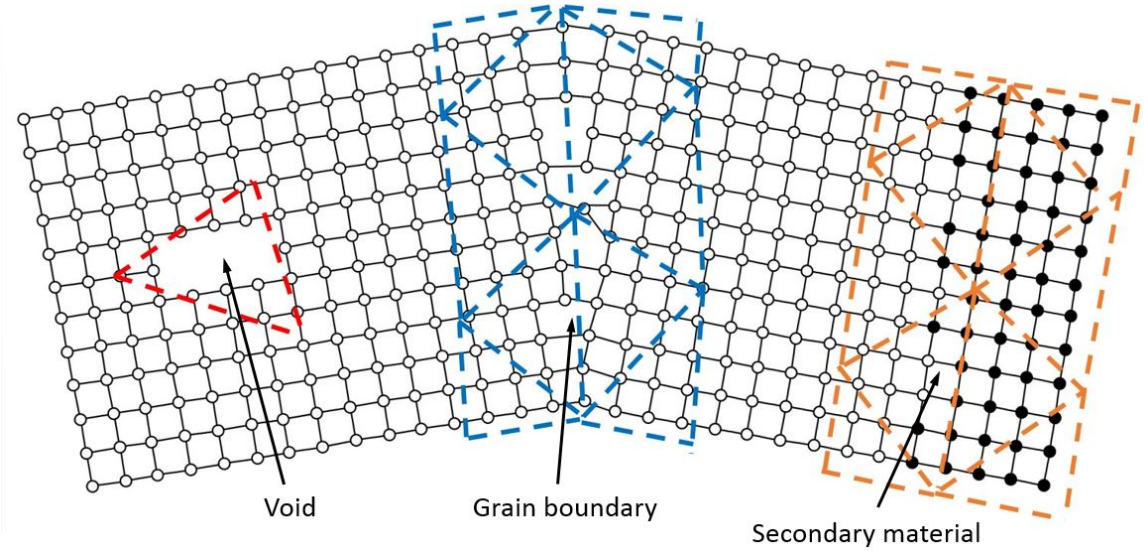

Fig. 2.7. Explicit representations of grain boundaries and other micro-defects(The grid of dots denotes the microstructure of the material while the dashed triangles denote the samples of the discretization in the model).

2.3 Orientation and misorientation

It is generally recognized that the grain orientation and the grain boundary misorientation distributions influence dynamic behavior and failure process of the polycrystalline material in the mesoscale. The grain orientation is defined as the angle between the local crystal coordinates and the global reference coordinate system, which can be denoted by the proper Euler angles (α,β,γ) with respect to rotation axes $z-x'-z''$. In three dimensions, the grain orientations can also be represented by a 3 by 3 orthonormal rotation matrix R. The conversion between Euler angle (α,β,γ) and rotation matrix R can be written as

$$R = \begin{bmatrix} \cos\gamma & \sin\gamma & 0 \\ -\sin\gamma & \cos\gamma & 0 \\ 0 & 0 & 1 \end{bmatrix} \begin{bmatrix} 1 & 0 & 0 \\ 0 & \cos\beta & \sin\beta \\ 0 & -\sin\beta & \cos\beta \end{bmatrix} \begin{bmatrix} \cos\alpha & \sin\alpha & 0 \\ -\sin\alpha & \cos\alpha & 0 \\ 0 & 0 & 1 \end{bmatrix}. \tag{2.6}$$

The misorientation angle of a grain boundary can be calculated using the orientations of two neighboring grains as

$$\theta = min|cos^{-1}\{\frac{tr(\mathbf{R}_B\mathbf{R}_A^{-1})-1}{2}\}|, \tag{2.7}$$

where $\mathbf{R}_A$ and $\mathbf{R}_B$ are the rotation matrices for two neighboring grains A and B as shown in Fig. 2.8.

In order to achieve a high fidelity prediction of the microstructure evolution in simulations, it is critical to generating a statistically equivalent numerical model to the real polycrystalline structure tested in the experiments by matching their orientation and

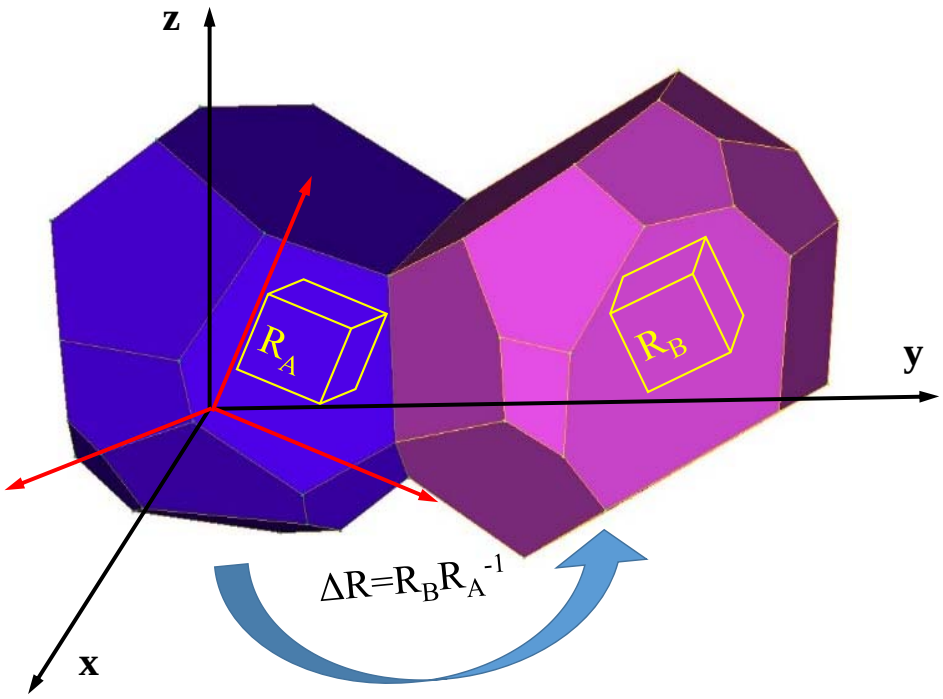

Fig. 2.8. Grain orientation and grain boundary misorientation. The reference coordinates are in black and the crystal coordinates are in red.

misorientation distributions. The orientation of the grains in the Voronoi tessellation is determined directly using the probability distribution function (PDF) of the grain orientations characterized in the Electron Backscatter Diffraction(EBSD) analysis. However, it is not necessary that the misorientation distribution of the initial model will agree with the experimental measurement. Thus, the Monte-Carlo annealing algorithm is utilized in this framework to reorganize the spatial distribution of the grain orientations. The Monte-Carlo annealing algorithm is a probabilistic technique for system optimization, which relies on repeated random sampling towards the convergence. In this particular application, the error of the Monte-Carlo annealing algorithm is defined

as a function of the orientation distribution function(ODF) and misorientation distribution function(MODF) [107]. Suppose Ξ^m and Ξ^e are the polycrystalline structures created by Voronoi tessellation and measured from the experimental sample, respectively, the error is assumed of the form

$$\lambda = \sum_{i=1}^{i_{\max}} (f_i(\Xi^m) - f_i(\Xi^e))^2 + \sum_{j=1}^{j_{\max}} (h_j(\Xi^m) - h_j(\Xi^e))^2, \tag{2.8}$$

where $i_{\max}$ and $j_{\max}$ represent the number of intervals chosen to partition the range of the grain orientation and misorientation angles, respectively. For instance, considering the misorientation angle ranges from 0 to 90 degrees, $j_{\max}$ equals to 9 if the interval is set as 10 degrees. f_i and h_j are the probability of the orientation and misorientation angles in the i-th and j-th interval, respectively. Since the orientations in the model are directly generated by the PDF of the experimental configuration, only the second term in the error function, i.e. the difference between the MODFs, needs to be minimized by the Monte-Carlo annealing process. The computational implementation follows the steps listed in Algorithm 1. Fig. 2.9 demonstrates the performance of this algorithm involving 500 misorientation angles. The grain boundaries of the tested polycrystalline sample are shown in Fig. 2.10. It is evident that the misorientation angle distribution of the model shows an excellent agreement to the target one after applying the Monte-Carlo annealing algorithm. Also, during the process, the orientation angle distribution remains the same and matches the experimental one exactly.

Algorithm 1 Monte Carlo Annealing Algorithm for MODF

Require: $h_j(\Xi_0^m)$: initial model MODF; $h_j(\Xi^e)$: target (or experimental) MODF;

Ensure: minimum error λ

1: Initialization: Set $k = 0$, given the number of intervals $j_{\max}$ and convergence tolerance δ, and calculate the initial error $\lambda_0 = \sum_{j=1}^{j_{\max}} \left(h_j(\Xi_0^m) - h_j(\Xi^e)\right)^2$;

2: Randomly select two grains in the model, A and B, and swap their orientations, i.e. $\mathbf{R}_A^{k+1} = \mathbf{R}_B^k$ and $\mathbf{R}_B^{k+1} = \mathbf{R}_A^k$;

3: Update the model MODF $h_j(\Xi_{k+1}^m)$;

4: Calculate the error $\lambda_{k+1} = \sum_{j=1}^{j_{\max}} \left(h_j(\Xi_{k+1}^m) - h_j(\Xi^e)\right)^2$;

5: Compute the change in the error function $\Delta\lambda = \lambda_{k+1} - \lambda_k$;

6: If $\Delta\lambda < 0$, accept the change. Otherwise, accept the change based on the probability $exp(-\Delta\lambda/M)$ where M is initially set at 10 and reduced by 20% every 100 accepted changes or every 1000 attempted changes, whichever is reached first;

7: Reset $k \longleftarrow k+1$. If $\lambda_{k+1}/\lambda_0 \leqslant \delta$, exit. Otherwise, go to (2).

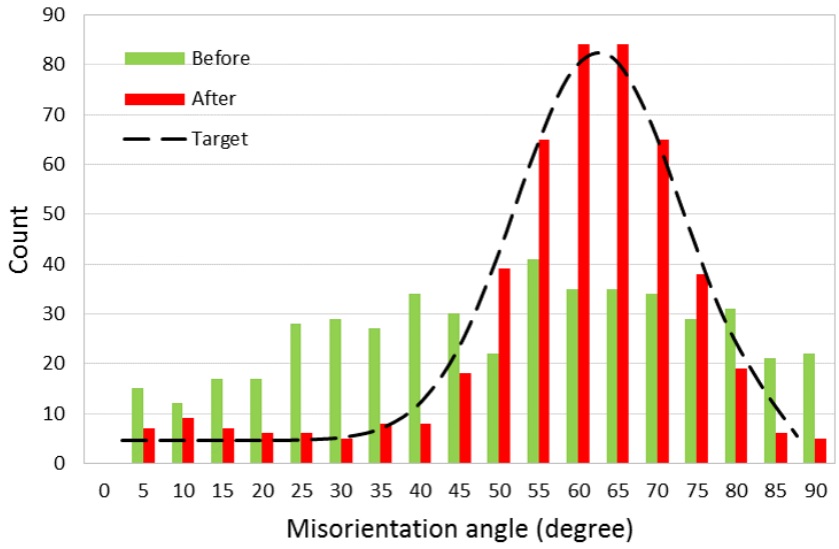

Fig. 2.9. Misorientation distribution before and after applying the Monte-Carlo annealing algorithm in comparison with the target distribution.

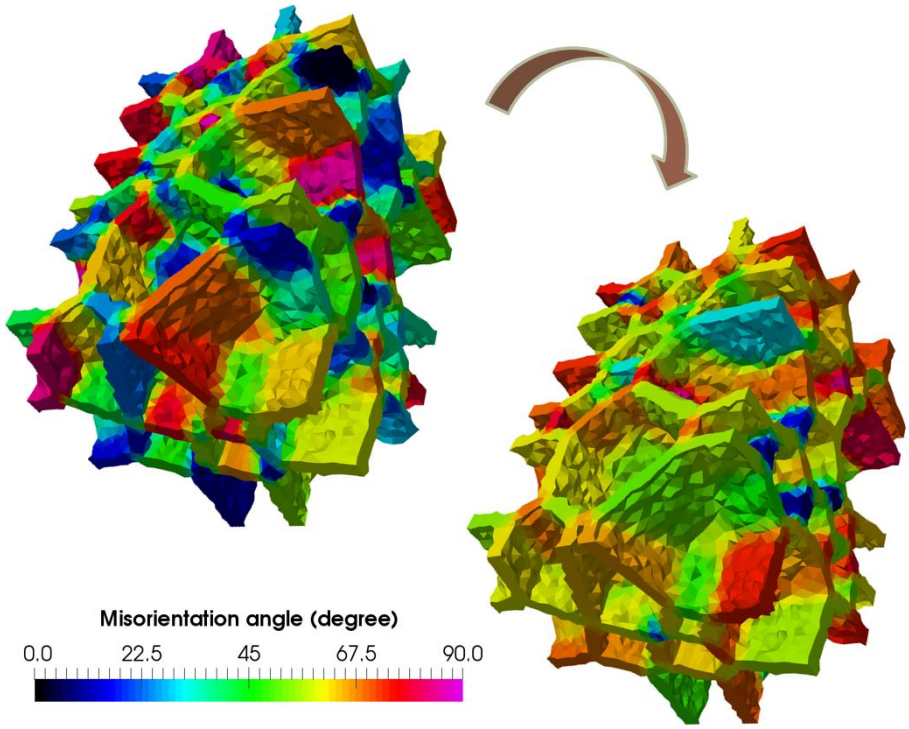

Fig. 2.10. Grain boundaries colored by misorientation angles before and after applying the Monte-Carlo annealing algorithm.

3 Computational framework

A computational framework, based on the Optimal Transportation Meshfree(OTM) method[74] and the EigenErosion scheme[76,108], is presented in this chapter. The goal is to simulate the dynamic crack propagation in brittle polycrystalline structures at high strain rates. In Section 3.1,the conservation of mass and the linear momentum balance are briefly reviewed. In Section 3.2, a crystal elasticity model is used to describe the anisotropic material properties in the polycrystal. Meanwhile, the strain energy density is divided into the volumetric and isochoric parts in order to characterize the failed material. Finally, the solutions for tracking the inter- and transgranular fractures in brittle polycrystalline materials under large deformations are given in Section 3.3 and 3.4.3.

3.1 Continuum mechanics

Considering a body occupying a domain $\Omega_0 \subset \Re^3$ in a certain reference configuration, the positions of material points $P \in \Omega_0$ can be referred by their position vector $\mathbf{X}(P)$ relative to some convenient origin O. The position vectors may further be defined by their components X_1, X_2, X_3 relative to some convenient orthonormal basis $\{\mathbf{E}_1,\ \mathbf{E}_2,\ \mathbf{E}_3\}$ centered at O. We shall refer to this reference frame, $\{\mathbf{E}_i\}$, and O, as the material reference

frame, and to components X_i relative to this frame as material (referential) coordinates. A deformation of a body Ω_0 is an injective mapping $\boldsymbol{\varphi}$: $\Omega_0 \rightarrow \Re^3$. The region $\boldsymbol{\varphi}(\Omega_0)$ is the deformed configuration of the body Ω_0. The deformation mapping $\boldsymbol{\varphi}$ projects material points $P \in \Omega_0$ to material points $p \in \boldsymbol{\varphi}(\Omega_0)$ in one-to-one correspondence. The positions of material points p can be referred by their position vectors $\mathbf{x}(p)$ relative to some convenient origin o. These position vectors may further be defined by their components x_1, x_2, x_3 relative to some convenient orthonormal basis $\{\mathbf{e}_1,\ \mathbf{e}_2,\ \mathbf{e}_3\}$ centered at o. We shall refer to this reference frame, $\{\mathbf{e}_i\}$, and o, as the spatial reference frame, and to components x_i relative to this frame as spatial (current) coordinates. In coordinates, the deformation mapping, see Fig. 3.1, takes the form:

$$\mathbf{x} = \boldsymbol{\varphi}(\mathbf{X}), \quad \mathbf{X} \in \Omega_0 \quad or \quad x_i = \boldsymbol{\varphi}(X_i), \quad i \in \{1, 2, 3\}. \tag{3.1}$$

Note, here and subsequently, Latin indices take the values 1, 2, and 3 while the index in the reference configuration will be substituted by capital letter J in order to distinguish from the spatial configuration. Since, by assumption, $\boldsymbol{\varphi}$ is injective, the inverse deformation mapping $\boldsymbol{\varphi}^{-1}$: $\boldsymbol{\varphi}(\Omega_0) \rightarrow \Omega_0$ is well defined.

Measures of local deformation play a prominent role in the formulation of material models when the principle of local action may be presumed to be in force. Let $dV \in \Omega_0$ be an infinitesimal material neighborhood of point $\mathbf{X} \in \Omega_0$, and let dv be the corresponding infinitesimal spatial neighborhood. Let $\mathbf{X} + d\mathbf{X}$ be a neighboring material

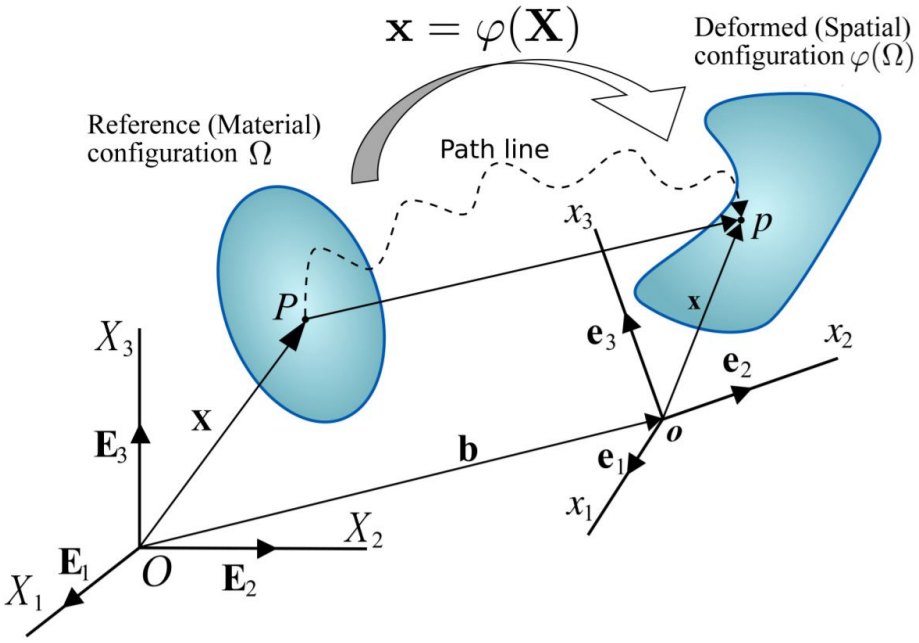

Fig. 3.1. Deformation mapping from the reference configuration Ω to the deformed configuration $\boldsymbol{\varphi}(\Omega)$.

point within dV , and $\mathbf{x}+d\mathbf{x}$ be the corresponding spatial point. Then we have:

$$\mathbf{x}_i + d\mathbf{x}_i = \boldsymbol{\varphi}_i(\mathbf{X}+d\mathbf{X},t) \sim \boldsymbol{\varphi}_i(\mathbf{X},t) + \frac{\partial \boldsymbol{\varphi}_i}{\partial X_J}(\mathbf{X},t)\,dX_J = x_i + \frac{\partial \boldsymbol{\varphi}_i}{\partial X_J}(\mathbf{X},t)\,dX_J. \tag{3.2}$$

Whence we obtain the differential relation

$$dx_i = \frac{\partial \boldsymbol{\varphi}_i}{\partial X_J}(\mathbf{X},t)\,dX_J. \tag{3.3}$$

Thus, the action of the deformation mapping on an infinitesimal material vector $d\mathbf{X}$ at $\mathbf{X}$ is completely determined by the deformation gradient, $\mathbf{F}$

$$F_{iJ}(\mathbf{X},t) = \frac{\partial \boldsymbol{\varphi}_i}{\partial X_J}(\mathbf{X},t) \equiv \boldsymbol{\varphi}_{i,J}(\mathbf{X},t) \equiv \nabla_0 \boldsymbol{\varphi}(\mathbf{X},t), \tag{3.4}$$

where the subscript 0 is the derivative to the reference coordinates $\mathbf{X}$. In general, $\mathbf{F}$ is not symmetric. Clearly, the deformation gradient is a second-order two-point tensor. The

relative change in volume between the deformed and the undeformed state is equal to the Jacobian of the deformation gradient, J

$$J = det(\mathbf{F}) = \frac{dv}{dV}. \tag{3.5}$$

Now, let's consider a body with reference configuration Ω_0 undergoing a motion $\boldsymbol{\varphi}$: $\Omega_0 \times [t_0, t_1] \rightarrow \Re^3$. We shall let $\boldsymbol{\varphi}_t$: $\Omega_0 \rightarrow \Re^3$ be the deformation mapping at time $t \in [t_0, t_1]$. A basic principle of classical mechanics is that mass is a fixed quantity that cannot be formed or vanished. Thus, the mass contained in every sub-body of the closed system must remain constant in time. Let ρ_0: $\Omega_0 \rightarrow \Re$ be the referential mass density per unit undeformed volume or $\rho_0 \equiv dm_0/dV$, and ρ: $\boldsymbol{\varphi}(\Omega_0) \rightarrow \Re$ be the mass density per unit deformed volume at time t or $\rho \equiv dm/dv$. Then, the mass contained in a sub-body $E \in \Omega_0$ is

$$\int_E \rho_0 dV = \int_{\boldsymbol{\varphi}(E)} \rho dv. \tag{3.6}$$

Changing variables on the right from dv to dV by using the (3.5), and rearranging gives

$$\int_E (\rho_0 - \rho_t(\boldsymbol{\varphi}(\mathbf{X})J)dV = 0. \tag{3.7}$$

Since this identity must hold for all measurable subsets of Ω_0, the integrand must vanish identically,i.e.,

$$(\rho \circ \boldsymbol{\varphi}_t)J = \rho_0, \quad \forall E \subset \Omega_0. \tag{3.8}$$

This identity relates the mass densities per unit deformed and undeformed configurations.

The conservation of linear momentum can be provided by the principle of virtual work. It is sometimes referred to as a weak statement of linear momentum balance because it does not involve derivatives of the stress-tensor field.

Let's condenser a body Ω_0 whose boundary is partitioned into two subsets, a displacement or Dirichlet boundary Γ_u, and a traction or Neumann boundary Γ_t, such that $\partial\Omega_0 = \Gamma_u \cup \Gamma_t$ and $\Gamma_u \cap \Gamma_t = \emptyset$.

The motion of the body is subject to the boundary conditions

$$\boldsymbol{\varphi} = \overline{\boldsymbol{\varphi}}, \quad \text{on } \Gamma_u \tag{3.9}$$

$$\mathbf{P}\cdot\mathbf{N} = \overline{\mathbf{T}}, \quad \text{on } \Gamma_t \tag{3.10}$$

where $\overline{\boldsymbol{\varphi}}$ is the prescribed deformation mapping over Γ_u, $\overline{\mathbf{T}}$ are the prescribed material tractions over Γ_u and $\mathbf{P}$ is the first Piola-Kirchhoff stress tensor.

A virtual displacement field $\delta\mathbf{u}$ is introduced over Ω_0, which is said to be an admissible variation if it vanishes identically over the displacement boundary, i.e. if $\delta\mathbf{u}|_{\Gamma_u} = 0$. According to the principle of virtual work, a stress field $\mathbf{P}$: $\Omega_0 \rightarrow \Re^{3\times3}$ is in equilibrium with body forces $\mathbf{B}$ and prescribed tractions $\overline{\mathbf{T}}$ applied over Γ_t, if and only if

$$\int_{\Omega_0} (\mathbf{P} : \nabla\delta\mathbf{u} - \rho_0(\mathbf{B} - \ddot{\boldsymbol{\varphi}})\cdot\delta\mathbf{u})\,dV - \int_{\Gamma_t} \overline{\mathbf{T}}\cdot\delta\mathbf{u}\,dA = 0 \tag{3.11}$$

for all admissible variations $\delta\mathbf{u}$, where $\ddot{\boldsymbol{\varphi}}$ denotes the acceleration of the body.

Integrating by parts and using the fact that $\delta\mathbf{u}$ is admissible to reduce the resulting boundary term to Γ_t gives

$$\int_{\Omega_0} (\rho_0(\ddot{\boldsymbol{\varphi}} - \mathbf{B}) - \nabla_0\cdot\mathbf{P})\cdot\delta\mathbf{u}\,dV + \int_{\Gamma_t} (\mathbf{P}\cdot\mathbf{N} - \overline{\mathbf{T}})\cdot\delta\mathbf{u}\,dA = 0 \tag{3.12}$$

and, since δu is otherwise arbitrary, it follows that the linear momentum balance and boundary conditions must hold, i.e.,

$$\rho_0(\ddot{\boldsymbol{\varphi}} - \mathbf{B}) - \nabla_0 \cdot \mathbf{P} = 0 \tag{3.13}$$

$$\mathbf{P} \cdot \mathbf{N} - \overline{\mathbf{T}} = 0 \tag{3.14}$$

3.2 Constitutive model

Assuming there is no other type of energy dissipation mechanisms except fracture, a crystal elasticity model can be employed at the material points to describe the dynamic anisotropic constitutive relationship of the brittle polycrystalline material[34,42]. Supposing the existence of a Helmholtz free energy density $W(\mathbf{F})$ or strain energy density, it follows from Coleman's relations that the first Piola-Kirchhoff stress tensor is given by

$$\mathbf{P} = \frac{\partial W(\mathbf{F})}{\partial \mathbf{F}}, \tag{3.15}$$

where $\mathbf{F}$ is the deformation gradient. Within an increment framework in the OTM method, the response of the brittle polycrystalline material in each time increment can be approximated as a small strain problem. In specific, the logarithmic strain is adopted which is defined as,

$$\boldsymbol{\varepsilon} = \frac{1}{2} ln(\mathbf{F}^T \mathbf{F}). \tag{3.16}$$

To further describe the behavior of the material points before and after failure, the strain energy density can be decomposed additively into the volumetric and isochoric parts[4],

$$W(\boldsymbol{\varepsilon}) = W^{\text{vol}}(\eta) + W^{\text{dev}}(\boldsymbol{\varepsilon}^{\text{dev}}), \tag{3.17}$$

where

$$\eta = \mathrm{tr}(\boldsymbol{\varepsilon}) \quad \text{and} \quad \boldsymbol{\varepsilon}^{\mathrm{dev}} = \boldsymbol{\varepsilon} - \frac{1}{3}\eta\mathbf{I} \tag{3.18}$$

are the volumetric strain and the deviatoric part of the small strain tensor, respectively.

In particular, the quadratic equation of state is employed, i.e.,

$$W^{\mathrm{vol}}(\eta) = \begin{cases} \frac{1}{2}(1-\chi)K_0\eta^2 & \text{if } \eta \geq 0, \\ \frac{1}{2}(1-\chi)K_0\eta^2 + \frac{1}{2}\chi K_t\eta^2 & \text{if } \eta < 0, \end{cases} \tag{3.19}$$

where χ is a damage parameter used to characterize the failure state of a material point (for simplicity, $\chi = 0$ for the intact material point and 1 for a failed material point), K_0 and K_t are the bulk moduli of the intact and failed material, respectively. The damage parameter will be determined by the Eigenstrain $\boldsymbol{\varepsilon}^*$ introduced in Section 3.4.3. After the material point is failed, it is considered that a crack has penetrated through the entire domain of the material point. Therefore, the failed material point has no resistance to tension but can respond to compressive loads. The isochoric response is modeled by the general Hooke's law, i.e.,

$$W^{\mathrm{dev}}(\boldsymbol{\varepsilon}^{\mathrm{dev}}) = \frac{1}{2}(1-\chi)\boldsymbol{\varepsilon}^{\mathrm{dev}} : \mathsf{C}^{\mathrm{dev}} : \boldsymbol{\varepsilon}^{\mathrm{dev}} + \chi\mu_t \parallel \boldsymbol{\varepsilon}^{\mathrm{dev}} \parallel^2, \tag{3.20}$$

where $\mathsf{C}^{\mathrm{dev}}$ is the isochoric part of the total elastic moduli C of the intact crystalline material while μ_t is the effective shear modulus of the failed material. The behavior of the failed material point for $\chi = 1$ is similar to a granular material in which the shear resistance is caused by the friction between particles. The number of independent material

parameters in the elastic moduli tensor C is subject to the symmetry system of the crystal structure. For a hexagonal structure, such as SiC, the stiffness tensor can be approximated using five independent parameters. In order to compute the isochoric stress and strain energy, several elastic constants need to be modified:

$$C_{11}^{\text{dev}} = (7C_{11} - 2C_{12} - 4C_{13} - C_{33})/9, \quad C_{12}^{\text{dev}} = (-2C_{11} + 7C_{12} - 4C_{13} - C_{33})/9,$$
$$C_{13}^{\text{dev}} = (-2C_{11} - 2C_{12} + 5C_{13} - C_{33})/9, \quad C_{33}^{\text{dev}} = (C_{11} + C_{12} + 2C_{13} - 4C_{33})/9. \tag{3.21}$$

Evaluation of the stresses at each element is performed in the local crystal coordinates instead of the global Cartesian coordinate system, as shown in Fig. 3.2.

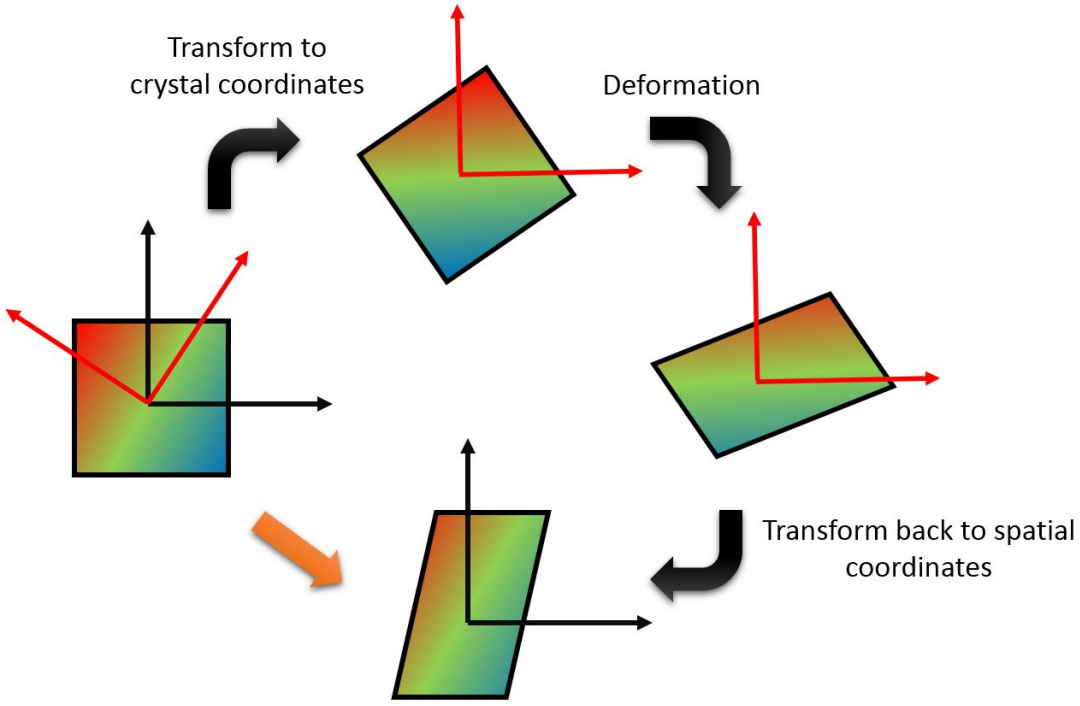

Fig. 3.2. Deformation in the crystal elasticity model using the rotation between crystal coordinates and spatial coordinates.

Therefore, the anisotropic constitutive relation needs to be rotated to accommodate the grain orientations. The coordinate transformations of fourth order stiffness tensor can be written in the following tensor notation,

$$C'_{pqrs} = R_{pi}R_{qj}R_{rk}R_{sl}C_{ijkl}, \tag{3.22}$$

where $\mathbf{R}$ is an orthonormal rotation matrix, with $\mathbf{R}^T\mathbf{R} = I$,

and in the matrix notation as

$$C' = DCD^T \tag{3.23}$$

where the 6 by 6 transformation matrix D related to the rotation matrix,R, as

$$D = \begin{bmatrix} R_{11}^2 & R_{12}^2 & R_{13}^2 & 2R_{12}R_{13} & 2R_{13}R_{11} & 2R_{11}R_{12} \\ R_{21}^2 & R_{22}^2 & R_{23}^2 & 2R_{22}R_{23} & 2R_{23}R_{21} & 2R_{21}R_{22} \\ R_{31}^2 & R_{32}^2 & R_{33}^2 & 2R_{32}R_{33} & 2R_{33}R_{31} & 2R_{31}R_{32} \\ R_{21}R_{31} & R_{22}R_{32} & R_{23}R_{33} & R_{22}R_{33}+R_{23}R_{32} & R_{21}R_{33}+R_{23}R_{31} & R_{22}R_{31}+R_{21}R_{32} \\ R_{31}R_{11} & R_{32}R_{12} & R_{33}R_{13} & R_{13}R_{32}+R_{12}R_{33} & R_{13}R_{31}+R_{11}R_{33} & R_{11}R_{32}+R_{12}R_{31} \\ R_{11}R_{21} & R_{12}R_{22} & R_{13}R_{23} & R_{13}R_{23}+R_{13}R_{22} & R_{13}R_{21}+R_{11}R_{23} & R_{11}R_{22}+R_{12}R_{21} \end{bmatrix} \tag{3.24}$$

3.3 Governing equations and the Optimal Transportation Meshfree (OTM) method

The dynamic behavior of the material can be predicted by solving the mass and linear momentum conservation equations of the system with the specific material models

under given initial and boundary conditions. Consider a body initially occupying a reference configuration Ω_0 in a d-dimensional Euclidean space with boundary Γ. Suppose the boundary can be decomposed into the essential boundary Γ_u and natural boundary Γ_t, such that $\Gamma = \Gamma_u \cup \Gamma_t$ and $\Gamma_u \cap \Gamma_t = \emptyset$. Thus, the motion and deformation of the body is subject to the solution of a general initial boundary value problem in the Lagrangian form, i.e.,

$$\mathbf{F}(\mathbf{X}, t) = \nabla_0 \boldsymbol{\varphi}(\mathbf{X}, t) \quad \text{in } \Omega_0 \times [0, T], \tag{3.25}$$

$$(\rho \circ \boldsymbol{\varphi}(\mathbf{X}, t)) J = \rho_0 \qquad \text{in } \Omega_0, \tag{3.26}$$

$$\rho_0 \ddot{\boldsymbol{\varphi}} - \nabla_0 \cdot \mathbf{P} = \rho_0 \mathbf{B} \quad \text{in } \Omega_0 \times [0, T], \tag{3.27}$$

$$\boldsymbol{\varphi}(\mathbf{X}, t) = \overline{\boldsymbol{\varphi}}(\mathbf{X}, t) \quad \text{on } \Gamma_u \times [0, T], \tag{3.28}$$

$$\mathbf{P} \cdot \mathbf{N} = \overline{\mathbf{T}} \quad \text{on } \Gamma_t \times [0, T], \tag{3.29}$$

$$\dot{\boldsymbol{\varphi}}(\mathbf{X}, 0) = \mathbf{V}_0(\mathbf{X}) \qquad \text{in } \Omega_0, \tag{3.30}$$

where $\boldsymbol{\varphi}$, $\dot{\boldsymbol{\varphi}}$ and $\ddot{\boldsymbol{\varphi}}$ are the deformation, the material velocity and acceleration of the domain, respectively, ρ_0 is the mass density in the reference configuration, $\mathbf{B}$ is the applied body force per unit mass in the reference configuration, and $J = \det(\mathbf{F})$ is the Jacobian of the deformation. In this study, we seek the numerical solution of the governing equations by using the Optimal Transportation Meshfree (OTM) method to address the challenges in grid-based numerical methods for highly localized large deformation at high strain rates. The OTM method is originally introduced by Li and Ortiz[74], which is constructed by combining the optimal transportation theory[118] for time discretization with

Local Maximum Entropy (LME) meshfree approximation[6] and material point sampling. OTM has demonstrated excellent robustness, accuracy and convergence properties in applications involving dynamic deformation and failure of materials[75,76] and, therefore, is ideally suited to the application of interest here. To this end, the corresponding variational structure of the rate problem follows from the formula

$$I[\dot{\boldsymbol{\varphi}}] = \int_{\Omega_0} \left(\dot{K} + \dot{W}(\mathbf{F}) - \rho_0 \mathbf{B}\cdot\dot{\boldsymbol{\varphi}}\right) dV - \int_{\Gamma_t} \overline{\mathbf{T}}\cdot\dot{\boldsymbol{\varphi}}\, dS, \tag{3.31}$$

where K is the kinetic energy, and $\dot{()}$ denotes the material time derivative[94]. A variational update may be defined by introducing the incremental functional from time t_k to t_{k+1},

$$I_k[\boldsymbol{\varphi}_{k+1}] = \inf_{\text{paths}} \int_{t_k}^{t_{k+1}} I[\dot{\boldsymbol{\varphi}}]\, dt. \tag{3.32}$$

Thus, a semi-discretized action can be obtained by a Backward-Euler approximating of the material time derivatives as

$$\begin{aligned} I_k[\boldsymbol{\varphi}_{k+1}] = \frac{1}{2}\frac{\mathrm{d}^2_W(\rho_k,\rho_{k+1})}{t_{k+1}-t_k} + \int_\Omega \left(W_{k+1} - W_k - \rho_k \mathbf{B}_{k+1}\cdot(\boldsymbol{\varphi}_{k+1}-\boldsymbol{\varphi}_k)\right) dV \\ - \int_{\Gamma_t} \overline{\mathbf{T}}_{k+1}\cdot(\boldsymbol{\varphi}_{k+1}-\boldsymbol{\varphi}_k) dS, \end{aligned} \tag{3.33}$$

where

$$\mathrm{d}^2_W(\rho_k,\rho_{k+1}) = \inf_{\text{paths}} \left\{ (t_{k+1}-t_k) \int_{t_k}^{t_{k+1}} \int_{\Omega(t)} \rho(t) |\dot{\boldsymbol{\varphi}}|^2 dV\, dt \right\} \tag{3.34}$$

is the Wasserstein distance between consecutive densities ρ_k and ρ_{k+1}. The first term in Eqn. (3.33) supplies a measure of the inertial action between times t_k and t_{k+1} based on the optimal transportation theory[118]. Thus, the discrete trajectories now follow from the discrete Hamilton's principle $\delta I_k = 0$ of stationary action. Taking variations (Ref[118],

Theorem 8.13) gives

$$\begin{aligned}\delta I_k = &\int_{\Omega_k} \frac{2\rho_k}{t_{k+1}-t_{k-1}}\left(\frac{\boldsymbol{\varphi}_{k\to k+1}(\mathbf{x})-\mathbf{x}}{t_{k+1}-t_k}+\frac{\boldsymbol{\varphi}^{-1}_{k-1\to k}(\mathbf{x})-\mathbf{x}}{t_k-t_{k-1}}\right)\cdot\delta\boldsymbol{\varphi}_{k+1}\,dV\\ &+\int_{\Omega_k}\mathbf{P}_{k+1}:\delta\mathbf{F}_{k+1}\,dV-\int_{\Omega_k}\rho_k\mathbf{B}_{k+1}\cdot\delta\boldsymbol{\varphi}_{k+1}\,dV-\int_{\Gamma_t}\overline{\mathbf{T}}_{k+1}\cdot\delta\boldsymbol{\varphi}_{k+1}\,dS,\end{aligned} \tag{3.35}$$

where the minimizer of the incremental action in $[t_k, t_{k+1}]$ is given in terms of McCann's displacement interpolation[81],

$$\boldsymbol{\varphi}(\mathbf{x},t)=\frac{t_{k+1}-t}{t_{k+1}-t_k}\mathbf{x}+\frac{t-t_k}{t_{k+1}-t_k}\boldsymbol{\varphi}_{k\to k+1}(\mathbf{x}), \tag{3.36}$$

and

$$\dot{\boldsymbol{\varphi}}(\mathbf{x},t)=\frac{\boldsymbol{\varphi}_{k\to k+1}(\mathbf{x})-\mathbf{x}}{t_{k+1}-t_k}. \tag{3.37}$$

In order to obtain a fully discrete action for computations, we begin by approximating the usual Lebesgue measure L of the volume at t_k by discrete measures of the form

$$L^h_k=\sum_{p=1}^{M} v_{p,k}\delta(\mathbf{x}-\mathbf{x}_{p,k}) \tag{3.38}$$

concentrated at material points $\mathbf{x}_{p,k}$, each of which is assigned a discrete volume $v_{p,k}$. The discretization of the mass densities ρ^h_k may be achieved simply by identifying the discrete mass distributions as measures that are absolutely continuous with respect to the discrete volume measure L^h_k, with Radon-Nykodim density ρ^h_k, namely,

$$\rho^h_k(\mathbf{x})=\sum_{p=1}^{M}\rho_{p,k}\delta(\mathbf{x}-\mathbf{x}_{p,k}). \tag{3.39}$$

The quantity $m_p=\rho_{p,k}v_{p,k}$ may be regarded as the mass carried by material point p. Li et al.[74] have shown that the constancy of the material point masses m_p is indeed equivalent to the weak satisfaction of the continuity equation. To complete the spatial

discretization, we approximate the incremental deformation mapping as

$$\boldsymbol{\varphi}^{h}_{k\to k+1}(\mathbf{x}) = \sum_{a=1}^{N} \mathbf{x}_{a,k+1} N_{a,k}(\mathbf{x}), \tag{3.40}$$

where $\{\mathbf{x}_{a,k+1}, a = 1, ..., N\}$ is an array of nodal coordinates at time t_{k+1} and $N_{a,k}(\mathbf{x})$ are conforming shape functions defined over the configuration at time t_k. In calculations, we specifically use the Local Max-Ent (LME) approximation[6]. Since the LME shape functions are strongly localized, the approximation at a material point $x_{p,k}$ depends solely on the nodes contained in a small local neighborhood of the material point. Fig. 3.3 shows an incremental update of the OTM method schematically.

Inserting these approximations into Eqn. (3.35) we obtain the fully-discrete mechanical balance equations with respect to nodal unknowns, which can alternatively be written

$$m_{a,k+1}\ddot{\boldsymbol{\varphi}}_{a,k+1} = \mathbf{f}^{\text{ext}}_{a,k+1} - \mathbf{f}^{\text{int}}_{a,k+1}, \tag{3.41}$$

where $m_{a,k+1}$ denotes the lumped mass of the node $\mathbf{x}_a$ at t_{k+1},

$$\ddot{\boldsymbol{\varphi}}_{a,k+1} = \frac{2}{t_{k+1} - t_{k-1}} \left(\frac{\mathbf{x}_{a,k+1} - \mathbf{x}_{a,k}}{t_{k+1} - t_k} - \frac{\mathbf{x}_{a,k} - \mathbf{x}_{a,k-1}}{t_k - t_{k-1}} \right) \tag{3.42}$$

is a central difference approximation of the nodal acceleration. Thus, combining Eqn. (3.41) and Eqn. (3.42) leads to the update of the nodal coordinates:

$$\mathbf{x}_{a,k+1} = \mathbf{x}_{a,k} + (t_{k+1} - t_k) m^{-1}_{a,k+1} \left(\mathbf{l}_{a,k} + \frac{t_{k+1} - t_{k-1}}{2} (\mathbf{f}^{\text{ext}}_{a,k+1} - \mathbf{f}^{\text{int}}_{a,k+1}) \right), \tag{3.43}$$

where the linear momenta at t_k is defined as

$$\mathbf{l}_{a,k} = m_{a,k+1} \frac{\mathbf{x}_{a,k} - \mathbf{x}_{a,k-1}}{t_k - t_{k-1}}. \tag{3.44}$$

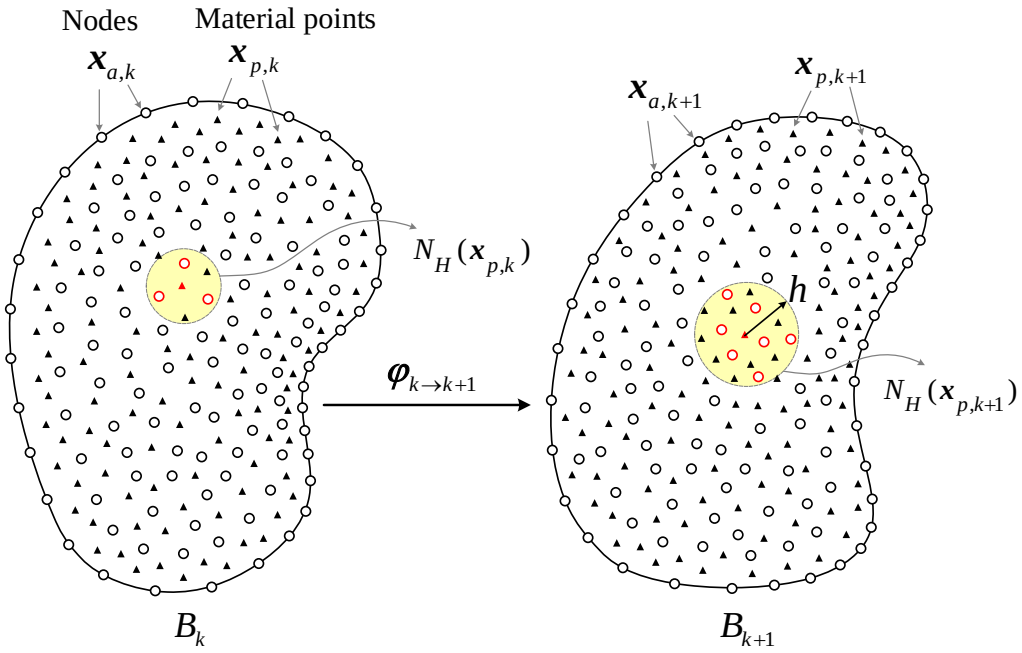

Fig. 3.3. Schematic of the OTM approximation scheme, showing two successive configurations Ω_k and Ω_{k+1} of the domain, mapped by the incremental deformation mapping $\boldsymbol{\varphi}_{k\to k+1}$. The domain is modeled by material points(solid triangles) and nodes(empty circles), where the kinematic information of the body (e.g. displacements, velocities, and accelerations) is carried by the nodes $\mathbf{x}_{a,k+1}$ and the deformation and local state are evaluated at the material points $\mathbf{x}_{p,k+1}$. $N_H(\mathbf{x}_{p,k})$ represents the neighborhood of material point $\mathbf{x}_p$ at time t_k. Only nodes in the neighborhood of the material point $\mathbf{x}_p$ are used to approximate the strain at $\mathbf{x}_p$.

Finally, the internal nodal forces are given by

$$\mathbf{f}^{\text{int}}_{a,k+1} = \int_{\Omega_k} \mathbf{P}_{k+1} \cdot \nabla N_a(\mathbf{x})\, dV = \sum_{p \in S(\mathbf{x}_{a,k})} \mathbf{P}(\mathbf{F}_{p,k+1}) \cdot \nabla N_a(\mathbf{x}_{p,k})\, v_{p,k}, \tag{3.45}$$

where $S(\mathbf{x}_{a,k})$ is the effective support range of node $\mathbf{x}_{a,k}$ at t_k, and the external nodal forces are

$$\begin{aligned}\mathbf{f}^{\text{ext}}_{a,k+1} &= \int_{\Omega_k} \rho_k \mathbf{B}_{k+1} N_a(\mathbf{x})\, dV + \int_{\Gamma_t} \overline{\mathbf{T}}_{k+1} N_a(\mathbf{x})\, dA \\ &= \sum_{p \in S(\mathbf{x}_{a,k})} \rho_k \mathbf{B}(\mathbf{x}_{p,k}) N_a(\mathbf{x}_{p,k})\, v_{p,k} + \sum_{q \in \gamma(\mathbf{x}_{a,k})} \overline{\mathbf{T}}(\theta_{q,k}) N_a(\theta_{q,k}) A_{q,k}.\end{aligned} \tag{3.46}$$

3.4 Fracture models

Standard finite elements have difficulties to capture the crack kinematics since they use continuous shape functions that are not particularly well adapted for solutions with discontinuous displacement fields. In order to overcome this issue in continuum modeling, various fracture algorithms have been developed.

3.4.1 Cohesive interface method for modeling fracture

One of the first models capable of modeling cracks within the FEM is the so-called cohesive interface method. In the approaches by Xu and Needleman[123,124], cohesive surfaces were introduced at the beginning of the simulation. In contrast, Camacho and Ortiz[22] adaptively introduced cohesive surfaces at element edges when a certain cracking criterion is met. This method assumes that the interface carries forces that oppose separation and shear between two surfaces until debonding. The magnitude of these forces is a function of the relative separation and shear displacements between the two surfaces. The tractions at the interface are calculated through the impenetrability condition employed in the contact model. The interface between the two elements is intact until the interface traction reaches the maximum value. Once the maximum traction is

reached, the interface starts failing and the traction reduces to zero linearly up to the maximum displacement jump. The cohesive law[22,92,103], a non-dimensional effective displacement jump is defined by

$$\lambda = \sqrt{(\frac{u_n}{\delta_n})^2 + \beta^2(\frac{u_t}{\delta_t})^2} \tag{3.47}$$

where, u_n and u_t are the actual normal and tangential displacement jumps at the interface estimated by the finite element analysis, and δ_n and δ_t are critical values at which interface failure takes place.

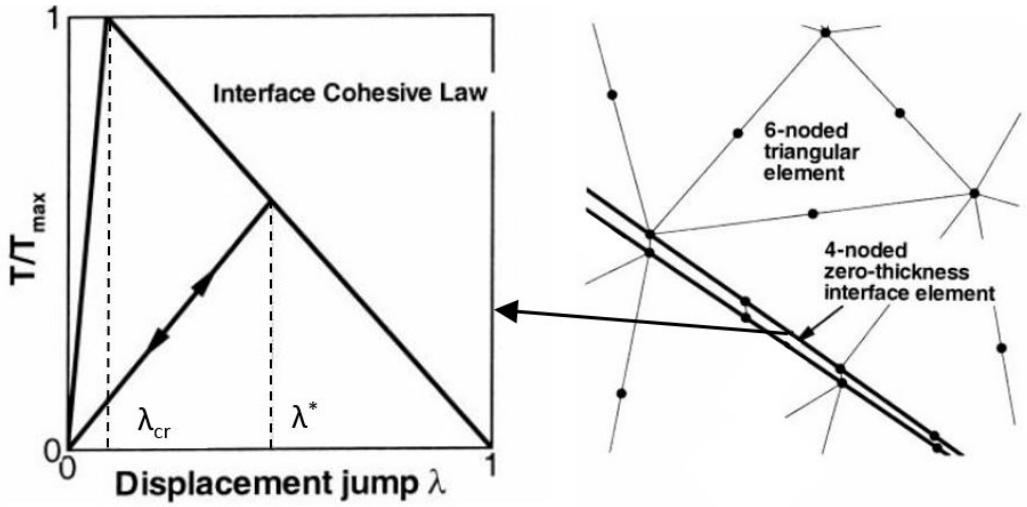

Fig. 3.4. The irreversible interface cohesive law used in the cohesive element at the interface between triangular elements[128].

For a triangular cohesive law, see Fig. 3.4, loading and unloading in the range $0 \leqslant \lambda \leqslant \lambda_{cr}$ are given by

$$T_n = \frac{u_n T_{max}}{\delta_n \lambda_{cr}}, \quad T_t = \alpha \frac{u_n T_{max}}{\delta_n \lambda_{cr}}. \tag{3.48}$$

T_{max} is the maximum normal traction that the interface can develop before failure and $\alpha = \beta(\frac{\delta_n}{\delta_t})$ is the parameter coupling the normal and shear tractions, such that $\beta^2 = G_{IIc}/G_{Ic}$.

It is assumed here that the traction can increase reversible and linearly to its maximum value $T = T_{max}$ when $\lambda = \lambda_{cr}$. Beyond λ_{cr}, the traction reduces to zero up to $\lambda = 1.0$ and any unloading takes place irreversibly[22,92]. For loading in the range $\lambda_{cr} \leq \lambda \leqslant 1$;

$$T_n = T_{max}\frac{u_n(1-\lambda)}{\delta_n\lambda(1-\lambda_{cr})}, \quad T_t = T_{max}\frac{u_t(1-\lambda)}{\delta_t\lambda(1-\lambda_{cr})}. \tag{3.49}$$

Due to irreversibility, loading/unloading in the range $0 \leqslant \lambda \leqslant \lambda^*$, where $\lambda^* \geq \lambda_{cr}$ is the last value of λ from where unloading took place, is given by

$$T_n = \frac{u_n T_{max}}{\delta_n\lambda^*}, \quad T_t = \alpha\frac{u_n T_{max}}{\delta_n\lambda^*}. \tag{3.50}$$

For loading in the range $\lambda^* \leq \lambda \leqslant 1$;

$$T_n = T_{max}\frac{u_n(1-\lambda)}{\delta_n\lambda(1-\lambda^*)}, \quad T_t = T_{max}\frac{u_t(1-\lambda)}{\delta_t\lambda(1-\lambda^*)}. \tag{3.51}$$

Once the effective displacement jump reaches or exceeds a value of 1, the interface element is assumed to have failed and crack is said to have initiated. Subsequent failure of neighboring interface elements leads to crack propagation and coalescence.

In cohesive methods, cracks are only allowed to develop along existing interfaces between elements. This endows the method with comparative simplicity but can result in an overestimate of the fracture energy when the actual crack paths are not coincident with element edges.

3.4.2 Phase Field method for modeling fracture

The phase field method[1,18,33,39,48,50,59,67] allows for the treatment of the global energy minimization as a standard variational problem for which classical FEM is up to the task, though with the restriction that the characteristic length of the mesh should tend to zero faster than the characteristic length of the regularization so as not to overestimate the surface energy of the crack. Due to the inclusion of a second field, a coupled system of equations must now be solved consisting of the original equilibrium/linear momentum equations and the evolution PDE of the phase field. The formulation for the brittle fracture is reviewed as follows.

Let's take the assumption of small deformations, and strain tensor is defined as:

$$\epsilon_{ij} = u_{ij} = \frac{1}{2}(\frac{\partial u_i}{\partial x_j} + \frac{\partial u_j}{\partial x_i}). \tag{3.52}$$

The linear elastic energy density can be written as:

$$\psi_e(\epsilon) = \frac{1}{2}\lambda\epsilon_{ii}\epsilon_{jj} + \mu\epsilon_{ij}\epsilon_{ij}, \tag{3.53}$$

where λ and μ are the Lam$acute$e constant and the shear modulus, respectively. The total potential energy of a body with a crack is:

$$\Psi = \int_\Omega \psi_e dx + \int_\Gamma G_c dx, \tag{3.54}$$

where Ω is the body, Γ is the crack discontinuity surface and G_c is the energy release rate. There is a length scale parameter, l, which determines essentially the damaged area of the crack zone. This comes in as the phase field is approximated by an order parameter

ranging from 0 to 1:

$$c(x) = e^{-|x|/l}. \tag{3.55}$$

When $c = 0$, the material is intact. When $0 \geq c \geqslant 1$, the material is damaged.

When expanding to multi-dimensional solids, the phase field approximation becomes the minimization problem:

$$c(x,t) = Arg\{\inf \Gamma_t(c)\}, \tag{3.56}$$

where $\Gamma_t(c) = \int_\Omega \gamma dV$ and $\gamma = \frac{1}{2l}c^2 + \frac{1}{2}|\nabla c|^2$, ∇c denotes the spatial gradient

The fracture energy can be approximated[20] as:

$$W_c = \int_\Omega G_c(\frac{(c-1)^2}{4l} + l\frac{\partial c}{\partial x}\frac{\partial c}{\partial x})dV \tag{3.57}$$

Once the elastic energy stored in Ω is equal to or greater than the fracture energy, the damage occurs and there is essentially a loss of stiffness in the material. This loss in stiffness represents the model experiencing crack propagation and separation in the material. This stiffness loss is limited to the failure zone and approximates the fracture surface, which physically isn't there because the elements do not actually break or disappear. This loss of stiffness is input in the elastic energy and is given by:

$$\psi_e(\epsilon, c) = [(1-c)^2 + \kappa]\psi_e^+(\epsilon) + \psi_e^-(\epsilon). \tag{3.58}$$

where κ is small positive constant meant to ensure a positive value of the bulk energy as $c \to 1$, ψ_e^+ and ψ_e^- represent the active and passive components of the strain energy, respectively, with only the former contributing to the damage process that results in fractures. The decomposition of the strain energy is to avoid crack opening in compressed regions, which is physically unrealistic. The commonly used decomposition models are spectral decomposition[83] and volumetric-deviatoric split[4].

3.4.3 Microstructure-informed Eigen-fracture approach

Finally, we extend the original Eigenerosion algorithm in our framework for tracking the inter- and transgranular fractures in brittle polycrystalline materials. Consider an elastic body occupying a domain $\Omega \subset R^n, n \geq 2$. The boundary of the body consists of an exterior boundary Γ, corresponding to the boundary of the uncracked body, and a collection of cracks jointly defining a crack set A. To this end, the energy-dissipation functional of a perfectly brittle material is given by:

$$F(u, A, t) = \int_{\Omega \setminus A} W(\boldsymbol{\varepsilon}(u)) dV - \int_{\Gamma_t} \bar{t} \cdot u dS + G_c |A|, \tag{3.59}$$

where $\Omega \setminus A$ denotes the domain of the body with the crack set excluded, G_c is the critical energy release rate, and $|A|$ denotes the area of the crack set. Due to the irreversibility of the fracture, the crack set A must be increasing monotonically over time. Thus, the evolution of crack growth and the corresponding stress field equilibrium can be sought by minimizing $F(u, A, t)$ at all times with respect to both the displacement field u and the crack set A. Nevertheless, a mathematical description of the crack surface is difficult to be derived in engineering applications, especially for three-dimensional problems.

With the help of the Eigen-deformation field $\boldsymbol{\varepsilon}^*$, which describes the crack set occurring in the material as $\boldsymbol{\varepsilon}^* \neq 0$, the crack-tracking problem in perfectly brittle materials can be simplified as the minimization of the action[95].

$$F_\epsilon(u, \boldsymbol{\varepsilon}^*, t) = \int_\Omega W(\boldsymbol{\varepsilon}(u) - \boldsymbol{\varepsilon}^*) dV - \int_{\Gamma_t} \bar{t} \cdot u dS + G_c \frac{\|C_\epsilon\|}{2\epsilon}, \tag{3.60}$$

where ϵ is a parameter that defines an ϵ-neighborhood of the crack set, C_ϵ, and $\|C_\epsilon\|$ is the volume of C_ϵ, as shown in Fig. 3.5. Instead of calculating the exact fracture surfaces, the Eigen-fracture approach characterizes the fracture as a regional failure within the ϵ-neighborhood. Once the material point is failed, the further deformation of the material point is governed by the Eigenstrain, which causes no more changes of the internal energy when the crack surfaces are separating from each other normally. Thus, the damage parameter χ is applied to associating the strain energy contribution under the complex local stress state around the crack.

The stationary of the simplified action in Equation (3.60) with respect to $\boldsymbol{\varepsilon}^*$ leads to the definition of an effective energy release rate at each material point, Ω_e, i.e.,

$$G_p = \frac{\alpha\epsilon}{\|C_\epsilon\|} \sum_{\mathbf{x}_p \in C_\epsilon} v_p W(\boldsymbol{\varepsilon}). \tag{3.61}$$

Thus, the energy release rate attendant to the failure of a material point $\mathbf{x}_p$ is estimated by a local energy averaging procedure in C_ϵ of the intact material points, and $\mathbf{x}_p$ is failed when the effective energy release rate exceeds the critical energy release rate G_c as a minimizer of $F_\epsilon(u, \boldsymbol{\varepsilon}^*, t)$, i.e., $G_p \geq G_c$. The calculation of the effective energy release rate is carried out within a local neighborhood of the element and requires no explicit

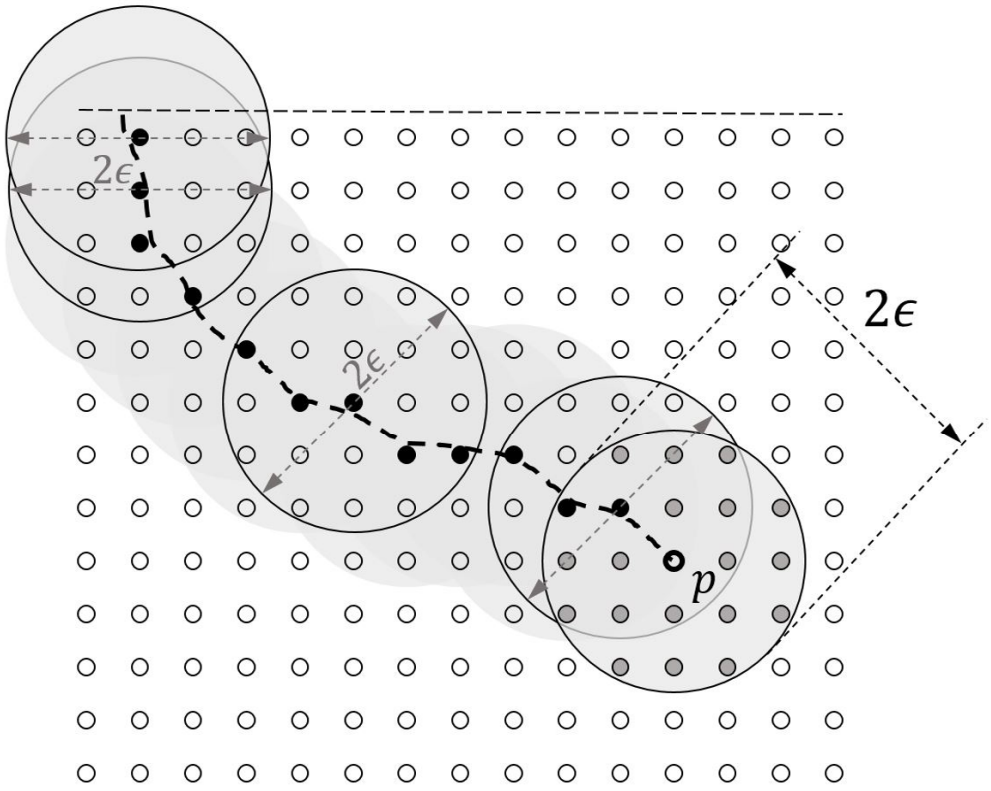

Fig. 3.5. Visualization of the ϵ-neighborhood(shadowed area) of the crack set A. Material points in the crack set are marked as black dots. Intact material points are presented as empty circles and grey dots, while the grey dots are in the ϵ-neighborhood of the material point p for calculating its equivalent energy release rate. The dash line shows the real crack trajectory.

representation of the crack. For linear elasticity, the Eigen-fracture scheme is known to properly converge to the solution of Griffith fracture theory in the limit of vanishingly small mesh sizes[108]. In addition, the local neighborhood averaging of the energy has the effect of eliminating spurious mesh-dependent artifacts. While the minimization problem states the fracture is produced once the averaged local strain energy density exceeds a critical value, it is necessary to investigate further which part of the strain energy density contributes to the crack propagation under complex stress states[78]. For instance,

when an element is under hydrostatic tension, its total strain energy density may be used in the failure criterion to calculate the effective energy release rate. However, when a material point is under hydrostatic compression, only the isochoric strain energy is dissipated due to new fracture surface generation. On the other hand, in the Griffith theory of brittle fracture, the critical energy release rate can be related to the surface energy density of potential fracture surfaces. Moreover, it has been generally recognized that the fracture resistance of brittle materials heavily relies on the distribution of topological defects in the microstructure including grain boundaries, porosity and second phase particles. In this regard, the surface energy density is no longer a fixed value throughout the material but should be considered as a function of the local microstructure features. Consequently, by integrating a microstructure-informed critical energy release rate in the Eigen-fracture approach at each material point, it allows us to explicitly model the interactions between the fracture and topological defects in the microstructure. In this work, only the grain boundaries and voids are explicitly accounted for, where the critical energy release rate at material points is set as a function of the misorientation angle[97] and void volume fraction. In particular, G_c^{gb} is defined in Eqn. (3.62) as a power law function of its misorientation angle for the sake of simplicity. A more precise study will be deployed in the future using Molecular Dynamic(MD) simulations.

$$G_c^{gb}(\theta,\phi) = (1-\phi)G_c^{grain}\exp\left(-c\left(\frac{\theta}{\theta_0}\right)^m\right), \tag{3.62}$$

where ϕ is the void volume fraction at the material point, G_c^{grain} is the critical energy release rate of a single crystal, θ is the misorientation angle, θ_0 is the reference misorientation angle, and c and m are the constants for grain boundary weakening. As the averaged strain energy at a material point exceeds the limit of the local microstructure, a new crack surface will be generated, and the amount of energy dissipated by the crack is evaluated as $G_c^{gb}|A|$.

4 Modeling dynamic failure of polycrystalline graphene under tension

4.1 Introduction

Two-dimensional materials, monolayer or few layers atomically, have extraordinary optical, electronic and mechanical properties theoretically[2,89]. Since the graphene was first isolated in 2004 by micromechanical cleavage[88], there are abundant studies have been performed for characterizing properties and developing applications. Among many attractive attributes of 2D materials, mechanical properties play pivot roles in manufacturing, integration, and performance. The mechanical properties of these 2D crystals are strikingly distinct from those of their 3D counterparts. For instance, nanoindentation experiments show that these 2D nanomaterials can have ultrahigh or very high Young's moduli, e.g., of about $1TPa$ in exfoliated[71] and CVD graphene[72], circa $0.2-0.3TPa$ in MoS_2 [13,23], and extremely high breaking strength ($> 130GPa$ for graphene[71] and $> 20GPa$ for MoS_2 [13]), corresponding to exceptionally high strain limits up to 25%, orders of magnitude higher than in conventional 3D crystals. With strength and flexibility, these 2D nanomaterials are ideal structural materials for future MEMS devices

with various applications such as flexible displays, resonators, sensors, actuators and piezoelectric-generators.

In many practical MEMS applications mentioned above, it is essential to have the large-area (μm^2 to mm^2) and high quality 2D film with reliable performance upon application of strain and strain rate. Theoretically, the pristine, defect-free 2D materials have the highest strength comparing to their polycrystalline allotropes. The fracture strength of the pristine material can be considered as the intrinsic strength corresponding to uniform atomic bond breaking. Mechanical exfoliation can produce single crystal and almost defect-free 2D sheets, but the size is limited ($< \mu m^2$) since the force generated by the exfoliation technique can cause fragmentation of the sample. Among many fabrication methods, chemical vapor deposition (CVD) is the most promising method for the large scale production of large area 2D semiconducting material due to its relative low cost and robustness towards various product types. The roll-to-roll technique has been able to produce predominantly monolayer 30-inch graphene films grown by CVD on copper substrates and multiple transfer[8]. On the other hand, the maximum strength and strain of the large-area polycrystalline 2D material are heavily limited due to the topological defects and their distributions. In the engineering perspective, the fracture strength of the manufactured (e.g. CVD) large area polycrystalline two-dimensional material is rather determined by the fracture toughness due to the existence of the rich mesoscale features (e.g. grain boundaries, grain orientations, vacancies, dislocations and etc.). An experimental measurement of the strength of monolayer graphene was

first reported by Lee et al.[71]. It is measured by nanoindentation of suspended monolayer graphene membranes using an atomic force microscope (AFM), as seen in Fig. 4.1. The measured intrinsic strength of defect-free graphene is $42 N m^{-1}$.

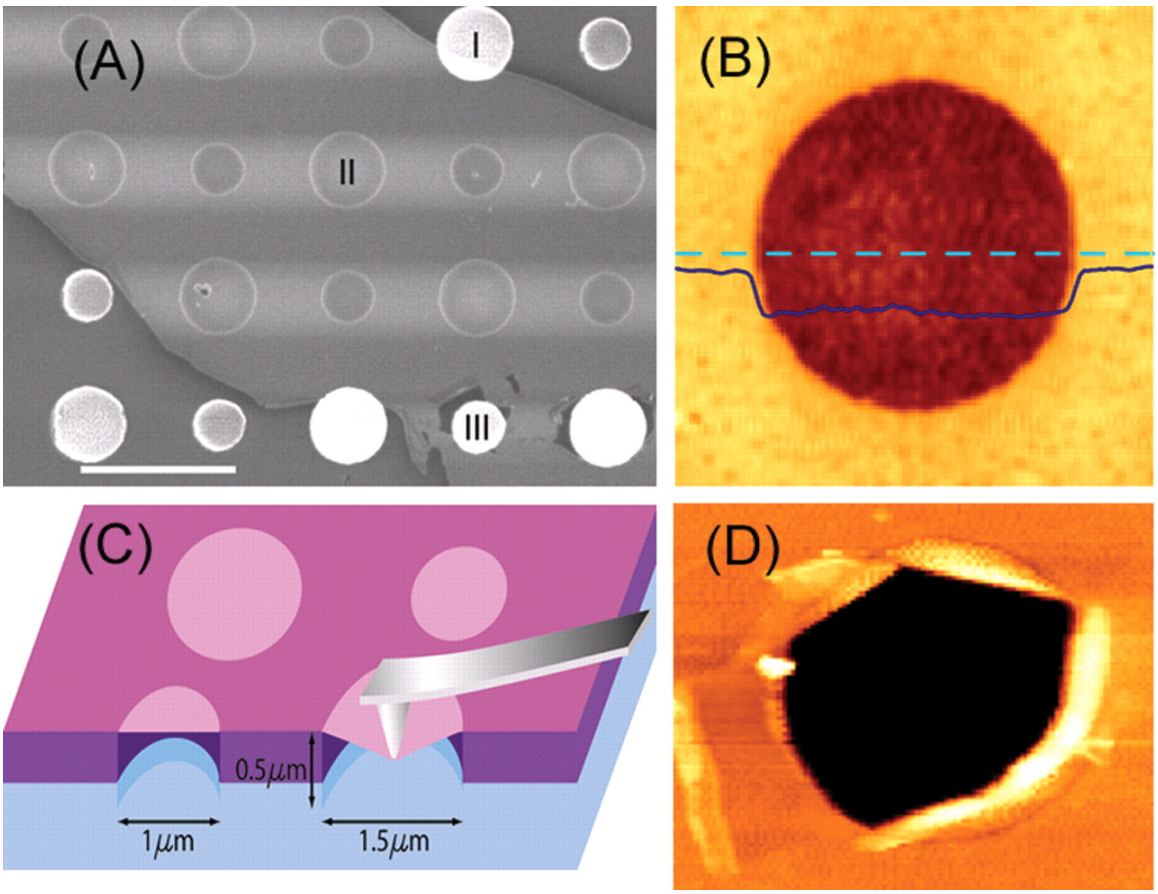

Fig. 4.1. Images of suspended graphene sheets used to measure its mechanical properties with an indenter. (A) SEM of a large graphene flake covering an array of circular holes $1mm$ and $1.5mm$ in diameter. Area I shows a hole partially covered by graphene, area II is fully covered, and area III is fractured from indentation. Scale bar, $3mm$. (B) AFM image of one membrane, $1.5mm$ in diameter. The solid line is a height profile along the dashed line. The step height at the edge of the membrane is about $2.5nm$. (C) Schematic of nanoindentation on the suspended graphene sheet. (D) AFM image of a fractured sheet[71].

In terms of fracture toughness, Zhang et al. [132] designed tension test platform, Fig. 4.2, to measure the fracture toughness of graphene as low as $15.9 N m^{-1}$, which is close to that of ideally brittle materials like silicon and glass. The pre-cracked graphene samples show a fast brittle fracture behavior with the failure stress much lower than the intrinsic strength of graphene.

Meanwhile, the reported toughness values of single-crystal graphene based on atomistic simulations are in general agreement with experimental measurements[62,117,122]. However, the toughness of polycrystalline graphene exhibits large scattering[61,111,133] and seems to depend on the grain size (i.e. grain boundaries) as well as the detailed distribution of topological defects[61,111]. Using AFM indentation method, Rasool et al. [100] tested the strength of bi-crystal graphene. They found the large-angle grain boundaries have strengths that are 89 to 92% of the strength of single-crystal graphene membranes and, for the lowest angle mismatches, the value is 59%. This trend can be explained by considering the critical bond at the strained seven-membered carbon rings that lead to failure; the large-angle boundaries appear stronger because they are able to better accommodate these strained rings, through simple cancellation of tensile and compressive strain in the grain boundary dislocation sequence[121,125].

So far, both experimental and numerical evidence has shown that the final strength of the 2D material is influenced by its the microstructures (e.g. grain boundaries and misorientations) under slow loading conditions (<$1 m/s$). However, many working conditions in 2D material applications have much higher loading rates. For instance, the

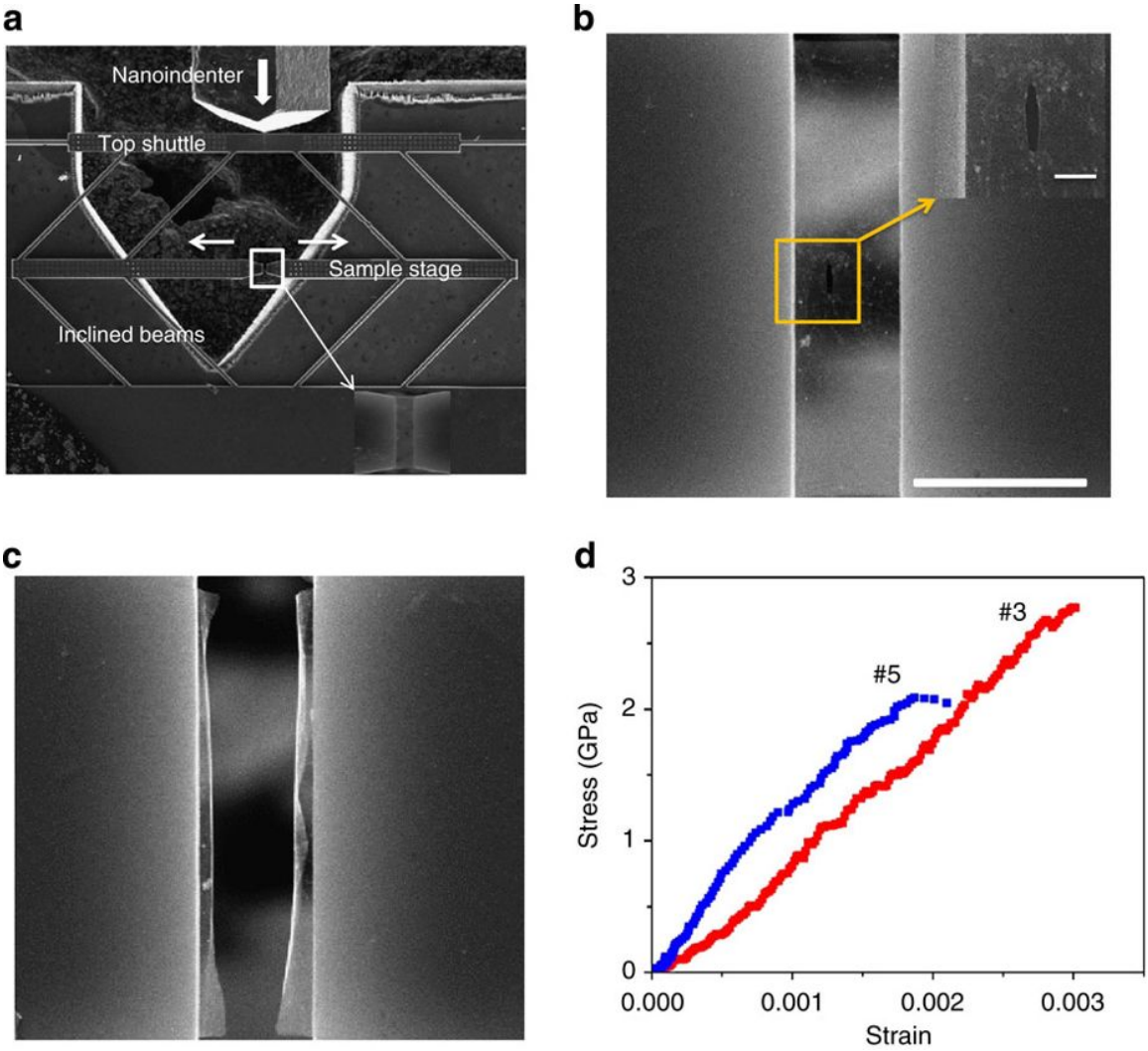

Fig. 4.2. (a) SEM image showing the in situ tensile testing with a microdevice. Movement of the nanoindenter tip (shown by the block arrow) was converted to pure tension of the specimen on the sample stage by the inclined beams. Inset is the magnified image of the boxed region showing graphene across the gap of the sample stage. (b,c) SEM images showing graphene on the sample stage before and after tensile testing, respectively. The pre-crack (boxed in (b)) was cut by FIB. The scale bar in (b) and its inset is $5\mu m$ and $500nm$, respectively. (d) Selected engineering stress-strain curves of the cracked graphene samples (♯3 with crack size $518nm$ and ♯5 with crack size 1256 nm)[132].

piezoelectric generator often operates at sub KHz and the graphene used in the resonator usually vibrates in the sub GHz range (from 1 to 1000MHz). Assuming the strain in each circle reaches 10%, the strain rate of these applications range from $10e^2\ to\ 10e^8 s^{-1}$. To date, Only few researches reached the high strain rate region in the mechanical characterization of 2D materials at large length scale (μm to mm).

Experimental studies of 2D materials at high strain levels (up to the fracture limit) with high strain rates remain an open challenge due to the lack of reliable test platforms and diagnostics. Lee et al.[73] performed miniaturized ballistic tests on multilayer graphene over a range of thickness from 10 to 100 nm. A silica μ-bullet is accelerated, up to $1 km/s$, by expanding gases created by the laser ablation of a gold film, Fig. 4.3.

The penetration energy, E_p, can be estimated by the kinetic and potential energy loss of the projectile[73]. The local strain rate of this experiment can reach as high as $10e^7\ s^{-1}$ corresponding to the maximum impact speed $1 km/s$. Theoretically, the penetration energy is proportional to the fracture stress, $E_p \propto \sigma_c$, if the impact area and penetration thickness are constant[49]. Lee's results also show that the penetration energy increases as the impact velocity increases, see Fig. 4.4. This trend is also found in other macroscopic materials, such as Steel and Aluminum, which is known as the strain-rate dependence.

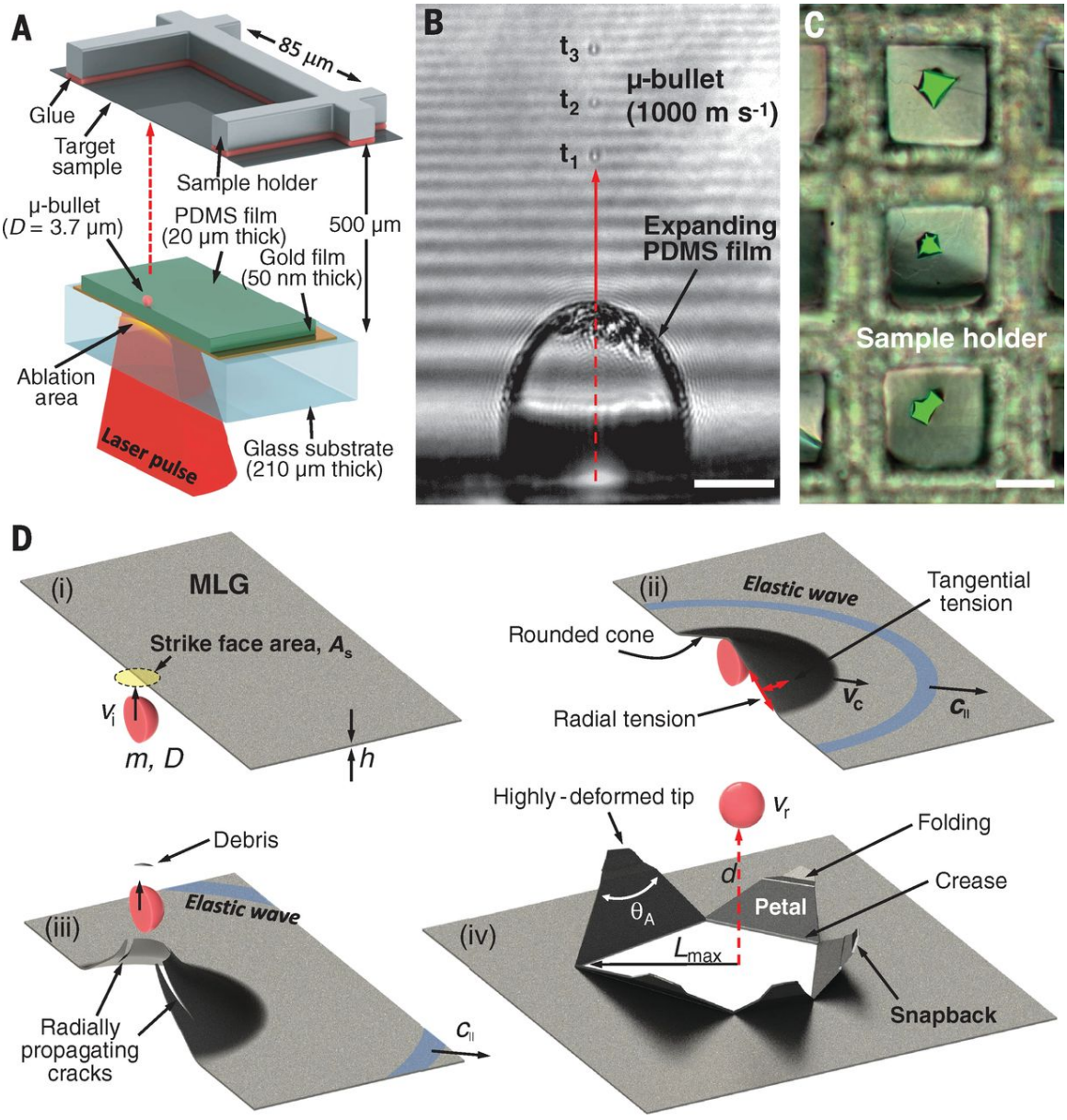

Fig. 4.3. (A) Scheme of the experiment. PDMS, polydimethylsiloxane. (B) Side-view image of a moving μ-bullet taken by triple exposure at time steps t_1 to t_3. (C) MLG membrane on a sample holder after α-LIPIT. Three separate impact test regions are highlighted by green backlight. (D) Schematic illustration of penetration steps: (i) prepenetration stage; (ii) conic deformation stage; (iii) fracture stage; and (iv) postpenetration stage, showing the film morphology after penetration and relaxation. Scale bars in (B) and (C), 50 μm.[73]

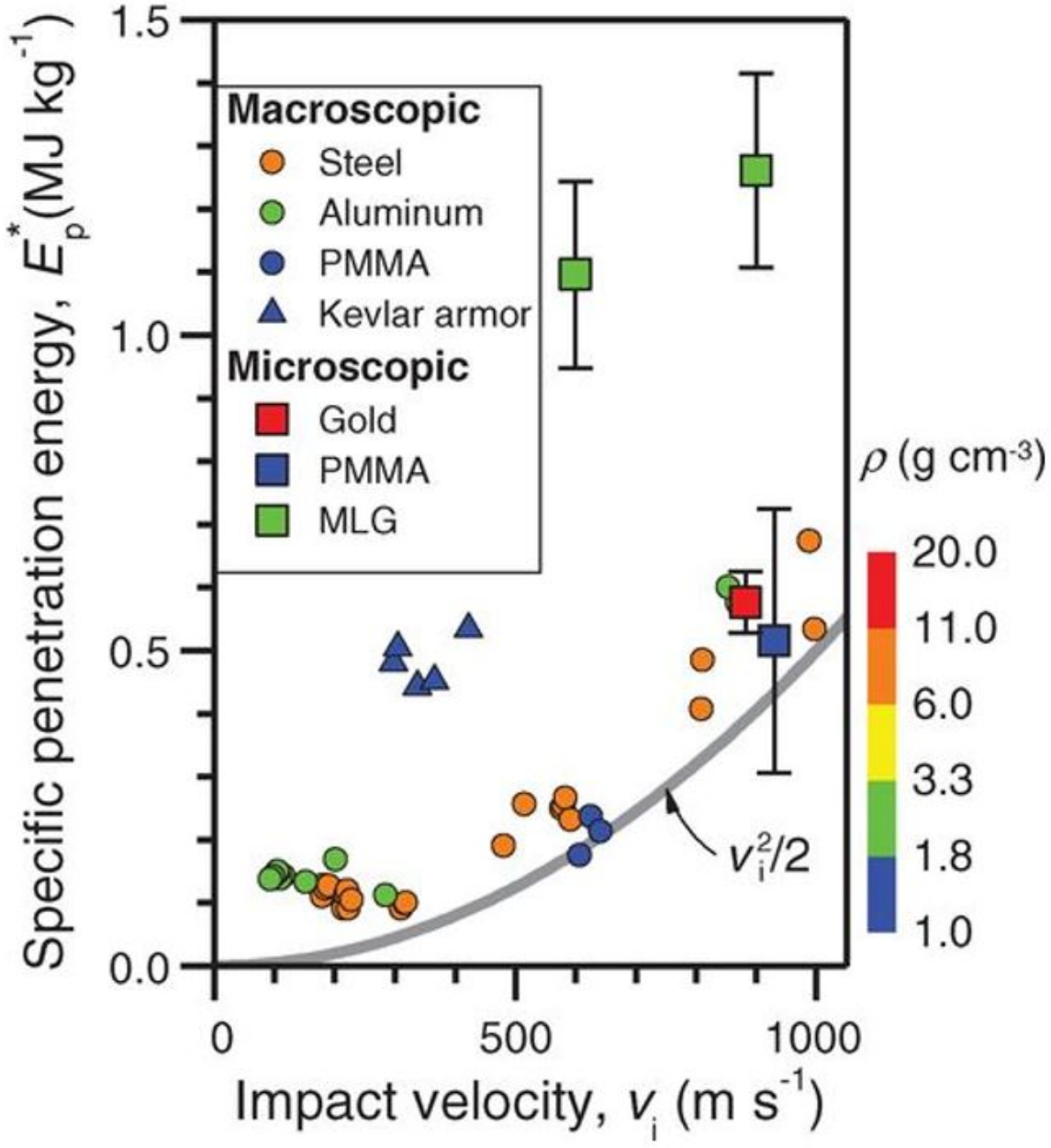

Fig. 4.4. Specific penetration energy of MLG, PMMA, and gold membranes compared with macroscopic materials at various impact velocities. The density of each material is represented by a logarithmic color scale. Error bars denote SD.[73]

Computationally, major difficulties arise from the length and time scales involved, ranging from topological defects on the atomic scale all the way up to the behavior of large single-layer polycrystals at micrometer sizes. The computational capacity of Molecular Dynamic simulation limits the sample size under μm. Zhao [134] investigated the effects of strain rate, and slit on the fracture strength of monolayer single-crystal graphene ($10.08nm \times 10.22nm$) by performing the uniaxial tensile test using MD simulation. Their results show both the fracture strength and the fracture strain increases slightly (< 5.6%) with the increase in the strain rate ($10e^8$ to $10e^{10}s^{-1}$) at room temperature in pristine graphene and the fracture strength decreases significantly (> 50%) with the increase in slit length (from 0 to $1nm$). Yi et al. [127] performed similar studies of the strain rate effect with graphene samples ($10nm \times 10nm$) with one grain boundary sitting in the middle. They find the fracture strength changes with the strain rate is comparable with Zhao's finding in the pristine graphene. Therefore they conclude the strength characteristic of graphene with tilt GBs is insensitive (< 6%) to the strain rate ($10e^8$ to $10e^{10}s^{-1}$). However, by studying a more realistic polycrystalline sample ($30nm \times 30nm$) with a network of GBs, Chen et al. [25] find the fracture strength of the polycrystalline graphene is more sensitive(> 10%) to strain rate ($5e^7$ to $5e^9$) than that of the single crystal graphene(< 4%). They also find the strain rate has a stronger effect on the fracture strength of polycrystalline graphene at a higher temperature than at a lower temperature.

In this work, the proposed computational framework based on the Eigen-fracture scheme and OTM method is implemented to study the dynamic behavior and failure in

large-size 2D materials under various loading rate. In order to investigate microstructure effects on the dynamic failure mechanism, the polycrystalline structures, such as grain orientations and grain boundaries are explicitly modeled by the polycrystalline reconstruction process. It is worth mentioning that the critical energy release rate at the grain boundary, G_c^{gb}, is interpolated from the results of bi-crystal tensile tests with various misorientation angles by atomic simulations. Therefore, the critical energy release rate, G_c, of the material is defined as a piece-wise linear function of the misorientation angle, θ, and varies at different grain boundaries and the interior of grains. Meanwhile, the comparison of the results between the MD simulations and the proposed direct numerical simulations provides a good validation for our computational framework.

4.2 Critical energy release rate function

A series of bi-crystal graphene tensile tests is performed, by Dr. Teng Zhang from Syracuse University, using MD simulations to study the influence of misorientation on grain boundary fracture toughness. The samples used in the MD simulations were in the rectangular shape with $40nm \times 60nm$ in $x-y$ plane, as shown in Fig. 4.5 a.

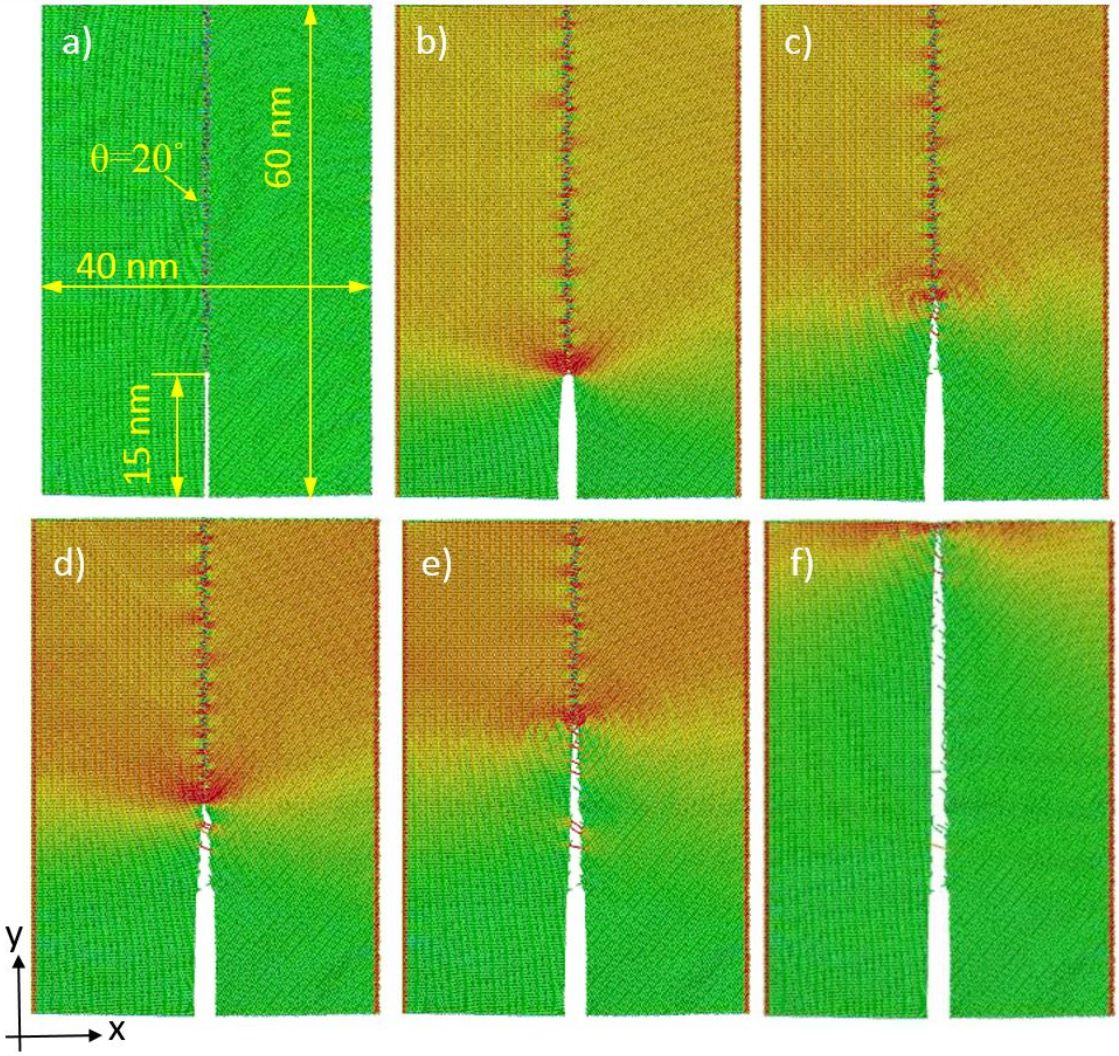

Fig. 4.5. Molecular dynamic simulation of bi-crystal tensile test: a) a sample with a 20° misorientation angle under unloaded condition, b)-f) various stages of the crack growth at the corresponding strain levels(4.5%, 4.65%, 5%, 5.3%, and 5.6%), colored by the tensile stress in x-direction.

A $15nm$ crack along the grain boundary was introduced at the center of the bottom edge by removing carbon atoms. The misorientation, θ is set at 20°. The interatomic interaction between carbon atoms in the graphene sheet was described by the adaptive intermolecular reactive empirical bond order (AIREBO) potential[82]. The carbon-carbon

interaction was prescribed by a switching function with cutoff distances (minimum and maximum cutoff distances of 1.7 and 2Å, respectively). The crack growth is illustrated sequentially through Fig. 4.5b-e), colored by σ_{xx}. As seen in the figures, the stress concentration occurs at the crack tip and the crack follows the grain boundary. Similar crack growth is observed when the misorientation angle is changed. Only stress histories are different. Fig. 4.6 plots the stress-strain relationships for the bi-crystal tensile tests with misorientation angle at 10°, 20°, and 30°. In the three cases, the grain boundary with 20° misorientation angle has the highest strength while the grain boundary with 10° has the lowest strength. In addition, the locations pointed along the stress curve for 20° match the steps of the crack growth demonstrated in Fig. 4.5. The strain level from point a to point f is 0, 4.5%, 4.65%, 5%, 5.3%, and 5.6%, respectively. Before the material fails (from point $a-c$), the stress builds up linearly with the increase of the strain, which indicates the brittleness of the material. The maximum stress (at point c)is reached right after the crack starts to propagate (at point b). Once the material is failed, the stress usually decreases linearly as the strain increases. However, it is interesting to note that the stress raises once more during the stage of stress dropping (at point d). During this short period of time, the crack temporally stops growing and the stress builds up again. The reason for this might be a particular defect in the grain boundary blocking the crack or dislocations occur in a way hardening the material at the crack tip location.

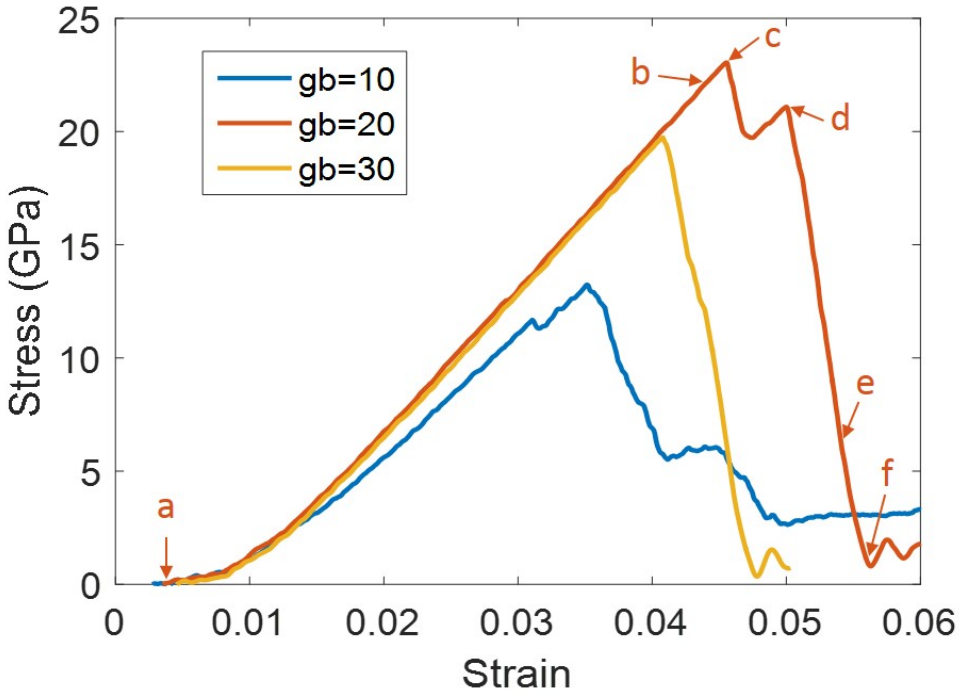

Fig. 4.6. Stress-strain curves from bi-crystal tensile tests with misorientation angles at 10°, 20°, and 30°. The $a-e$ locations pointed out in the stress curve for 20° misorientation correspond with the series of images shown in Figure 4.5.

As aforementioned, the critical energy release rate, G_c, can be calculated using (1.9) with given crack size, a and the maximum stress, σ_f, which are both acquirable in the simulation. Thus, different values of the critical energy release rate at grain boundaries with various misorientation angles are evaluated and mapped in Fig. 4.7. As the data points increase, a more detailed curve can be plotted. So far, piece-wise linear functions are used to interpolate the values between every adjacent mapped data points. Meanwhile, the critical energy release rate based on the fracture toughness of the pristine graphene is also evaluated at $27.5 J/m^2$, using the same sample configuration with

0° misorientation angle. This value is higher than any critical energy release rate of the grain boundary.

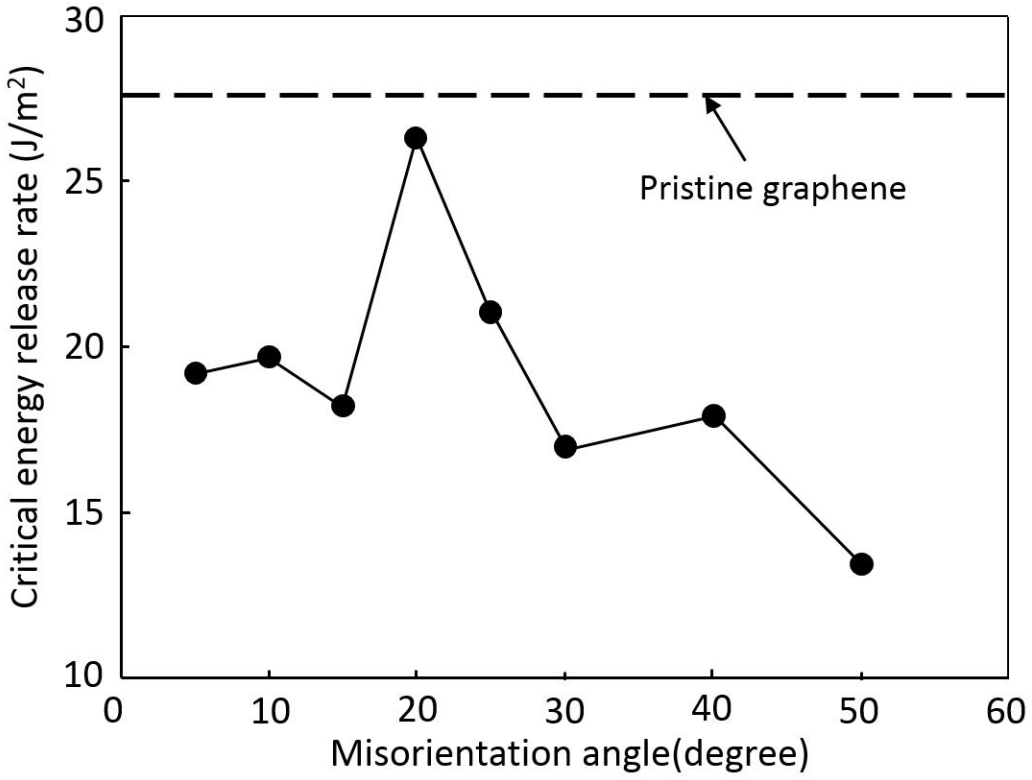

Fig. 4.7. Critical energy release rate as piece-wise linear functions of misorientation angle. (Note that the maximum misorientation angle is 60° due to the lattice symmetry)

4.3 Comparison between MD simulation and continuum modeling

A validation experiment is conducted by comparing MD simulation and our proposed computational framework where the interpolated G_c function is adopted by the Eigenfracture algorithm. The sample tested is a $75nm \times 130nm$ rectangular containing 11 equiaxed hexagonal grains. Fig. 4.8 a) shows the sample used in the MD simulation with

grain orientations mapped in each grain. Three values of orientation angle (0°, 10.9°, and 21.8°) are chosen in an arithmetic sequence, hence the one resulting misorientation angel is two times greater than the other (10.9°, and 21.8°). The sample used in our proposed model is shown in Fig. 4.8 d) with grain boundaries colored by misorientation angles. The geometry is discretized into 15,000 triangular elements with a minimum mesh size $0.83nm$. Since the grain boundary consists of two layers of the finest mesh, its thickness can be approximated at $1.66nm$. The mesh is symmetric about $x-$ and $y-$axis. Fig. 4.8 b) and c) highlighted the representations of grain boundary junction in lattice configuration and continuum mesh configuration, respectively. As seen in Fig. 4.8 b), the grain boundaries are mainly composed of arrays of 5-7 defects which have a higher density in high angle grain boundary than low angle one. Unlike the $G_c^{gb}(\theta)$ function analyzed above, the G_c function at the junctions are way more complicated to evaluate due to multiple variables need to take into account, e.g. misorientations of each connecting grain boundary and angles between each adjacent grain boundaries. Though, it is well-recognized that, in the real material, dislocations tend to form clusters at the grain boundary junction during the grain growth. In our proposed model, the misorientation angle at the grain boundary junction changes gradually from one grain boundary to another, as seen in Fig. 4.8 c). Thus, the evaluated $G_c^{gb}(\theta)$ can be also applied to the junctions.

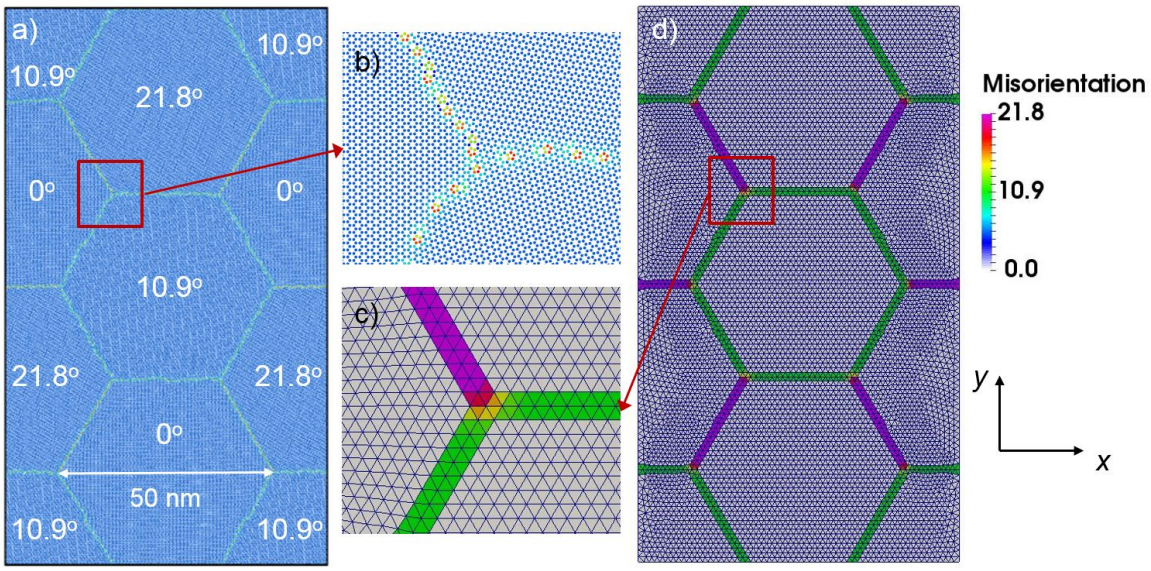

Fig. 4.8. The same sample reconstructed in a) MD simulation and d) the proposed model (with mesh). b) and c) show the detailed configurations at the grain boundary joint for different methods.

Table 4.1 shows the material properties used in the continuum simulation. Since the out-of-plane displacement is disabled in the MD simulation, a plane strain assumption is made in the continuum model for a better comparison.

Table 4.1. Material properties used in the graphene tensile test

Parameter	**Value**	**Definition**
C_{11}	1000	
C_{22}	1000	Elastic constants [GPa]
C_{12}	125	
ρ	5	Density [g/cm^3]
G_c	27.5	Critical energy release rate for single crystal [N/m]

The uniaxial tensile tests are performed in the x-direction and the y-direction, respectively. Same boundary conditions are assigned in both MD and continuum simulations. For instance, in the case of uniaxial tensile in the x-direction, the left and right edges have a uniform velocity of $30m/s$ pulling in opposite directions along the x-axis while the top and bottom edges only have one degree of freedom in the loading direction.

Fig. 4.9 show the comparison of the crack development under uniaxial tension in the x-direction. In both simulations, cracks are first initiated at the low angle grain boundaries and tend to follow the grain boundary at the beginning. However, after crack meets the junction, the transition from inter-granular to trans-granular occurs. There are also transitions starting at the middle of the grain boundaries observed in both simulations. It is interesting to note that the stresses are released on both sides of the crack. In the continuum simulation, branching phenomenon is observed in the transgranular fracture which is not present in the MD simulation. Nevertheless, one branch usually stops at once while the other continues to grow. This might be caused by underestimating the Shear's modulus or overestimating the density in the continuum model which result in an underestimated Rayleigh velocity in the material. In materials like PMMA, branching generally does not occur until about 70% of the Rayleigh velocity is reached[96].

Fig. 4.10 show the comparison of the crack development under uniaxial tension in the y-direction. Cracks, in both simulations, are first initiated and then propagate at the low angle grain boundaries in the horizontal direction. After the crack enters the inner grain, branches are observed for both simulations.

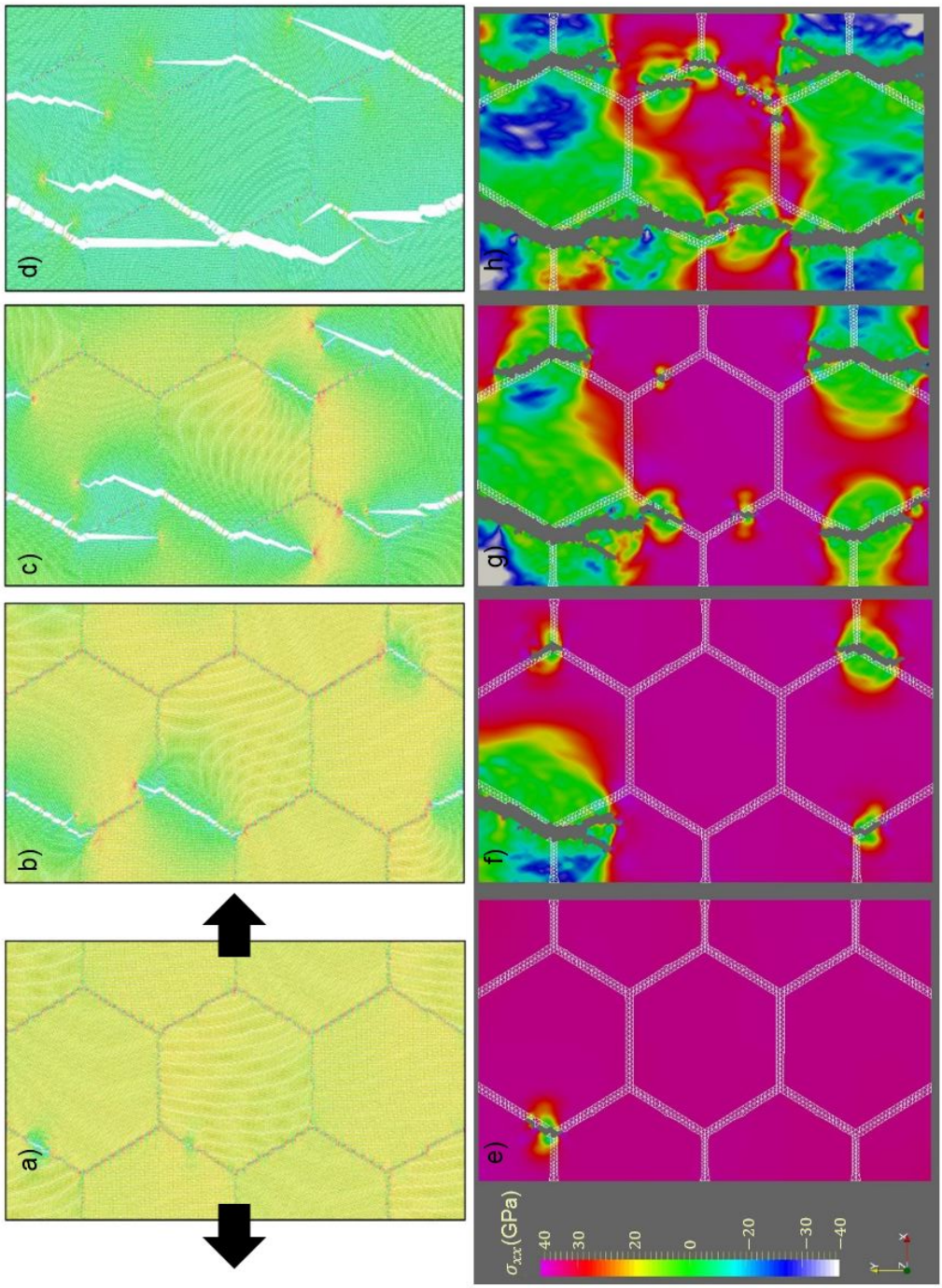

Fig. 4.9. Comparison of crack growth between a)-d) MD simulation and e)-h) continuum simulation under the uniaxial tension in the x-direction. The stress field is colored.

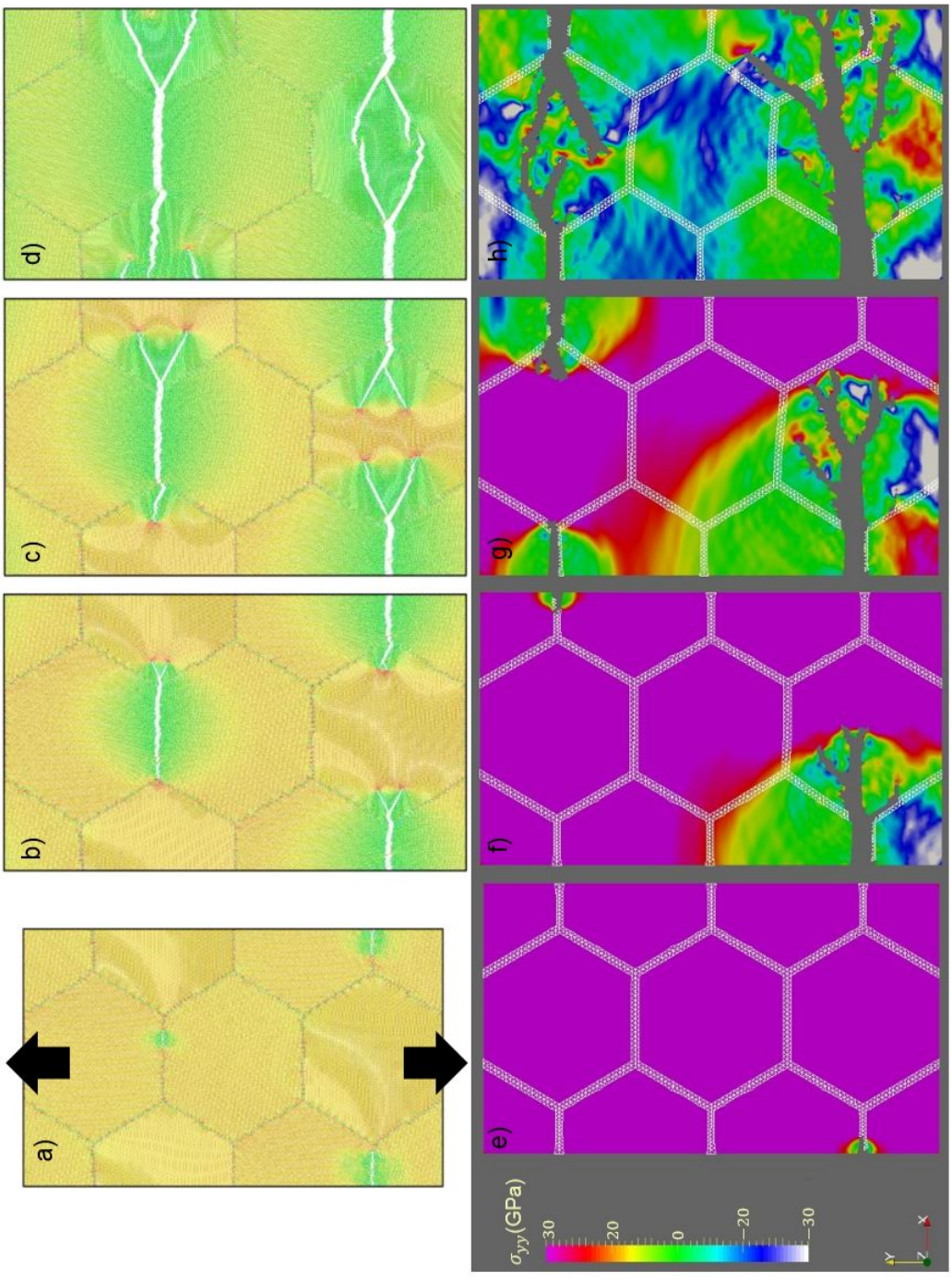

Fig. 4.10. Comparison of crack growth between a)-d) MD simulation and e)-h) continuum simulation under the uniaxial tension in the y-direction. The stress field is colored.

The stress-strain curves from both types of simulations are plotted in Fig. 4.11. For each model, $\sigma_x x$ and $\sigma_y y$ are have close values to each other. Comparing the strength from MD simulation at 45 GPa, the strength predicted by the continuum model is 10 GPa lower. Nevertheless, the trend for each curve is similar in general. The underestimated strength might be because of the way to calculate the stress. The stress in the continuum simulation is homogenized over all the unfailed elements at each time, i.e.,

To this end, the validation tests for G_c function in the Eigen-fracture algorithm are presented. The crack nucleation and propagation process predicted by MD simulations are successfully captured in our continuum computations. Excellent agreement between the MD and the proposed model predictions for the strength of the graphene polycrystal is achieved. A slight difference in terms of crack patterns might be due to the symmetry of the mesh. However, unlike the MD simulations, the proposed model is not limited by the size of the sample, the distribution of topological defects in the microstructure and dynamic loading rates.

$$\sigma_{avg} = \frac{\sum_i A_i \sigma_i}{\sum_i A_i}, \quad i \in \{intact\ elements\}, \quad A_i : weight. \tag{4.1}$$

In fact, the maximum stress in the continuum simulation can reach close to 60 GPa.

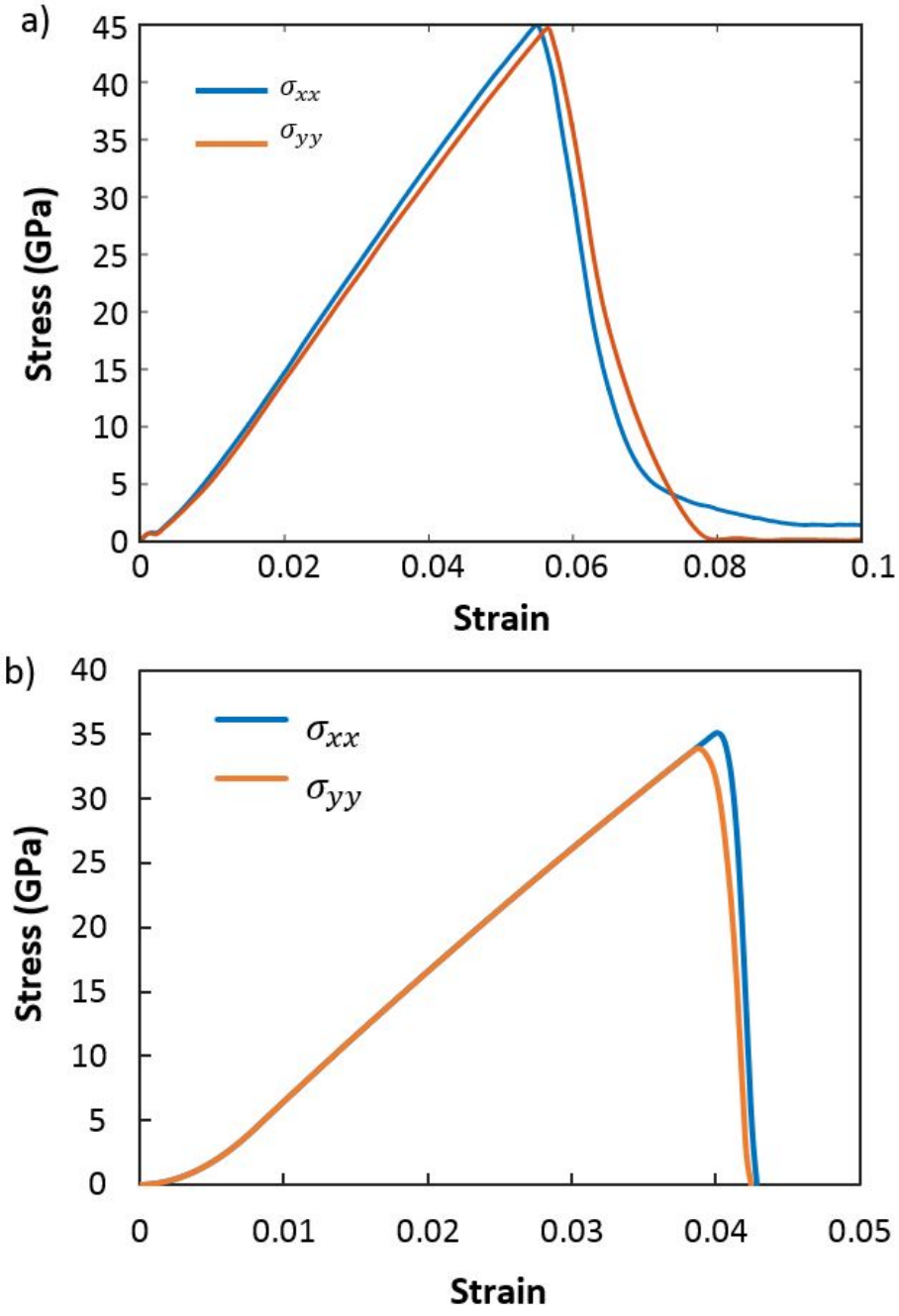

Fig. 4.11. Comparison of stress-strain curves a) MD simulation and b) continuum simulation.

4.4 Influence of strain rate on the tensile strength

A double notched polycrystalline graphene sample with a large area ($4\mu m \times 4\mu m$) is constructed to investigate the strain rate sensitivity of the uniaxial tensile strength. Two notches with $0.6\mu m$ length and 28° angle are placed at the middle of the top and bottom edges to initiate the crack locations. The sample consists of 90 equiaxed grains with randomly distributed orientations. It is discretized into 12,909 elements with finer meshes in the middle, as shown in Fig. 4.12. Therefore, the grain boundary thickness in the fine mesh region is approximately $30nm$. Uniaxial tensile loading is applied to the left and right edges as uniform but opposite displacements in the x-direction, while the top and bottom edges are locked in the y-direction.

Three cases with different pulling velocities ($v = 0.5m/s$, $10m/s$, and $100m/s$) are tested in this study while The corresponding strain rates are $10^5/s$, $10^6/s$, and $10^7/s$, respectively. The crack growths in three cases are different from each other. At the low pulling velocity, $v = 0.5m/s$, the cracks are initiated at both notches while only the crack from the bottom notch continues to propagate along the adjoining grain boundary. The crack then follows the grain boundaries that are tilted slightly from the vertical direction, as seen in Fig. 4.14. The transition from intergranular fracture to transgranular fracture occurs at a triple junction where the upcoming grain boundaries deviate heavily from the crack propagating direction. Fig. 4.15 shows the failure process of the same sample at the pulling velocity, $v = 10m/s$. In the beginning, the crack only appears at the bottom

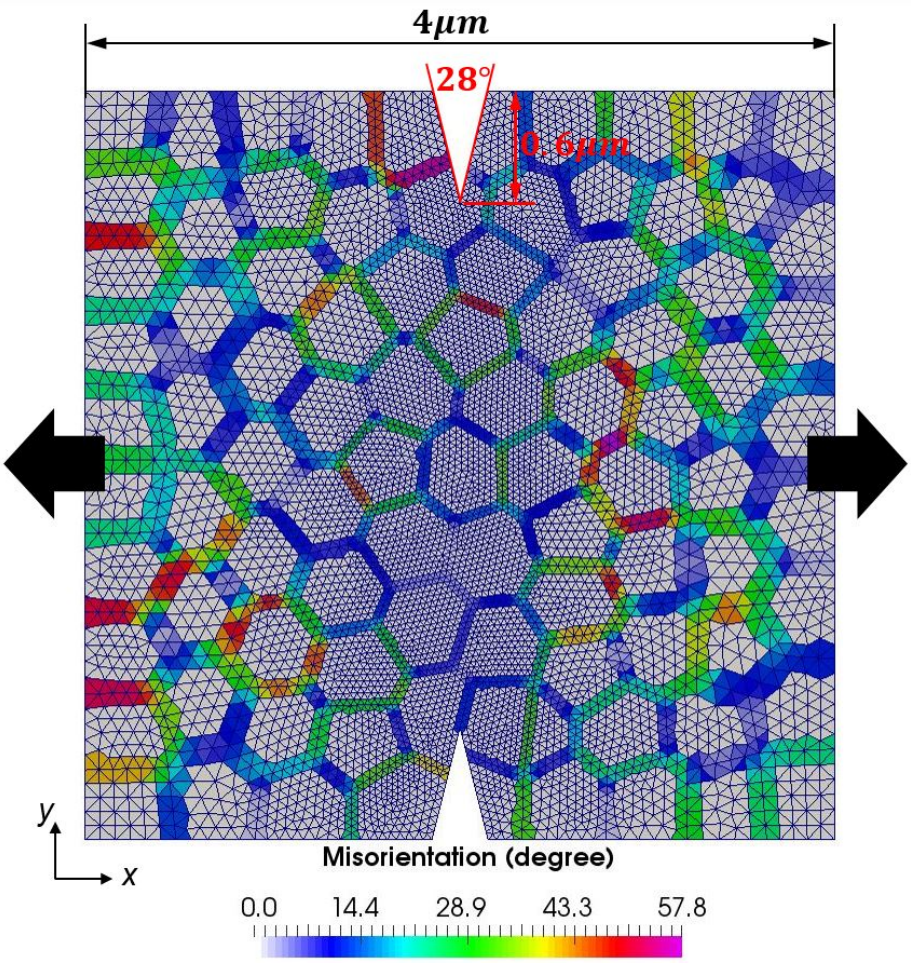

Fig. 4.12. The mesh of the notched polycrystalline graphene sample.

notch and propagates towards the top notch where no crack is observed. The crack travels along a similar path as in the previous case until branching occurs. At the same time, the top notch starts to crack. At the pulling velocity, $v = 100 m/s$, the cracks start at both notches simultaneously and travel towards each other till they meet around the center of the sample. Branches are observed near the end of the propagation for both major cracks. The cracks are mostly formed by intergranular fractures, as seen in Fig. 4.16. The

corresponding stress-strain curves for all the cases are plotted in Fig. 4.13. The maximum stress increases as the pulling velocity increases. The increase in strength, from $v = 0.5m/s$ to $v = 10m/s$, is much smaller than the one from $v = 10m/s$ to $v = 100m/s$. Meanwhile, there is an obvious increase in Young's modulus at the highest pulling velocity. According to the experimental data, the fracture toughness, K_c of the sample at different pulling rates can be evaluated in Table 4.2.

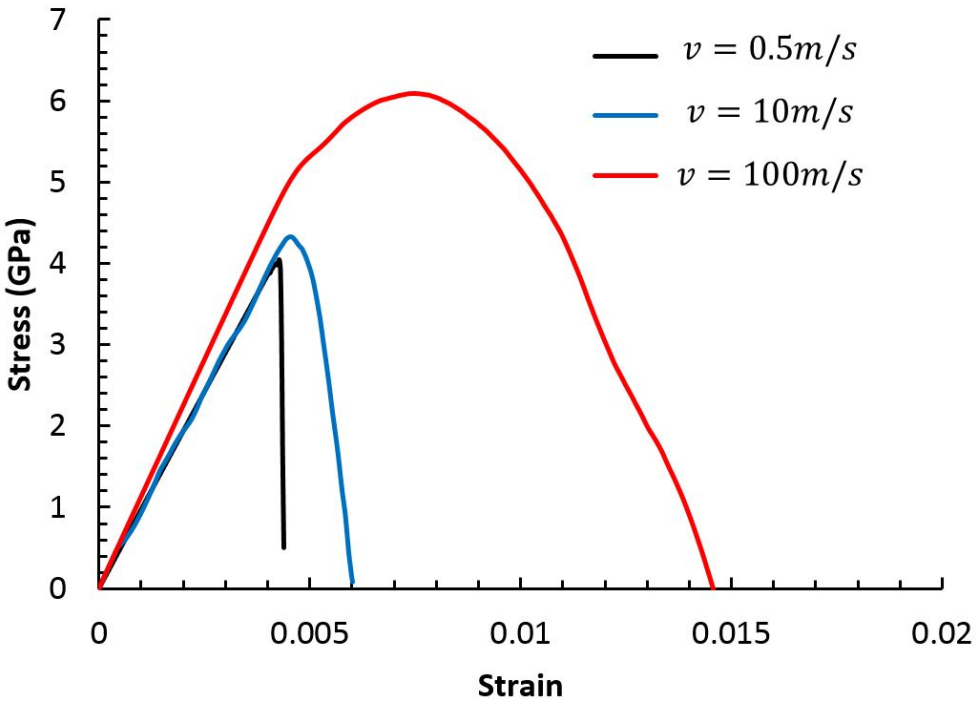

Fig. 4.13. The stress-strain curve of the uniaxial tensile test at pulling velocities of $0.5m/s$, $10m/s$ and $100m/s$.

4.4.1 Conclusion

The proposed computational framework for two-dimensional modeling is validated by comparing the predicted failure process against the results from Molecular Dynamic simulations. The critical energy release rate assigned in the Eigen-fracture model is

Table 4.2. Experimental data of critical fracture stress and Young's modulus for polycrystalline graphene with a pre-crack of length $0.6\mu m$

Pulling velocity v **(m/s)**	**Young's modulus** E **(GPa)**	**Fracture stress** σ_f **(GPa)**	**Stress intensity factor** K_c**(MPa**$\sqrt{\mathbf{m}}$**)**
0.5	971	4.05	5.56
10	987	4.33	5.94
100	1118	6.09	8.36

defined as a function of misorientation angles, $G_c(\theta)$, by interpolating the data points evaluated by the first principle simulation. The proposed fracture model successfully captures the fracture features in the mesoscale, such as the crack locations and the transition between fracture modes, which are also predicted in the MD simulations. However, unlike the MD simulations, the proposed model is not limited by the size of the sample, the distribution of topological defects in the microstructure and dynamic loading rates. Later, the strain rate effect of the dynamic tensile strength is investigated by continuum modeling a double notched polycrystalline graphene sample under uniaxial tension. The rate-dependence of the macroscopic tensile strength in two-dimensional polycrystalline graphene is found and related to the location of crack initiation sites and the particular propagation path in the microstructure.

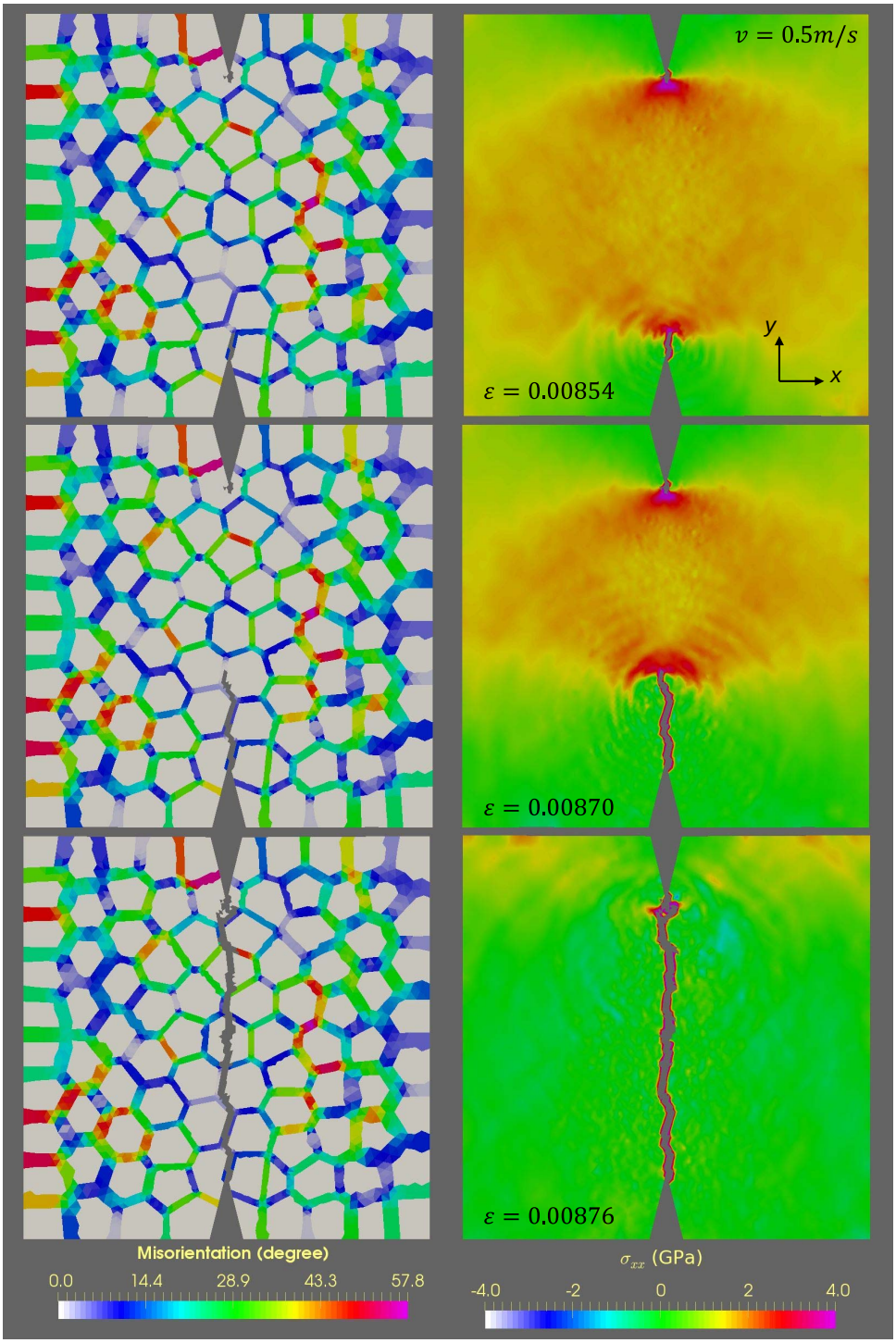

Fig. 4.14. Failure process in the double notched polycrystalline graphene (right) under uniaxial tension at pulling velocity, $v = 0.5m/s$, with the corresponding stress field (left).

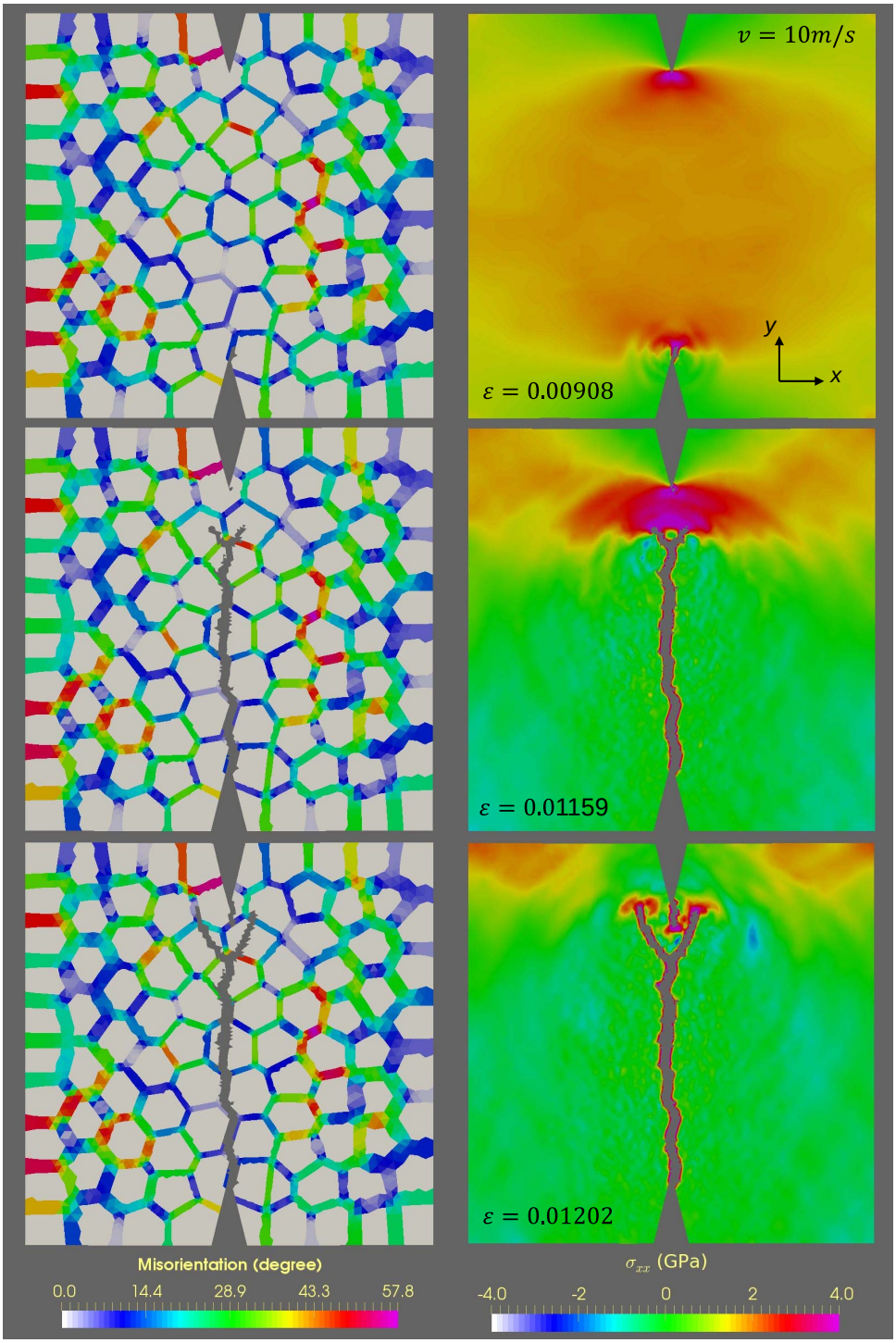

Fig. 4.15. Failure process in the double notched polycrystalline graphene (right) under uniaxial tension at pulling velocity, $v = 10m/s$, with the corresponding stress field (left).

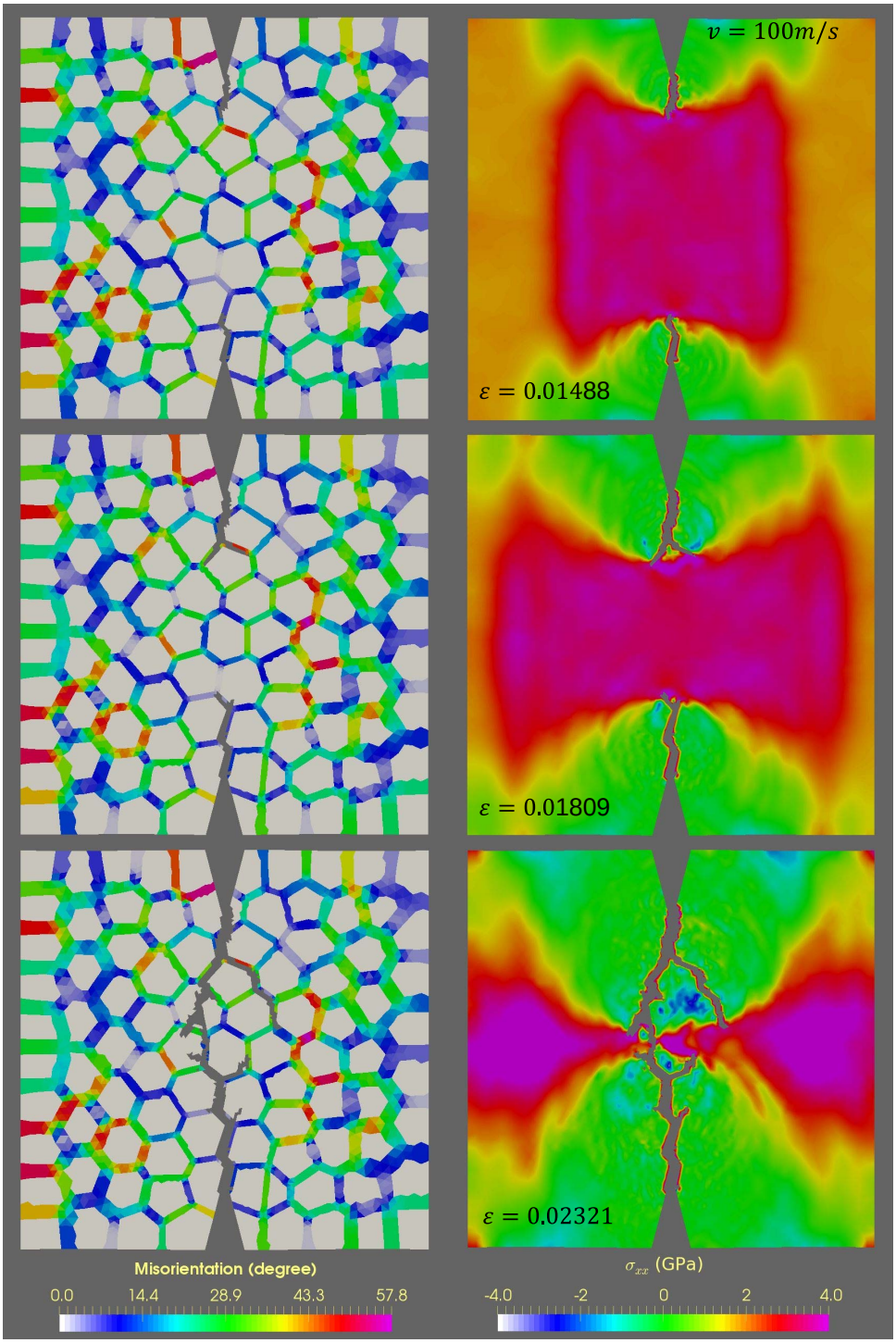

Fig. 4.16. Failure process in the double notched polycrystalline graphene (right) under uniaxial tension at pulling velocity, $v = 100m/s$, with the corresponding stress field (left).

5 Modeling dynamic failure of polycrystalline ceramic materials

5.1 Introduction

Ceramics materials, such as silicon carbide and aluminum nitride, are brittle polycrystalline materials popular in applications of defense and shielding, due to their low density, high-temperature stability, high hardness and high compressive strength. Such applications usually require a deep understanding of the material's limitation and their dynamic behavior during the failure process. It is generally recognized that the fracture responses in brittle polycrystalline materials are essentially related to their intrinsic microstructure and the defect distribution. Here, the microstructural features include grain size and shape, grain orientation, and misorientation distributions, grain boundaries, micro-voids, second phase particle, etc. Each of these micro-features has its unique contribution to affect the propagation of cracks under dynamic extreme loading conditions. Therefore, the fundamental understandings of the dynamic failure mechanisms in brittle polycrystalline materials (e.g. ceramics) at high strain rates, such as rate-dependency and porosity-strength effect, must be sought at the microscopic scale.

In addition, a detailed description of the interaction between the crack front and defects in the microstructure may enable us to better predict the macroscopic strength of ceramics under various dynamic loading conditions.

Experimental studies of strain rate dependent compressive strength in ceramics, such as SiC[106,119] and AlN[26,53,54], have focused on the macroscopic responses in a qualitative manner. Their findings regarding the failure process and strain rate effect can be summarized as follows: 1) The subcritical micro crack propagates and coalesces before macro crack splits; 2) Intergranular fracture is preferred under quasi-static loading conditions, while transgranular fracture becomes dominant as the strain rate increases and fragment size turns to be smaller; 3) There exists a critical strain rate (e.g., $1000s^{-1}$) beyond which the ultimate compressive strength is strongly sensitive to the strain rate. These observations and post-analysis characterize the dynamic fracture response of brittle polycrystalline structures at the macro-scale and provide evidence about the microstructure effects. Nevertheless, due to the limitations of experimental diagnostics, there are very few, if any, experiments that perform quantitative and real-time analysis at the microstructure level. In order to develop and test theories for the dynamic failure mechanisms in brittle polycrystalline materials, physics-based computational modeling and simulations are indispensable. For instance, the wing-crack array model[24,86,106,119] utilizes the local stress intensity as the failure criterion, which is defined as a function of micro-flaw size and spacing. The rate-dependent effect is included by the dependence of a dynamic intensity factor on the crack growth rate[51,101]. Their model captures the dynamic damage evolution to some degree. However, the

crack paths, intergranular and transgranular fracture patterns are not explicitly solved. Other topological defects in the microstructure including grain boundaries and grain orientations are not explicitly accounted for.

Additionally, the intergranular fractures are often modeled using a cohesive surface approach within finite element formulation[40,64,80,87,109,128,129]. The deformation and failure of the grain boundaries are governed by a cohesive law. The crack nucleation and propagation are controlled by the maximum normal traction and the critical stress intensity. Nittur et al.[87] investigated the dynamic fragmentation of ceramic under compression. They have found that the material remains intact mainly when peak compressive strength is achieved but shows catastrophic damage shortly after the peak. Furthermore, Zavattieri et al.[129] introduce a Weibull distribution at grain boundaries to account for the misorientation and the presence of impurities. It is worth mentioning that the statistical approach is also applied to study the influence of pre-existing flaws using the cohesive method[32]. Their results show that integrating more microstructural information in the model provides a more realistic crack pattern and damage kinetics. Nevertheless, most of the cohesive zone models for polycrystal structures only predict the intergranular fracture pattern since it becomes computationally expensive to include transgranular fractures. Also, the mesh spacing and orientation restrict the crack path to follow the element interfaces. It has been stated out that the cohesive zone models suffer from mesh-dependence and the lack of strict convergence properties[85].

Instead of using stress-related criteria, the fracture can be modeled through energy minimization[14,15]. Fracture models derived from a variational formulation[21,108] address

the conservation issue instinctively by an energy minimization process. The phase field model[3,16,18,28,29,65,66] approximate the discontinuities by a secondary field, which is independent of the displacement field and can be calculated implicitly. An order parameter is introduced along the crack to accommodate the material transition from the intact to the damaged state. However, the material properties of the damaged material need to be estimated, and the order parameter function through the fracture thickness must be calibrated against available experimental data. The polycrystalline phase field model developed by Clayton and Knap[28] is capable of capturing the change of crack paths and bulk material properties by adjusting the grain boundary properties. In order to predict the strain rate sensitivity in the dynamic response of brittle materials, rate-dependent phase field model needs to be further developed.

Another variational approach to fracture is deducted using the Eigen-fracture scheme based on element erosion or material point failure[75,76,95]. Similar to the phase field model, the discontinuities are approximated using the Eigenstrain, which is widely used in mechanics to describe deformation modes that cost no local energy. Instead of concerning the energy minimization globally, the Eigen-fracture approach regards fracture as a dissipative process with dissipation located at the crack front[69]. The crack front velocity obeys a kinetic law regarding the local driving force, and the entire trajectories of the system, including the crack paths, follow as minimizers of energy-dissipation functionals[84]. For brittle materials, the dissipation potential can take a simple rate-independent form as $G_c|v|$, where G_c and v are the critical energy release rate and the crack front velocity, respectively. The energy release rate attendant to the failure of an

element (or material point) is estimated by a local strain energy averaging procedure in the $\epsilon-$neighborhood, and elements (or material points) are failed when the attendant energy release rate exceeds G_c as a minimizer of the energy-dissipation functional. In this regard, the propagation of the crack can be related to the combination and competition of various energy dissipation pathways in the materials microstructure. Various types of defects, such as pre-existing microcracks and grain boundaries, can be considered explicitly as potential energy sinks to minimize the local energy when stress flow passes by.

5.2 Simulations and results

In this work, we study the dynamic failure process of ceramic material (6H-SiC) under compression. The experiment selected is the uniaxial unconfined dynamic compression test performed using the split-Hopkinson pressure bar(SHPB)[99]. Uniaxial compression tests performed using a split-Hopkinson pressure bar (SHPB) have been widely used for determining the dynamic compressive strength and strain-rate sensitivity of various materials in the strain rate range from $10^2 - 10^4 s^{-1}$. A schematic of the typical experimental setup is shown in Fig. 5.1. The SHPB consists of an incident bar and a transmitter bar, with a small specimen placed between them. At the beginning of the test, a projectile impacts the open end of the incident bar. The resulting compressive pulse which propagates toward the specimen. Due to the interfaces between the specimen and the adjacent bars, the loading pulse echoes within the specimen. There is a transmitted pulse is sent into the transmitter bar, and a reflected pulse is sent back to the incident

bar. The incident and transmitter bars are designed to remain elastic throughout the test, as is the striker bar.

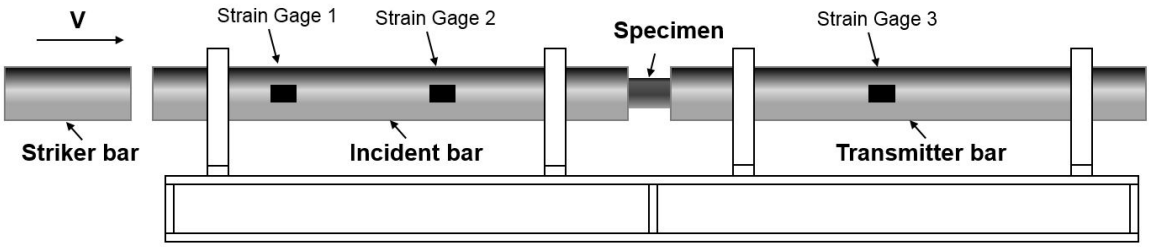

Fig. 5.1. Schematic of the uniaxial compression test using Split-Hopkinson pressure bar test.

In the experiment, three resistance strain gages are used to measure the pressure waves traveling in the bars. Two separated gages are placed on the incident for measuring the incident pulse and the reflected pulse, respectively. While the transmitted pulse is measured by the third gage placed on the transmitter bars. Then these measured raw data can be used to calculate the axial stress history of the specimen by applying the one-dimensional elastic wave theory. The numerical simulation, on the other hand, provides the stress state at any point in the specimen directly. Thus, it is not necessary to model the incident bar and transmitter bar explicitly. Instead, proper boundary conditions applied at the interfaces gives more accurate displacement control and reduces the computational cost. The details of the boundary conditions used in our simulation are presented in the following section.

Fig. 5.2 presents the real-time failure process in a SiC sample under the SHPB test captured using the high-speed camera, and the corresponding result. The visible fracture features on the imaged surface appear first near the front and back surfaces right

before the peak stress is reached. In image 4, approximately $3\mu s$ after peak stress, longitudinal cracks start to grow across the sample, which causes the stress in the material to collapse further.

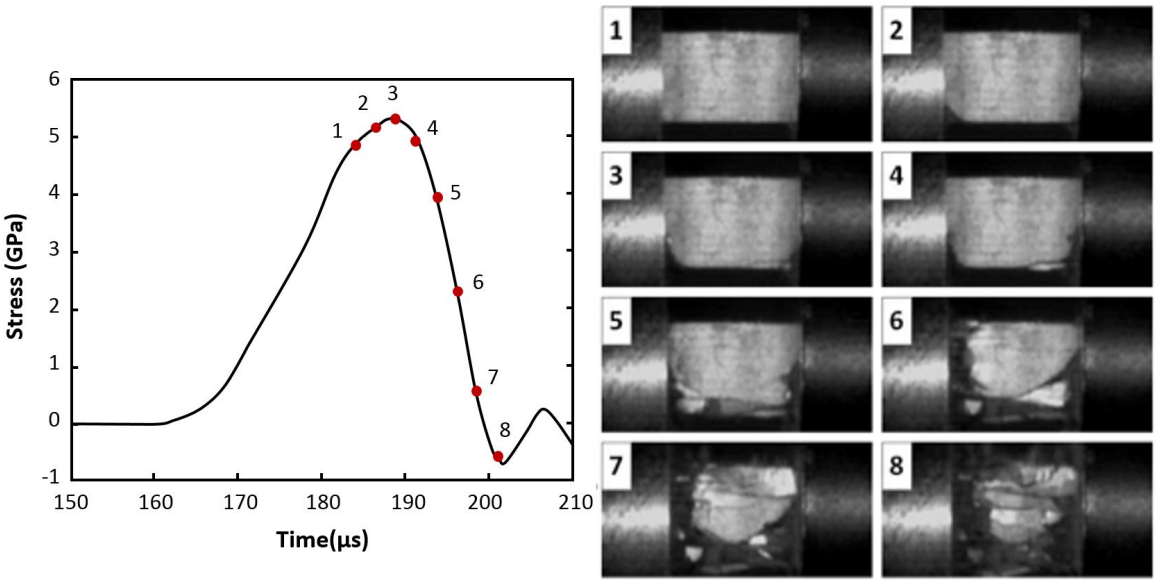

Fig. 5.2. Stress-time history with high speed camera images of the failure process of SiC under uniaxial dynamic compression. Note the images(right) are captured with an inter-frame interval of 3 μs while the corresponding stress levels are marked by red dots in the stress curve(left).

Meanwhile, the strain rate effect can be found from the results of the SHPB testing. In many ceramics, the material has a higher strain rate dependence of the strength at high strain rates, see Fig. 5.3.

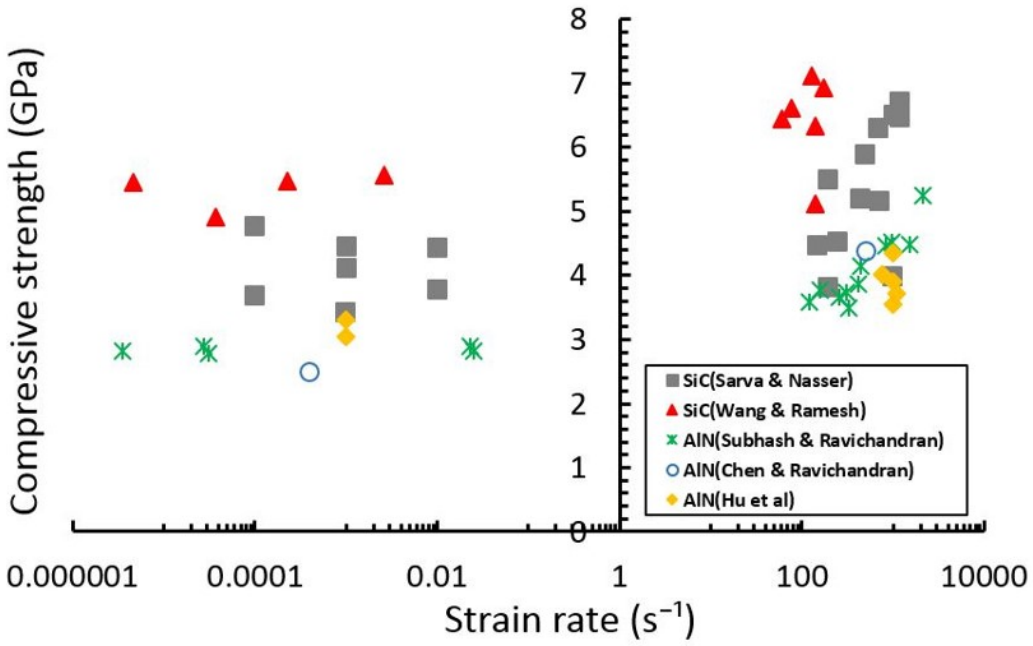

Fig. 5.3. Effect of strain rate on the compressive strength of ceramic materials (SiC and AlN) measured by SHPB tests.

In this section, a low-strain-rate compression test of a polycrystal with weak grain boundaries is performed first as the benchmark case. Then, a typical simulation for the high-strain-rate tests is given to demonstrate the setup of the test configuration, the material properties, boundary conditions and results. A convergence study of the proposed algorithm as refining the discretization is presented to show the mesh-independency. Finally, by controlling the microstructure of the specimen and loading conditions, we investigate the influence of the microstructure on the dynamic compressive failure mechanisms of 6H-SiC, including porosity effect, strain-rate dependence and the influence of misorientation distribution.

5.2.1 Benchmark test

In order to test the fracture mode sensitivity of our proposed fracture model, a benchmark test is performed first with an engineered grain boundary strength, $G_c^{gb} = 10\% G_c^{grain}$ under a static compressive loading condition, $\dot{\varepsilon} = 0.001 s^{-1}$. The cubic polycrystalline sample ($1mm \times 1mm \times 1mm$) consists of 90 grains created by Poisson's Voronoi tessellation and is discretized into 90,590 elements and 17,000 nodes, as seen in Fig. 5.4 a). Fig. 5.4 b)-f) shows the failure process in the benchmark test. The cracks first appear on the loading surface and then propagate mainly along the grain boundaries. In the end, the whole sample fragments into small pieces. The predicted fracture features is well-expected, which is similar to the fracture of ceramic materials under static compression, i.e., intergranular fractures and fragmentations. To this end, it is confident to say that the proposed fracture model has the rate sensitivity of fracture modes under compression.

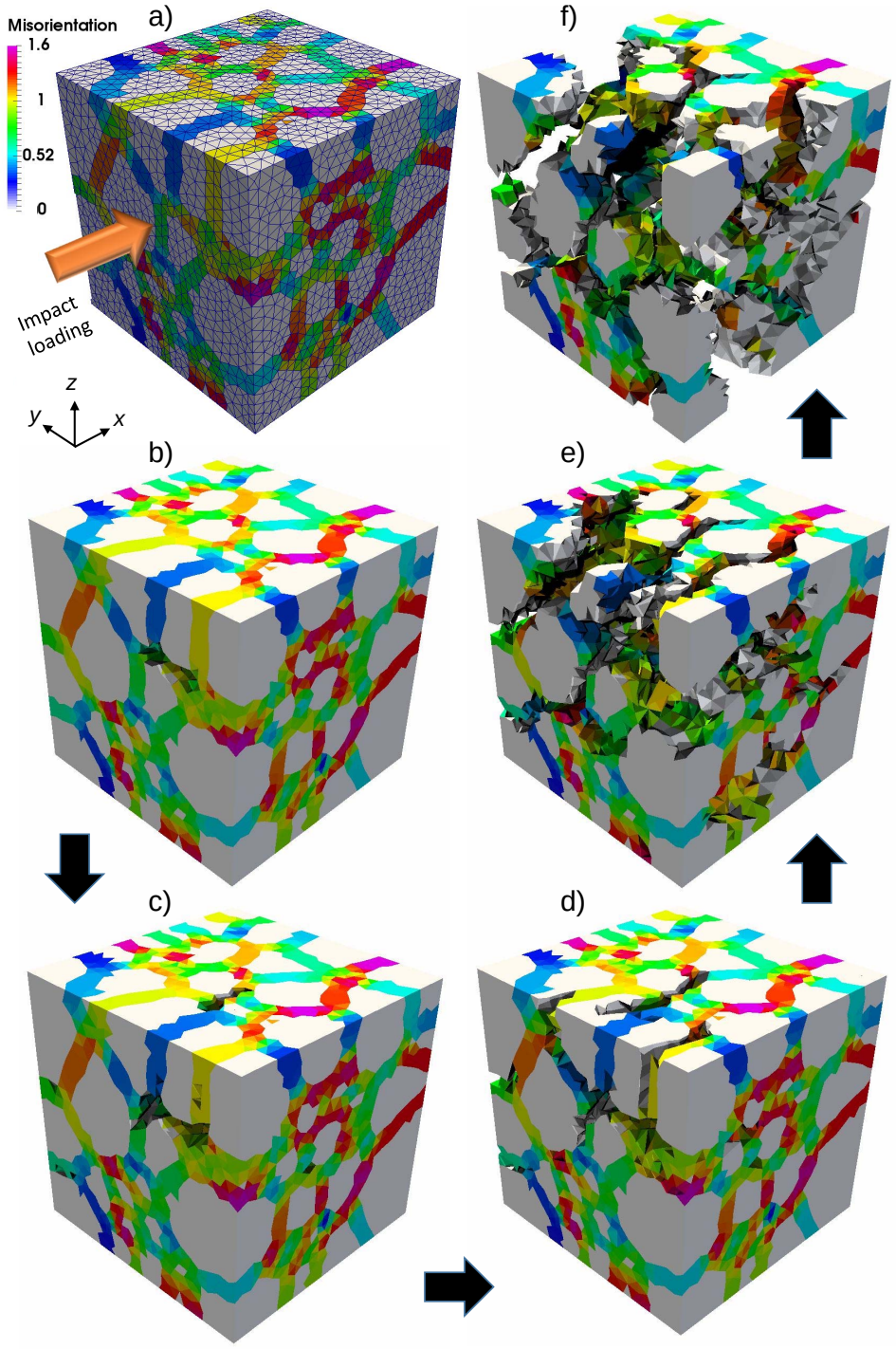

Fig. 5.4. Benchmark test with low grain boundary strength, $G_c^{gb} = 10\% G_c^{grain}$, and low strain rate, $\dot{\varepsilon} = 0.001 s^{-1}$: a) meshes of the cubic sample colored in misorientation, and b)-f) failure process.

5.2.2 Validation and convergence tests

The reconstructed specimen and the boundary conditions are illustrated in Fig. 5.5(a). The nodes on the front surface are assigned with a linearly increasing velocity in the $x-$direction up to a constant value as shown in Fig. 5.5(b), while the nodes on the back surface are confined in the y-z plane. The polycrystalline specimen consists of 100 equiaxed grains, which aggregate a cuboid with dimensions of 1000μm $\times$ 600μm $\times$ 600μm. The average size of the grains is estimated as 150μm. In this simulation, the specimen is modeled by 1,929,325 material points and 339,855 nodes. The material properties and model parameters used in the simulations are collected from literature and listed in Table 5.1.

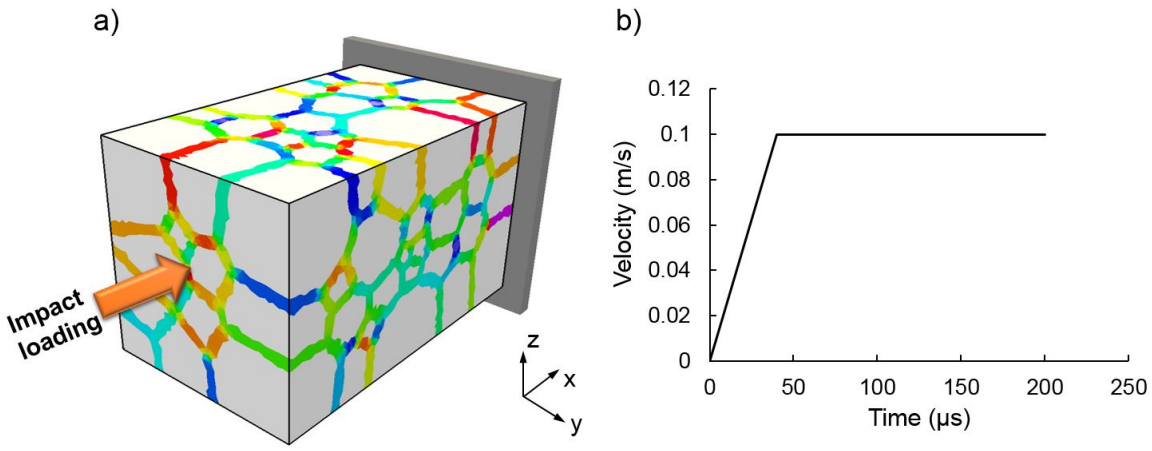

Fig. 5.5. a) Reconstructed specimen with loading direction and b) Velocity profile of boundary nodes on the loading surface.

Table 5.1. Parameters used in the SiC compression test

Parameter	**Value**	**Definition**
C_{11}	501	
C_{33}	553	
C_{44}	163	Elastic constants [GPa]
C_{12}	111	
C_{13}	72	
K_0, K_t	231, 185	Bulk modulus for the intact/failed material[GPa]
μ_t	5	Shear modulus for the failed material [GPa]
ρ	3.21	Density [g/cm^3]
K_{IC}	10	Critical fracture toughness for single crystal [MPa$\sqrt{m}$]
θ_0	90	Reference misorientation angle in G_c^{gb} function [degrees]
c, m	1.5, 0.8	Grain boundary weakening constants
ϵ	$1.5h_e$	Epsilon neighbor size, where h_e is the element size

Fig. 5.6 illustrates a representative simulation of the dynamic failure process in a brittle polycrystalline SiC with 5% porosity at strain rate $100s^{-1}$. As shown in Fig. 5.6(a), the cracks first initiate at the weak grain boundaries near the front and back surfaces of the specimen. As stress increases, internal grain boundaries start to fail. While the intergranular cracks propagate, the transition from intergranular fracture to transgranular fracture occurs as demonstrated in Fig. 5.6(b) due to a large amount of energy deposited in the material in a short time. Wing cracks as a result of the crack turning from the grain boundaries to the interior of the grains are developed during this stage. The transgranular fracture grows along the loading direction and creates longitudinal splits from

the peripheral surfaces in Fig. 5.6(c), which agrees well with the experimental observations[119]. The direction and number of the macroscopic splits are intimately related to the geometry and the stress concentration in the specimen. Later, the transgranular fracture connects the spatially dispersed grain boundary cracks into a network. As a result, the structure is divided into a number of pillars. Finally, the individual components comminute rapidly until the entire structure fails as the strain energy accumulates, Fig. 5.6(d).

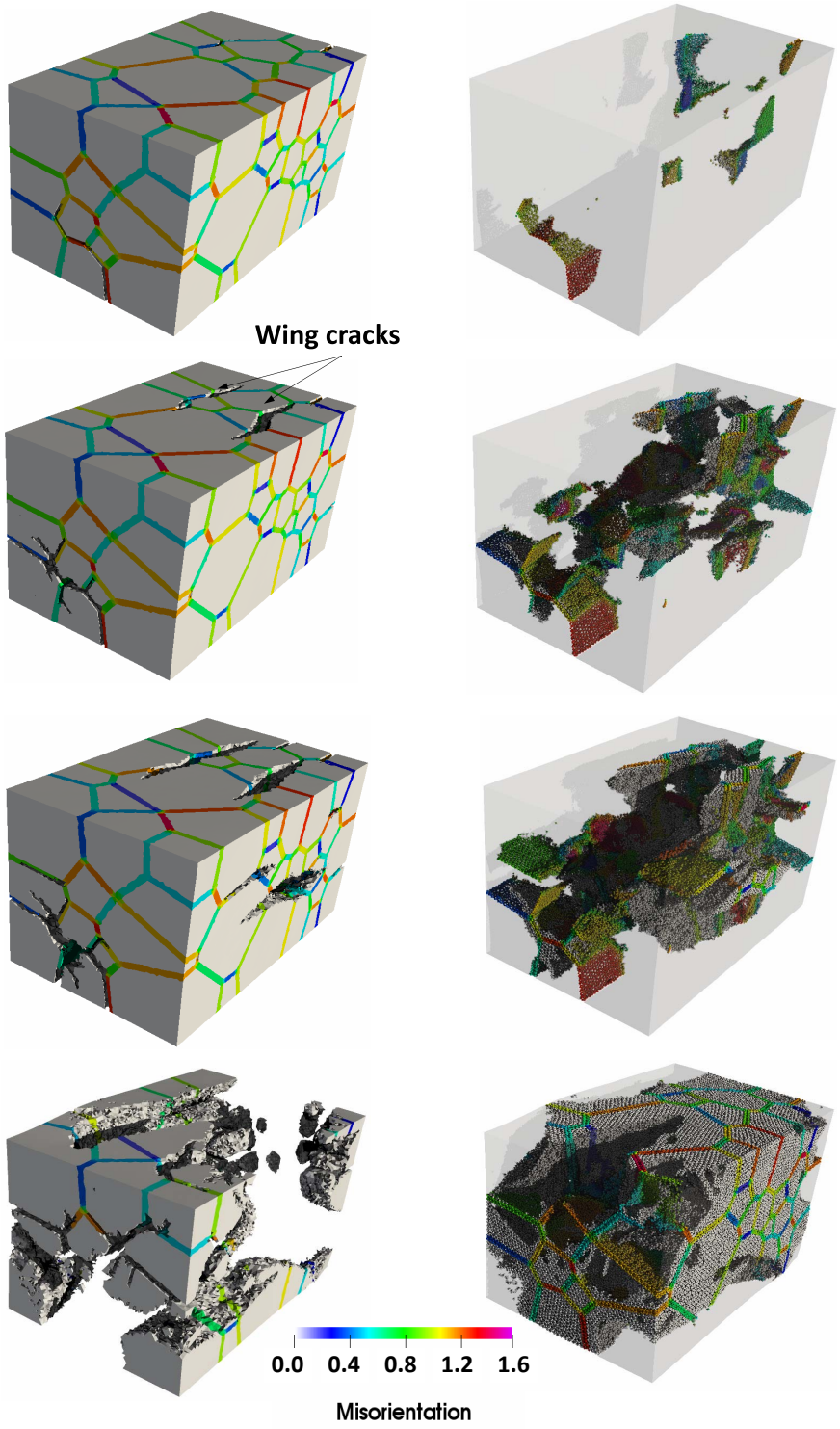

Fig. 5.6. Fracture evolution under uniaxial compression: a)Crack initiation, b)Crack propagation, c)Interaction between cracks and d)Comminution.

The corresponding stress history of the 6H-SiC specimen is shown in Fig. 5.7. The stress along the loading axis is homogenized over the entire domain. As observed in the figure, the predicted compressive strength of the porous SiC specimen at strain rate $100s^{-1}$ is 4.58 GPa. The residual stress after the peak is due to the resistance to deformation in the failed material. Comparing Fig. 5.6 to Fig. 5.7, it is interesting to note that the stress continues to build up even when multiple grain boundary cracks are developed at the failure stage (b). The increase in stresses gradually slows down as the transgranular fracture propagates. When individual cracks coalesce into a network, the stress approaches its maximum value towards a sudden decrease due to the material comminution. It is evident that a detailed description of the crack propagation in the microstructure may shed light on a mechanistic understanding of the macroscopic strength of the material at high strain rates.

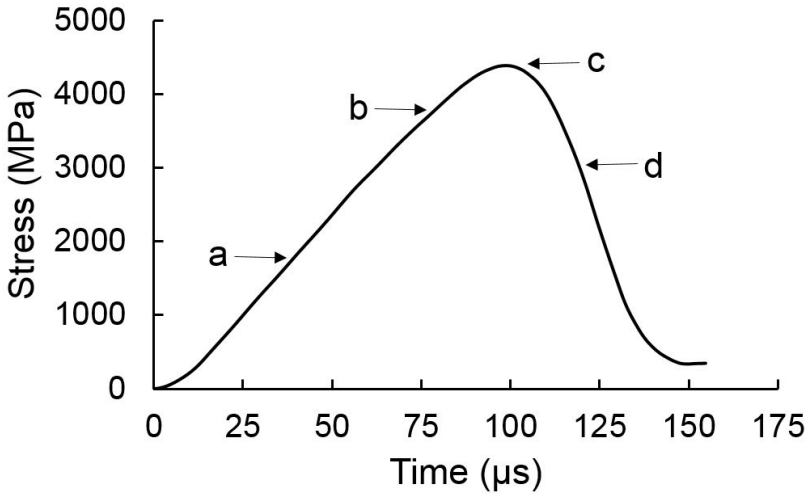

Fig. 5.7. Stress history for strain rate at $100s^{-1}$. The a, b, c and d locations pointed out in the stress curve correspond with the series of facture images shown in Fig. 5.6.

A convergence study is performed to show the mesh-independent property of the algorithm. Fig. 5.8 shows the final strength of 6H-SiC under compression tests at strain rate $10^4 s^{-1}$ versus the mesh size. The convergence plot exhibits a well-defined asymptotic regime where the predicted strength approaching the experimental measurement[106], i.e., 5.82 GPa. Fig. 5.9 shows a series of images for the comparison of the crack paths in different discretizations. Each row illustrates the development of the intergranular and transgranular crack surfaces in the sample and the deformed configuration as the stress reaches the peak value. It is expected that the failure zone (the collection of failed material points) becomes thinner as the discretization is refined, which enhances the resolution of the predicted crack surfaces in the domain. For instance, one large failure zone or coalesced crack in the coarse mesh may be resolved with two parallel refined cracks in the fine mesh. In general, the fracture patterns are similar on the whole and the elimination of the spurious discretization-dependent artifacts in the simulations is noteworthy.

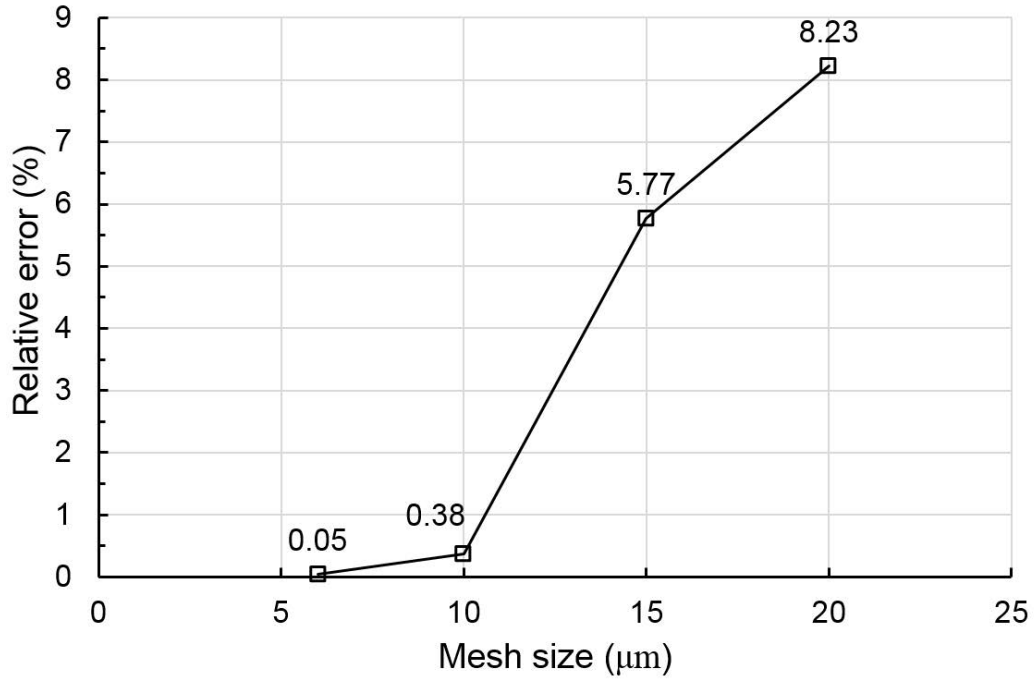

Fig. 5.8. Convergence plot of final strength.

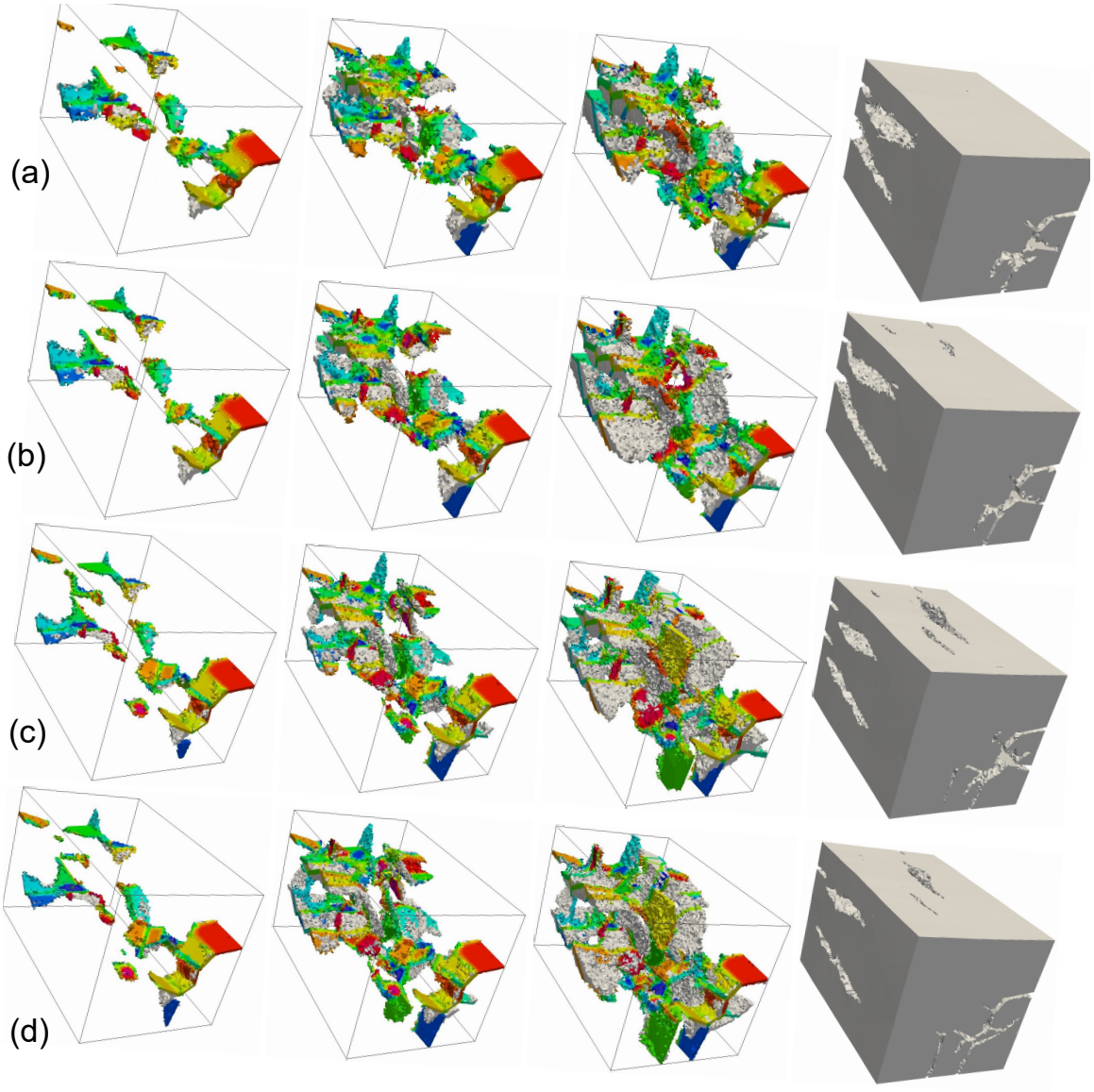

Fig. 5.9. Comparison of the crack growth in different discretizations with mesh sizes equal to (a) $20\mu m$; (b) $15\mu m$; (c) $10\mu m$; (d) $6\mu m$. The first three columns are the evolution of the crack surfaces in the sample colored by the misorientation angle to demonstrate intergranular and transgranular fractures. The last column is the deformed configuration as the stress reaches the peak value.

5.2.3 Influence of porosity on the compressive strength

The influence of porosity on the uniaxial strength has been observed and measured in many engineering brittle materials. The failure strength, in tension and compression, drops with the presence of voids or porosity[9,77,105]. The theoretical explanation can be drawn by treating the voids as cracks in a periodic array. Thus, the degraded strength is determined by the shape and spacing of the voids. In the perspective of continuous media, the porosity also affects other mechanical properties of the material, such as the elastic modulus, Poisson's ratio, and fracture energy, etc. Due to the complexity of spatial void distributions in the real material and the limitation of measuring techniques, simple empirical models are commonly used to describe the porosity-strength dependency. The degradation of the failure strength, based on experimental data on various materials, can generally be expressed as a power law function or an exponential function of the porosity. For instance, the well-known power law expression proposed by Bal'shin[9] for uniaxial tensile strength follows as:

$$\sigma_{tp} = \sigma_{t0}(1-p)^b, \tag{5.1}$$

where σ_{tp} is the uniaxial tensile strength of the material with a porosity p, σ_{t0} is the ideal tensile strength of a nonporous media, and b is an empirical constant. The value of b was found to be between 3 and 6 for metal ceramics. Similarly, Ryshkewitch[105] obtained an exponential function from a study of the compressive strengths of Al_2O_3 and ZrO_2:

$$\sigma_{cp} = \sigma_{c0}e^{-kp}, \tag{5.2}$$

where σ_{c0} is the ideal compressive strength of a nonporous material and k is an empirical constant. The value of k was found to be above 5 for ceramics.

In this work, we employ the proposed model to derive a quantitative relationship among failure strength, porosity, and spatial void distribution in the polycrystalline brittle materials. The voids with an averaged size in $O(1)\mu m$ are modeled explicitly by material points with the void volume fraction set to be 1. The investigation takes account of various porosity levels at 0%, 5%, 10% and 20% and two spatial distribution types in the bulk material. In specific, we consider the spatial void distribution type by allocating 90% of the voids along the grain boundaries (biased spatial distribution), while the other with the voids uniformly distributed throughout the domain (uniform spatial distribution). The dimensions and grain structure of the specimen is the same as the one described in the representative simulations at strain rate $100s^{-1}$. The normalized stresses are plotted in Fig. 5.10 to show the strength degradation as the porosity increases. It is evident from the comparison between two different distributions that the specimen with a biased spatial distribution is more sensitive to the change of porosity. As illustrated in the plots, the results of the biased case can be fitted to the Balshin's model with empirical constant $b = 6$ or $k = 6.5$ for the Ryshkewitch's model. The calibrated empirical constants are in the range of ceramic materials. Indeed, the biased void distribution may be considered as a more realistic one due to the fabrication process of real ceramic materials, in which the sintering and heat treatment usually leave more voids at the grain boundaries rather than inside of the grains.

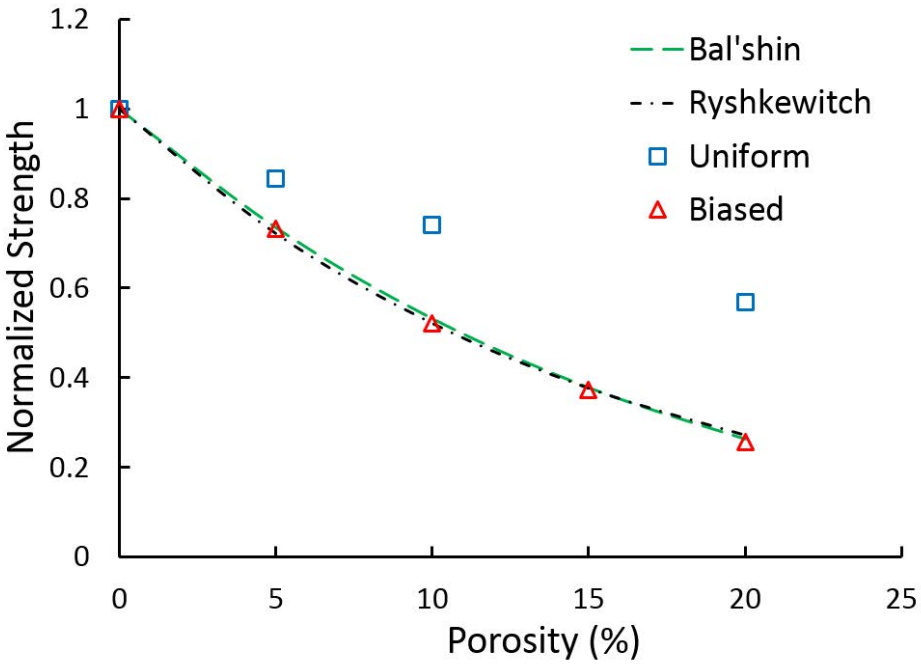

Fig. 5.10. Comparison of strength decaying between simulation results and empirical models.

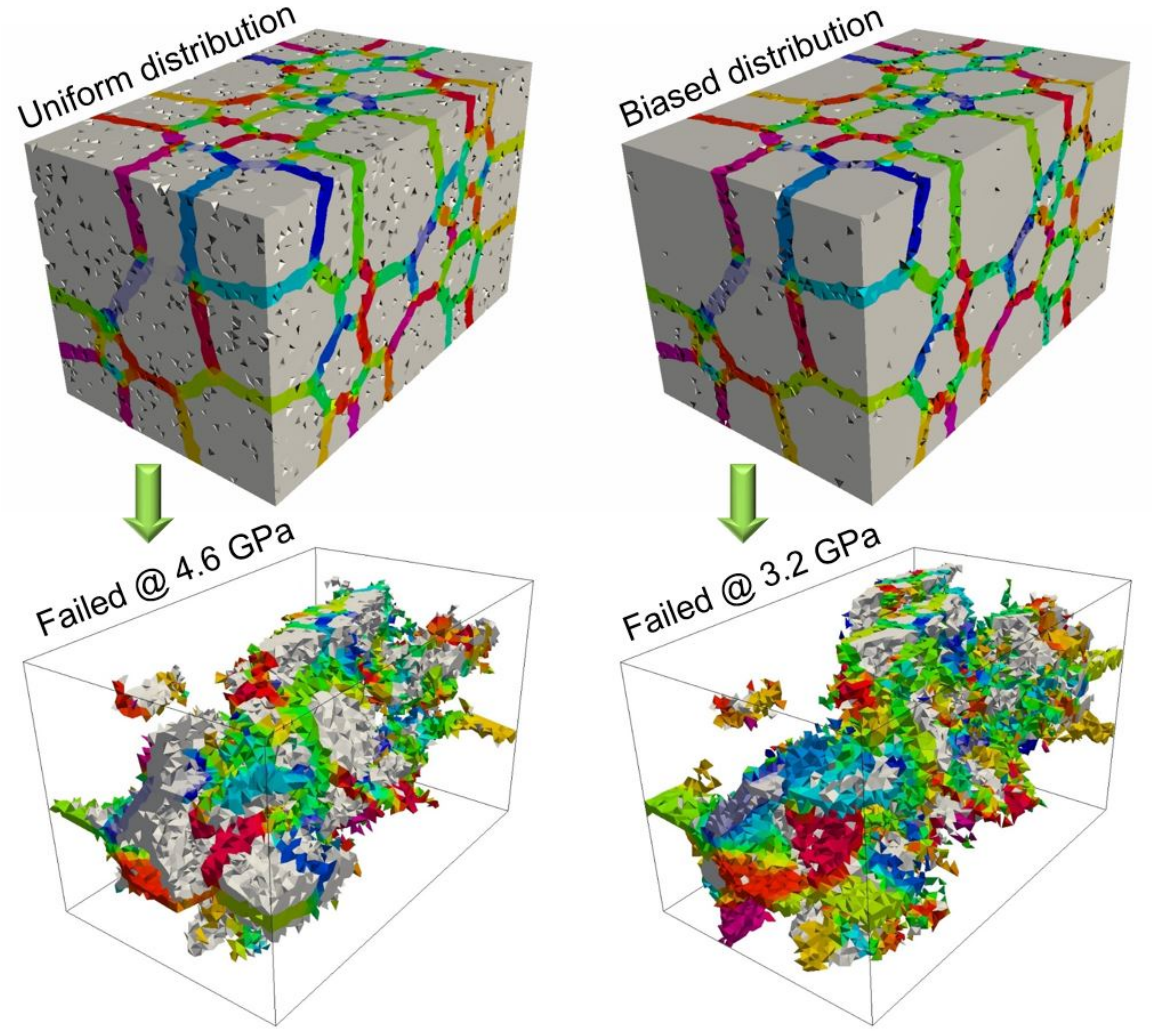

Fig. 5.11. Comparison of fracture surfaces at the failure strength between uniform and biased void distribution.

Fig. 5.11 compares the internal crack surfaces in a sample with 10%-porosity between the biased and uniform void spatial distributions. At this particular moment, the regional cracks are connected along the loading direction and the peak stresses are reached in the sample. The total volume of the failed material points calculated in our simulations for these two void distribution types is almost equivalent. However,

as shown in Fig. 5.11, the transgranular fracture pattern is more evident in the specimen with uniform void distribution. It can be further confirmed in the plot of the volume fraction ratio of transgranular to intergranular fractures versus the porosity, Fig. 5.12. At 10% of porosity, the volume fraction of the transgranular fracture to the total volume of the failed material points is 35% in the specimen with a uniform void distribution and 23% for the biased case. It is noteworthy that the trans-to-intergranular fracture ratio decreases as the porosity increases, while the one for the biased void distribution is more sensitive to the porosity level.

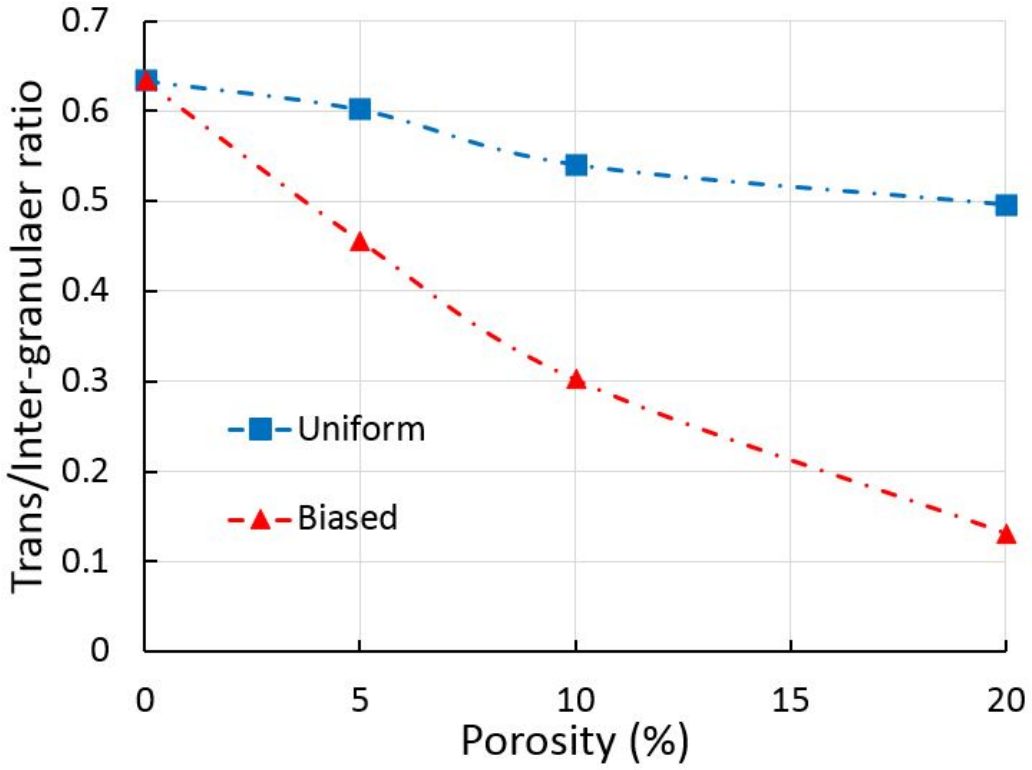

Fig. 5.12. Comparison of trans/intergranular ratio at the failure strength between uniform and biased void distributions.

A micromechanical interpretation can be drawn in terms of the stress concentrations in polycrystalline materials. Due to the heterogeneity of the microstructure and the anisotropic material properties, the stress concentration predominantly occurs at the grain boundaries. In addition, the voids also cause stress concentrations in the surrounding material. In general, the voids at the grain boundaries make them more vulnerable to the fracture. There is experimental evidence showing that the void at the triple joint in the sintered ceramic materials is the common initiation site of a crack. Therefore, it is favorable for the material to develop more intergranular fractures as more voids allocate at the grain boundaries at medium strain rates, which limits the materials capability for the energy dissipation and give rise to a quick drop of the compressive strength.

5.2.4 Influence of strain rate on the compressive strength

The rate dependence phenomenon of the compressive strength of brittle ceramic materials, such as SiC and AlN, have been studied experimentally by multiple research groups[27,54,106,115,119]. Their experimental data indicates the strength of the material becomes significantly sensitive to the strain rate beyond $1000s^{-1}$.

A series of numerical experiments are performed by using the proposed model to investigate the strain rate effect on the fracture mode and the final strength in the microstructural level. The specimen, with 5% porosity and the biased void spatial distribution, is exercised under dynamic compressive loading conditions at various strain rates,

ranging from $10s^{-1}$ to $10000s^{-1}$. The geometry, boundary conditions and parameter settings are the same as the example of simulations presented in Section 5.2.2, which is in fact a part of this strain rate study as the result in $100s^{-1}$.

Fig. 5.14, Fig. 5.15 and Fig. 5.16 show the predicted crack growth in the SiC sample under dynamic compression at strain rate $1000s^{-1}$, $5000s^{-1}$ and $10000s^{-1}$ respectively. At all the strain rates, the cracks first appear at the grain boundaries and propagate in the loading direction accompanied by the transition from intergranular fracture to transgranular fracture. The longitudinal splits from the peripheral surfaces are observed for all the cases, which agrees well with the experimental observations. In general, the main crack patterns at different strain rates are similar while more transgranular cracks are observed as the strain rate increases. The corresponding stress curves are plotted in Fig. 5.17.

The nonlinearity of the strain rate dependence is characterized by our model in Fig. 5.13 in comparison with the experimental measurements by Sarva and Nasser[106]. It evidently shows that there is a critical strain rate between $100s^{-1}$ and $1000s^{-1}$ predicted by the proposed model, which agrees well with the experimental findings. Below the critical strain rate, the compressive strength of the material is not sensitive to the strain rate. As the strain rate is higher than $1000s^{-1}$, a drastic increase in the compressive strength can be observed. It is worth mentioning that neither the constitutive model nor the fracture model is defined to be rate dependent in our simulations. Therefore, the

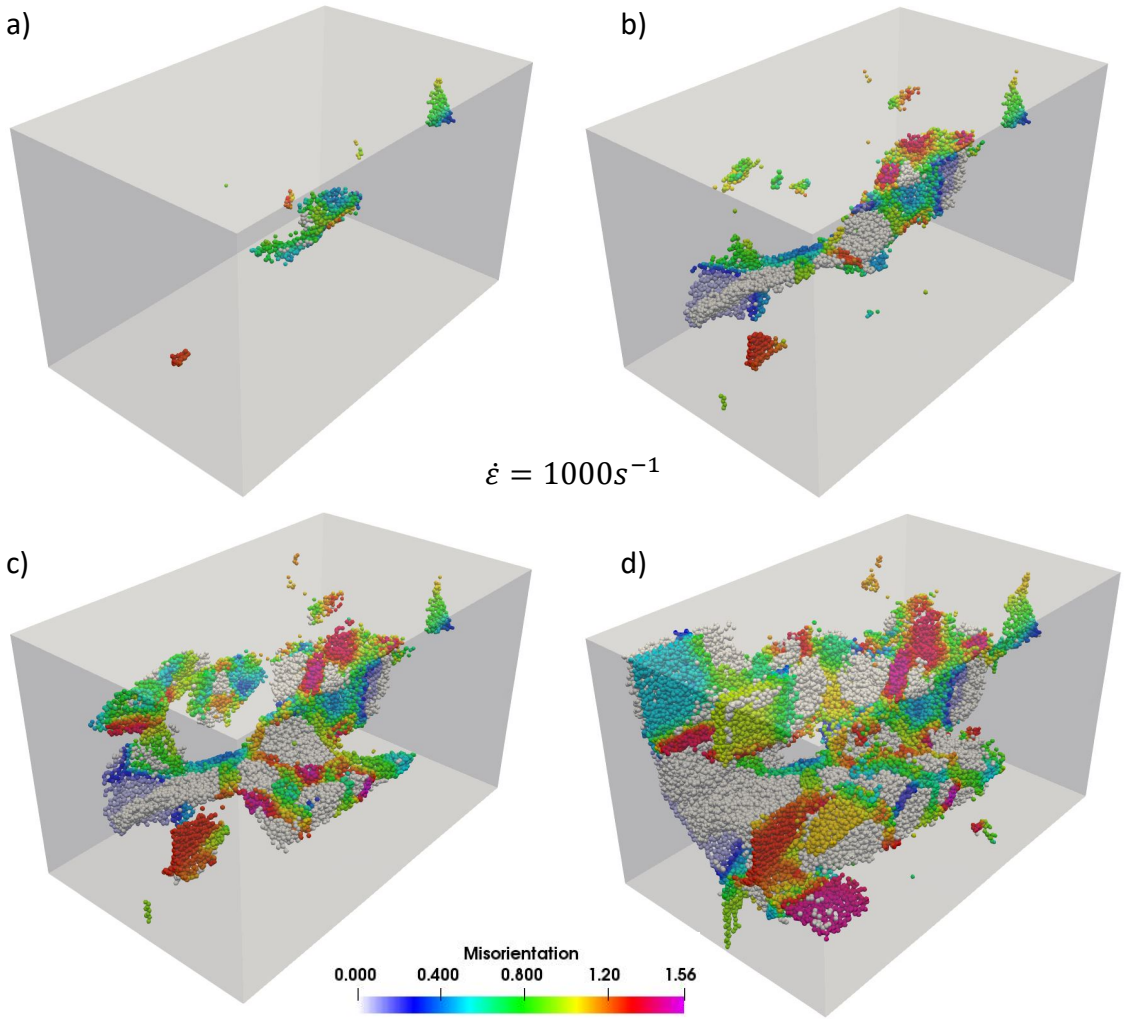

Fig. 5.14. Crack growth in the polycrystallne SiC sample under dynamic compression at strain rate $1000s^{-1}$: a)-d) are taken at uniformly-apart moments from when cracks first appear till the maximum stress is reached.

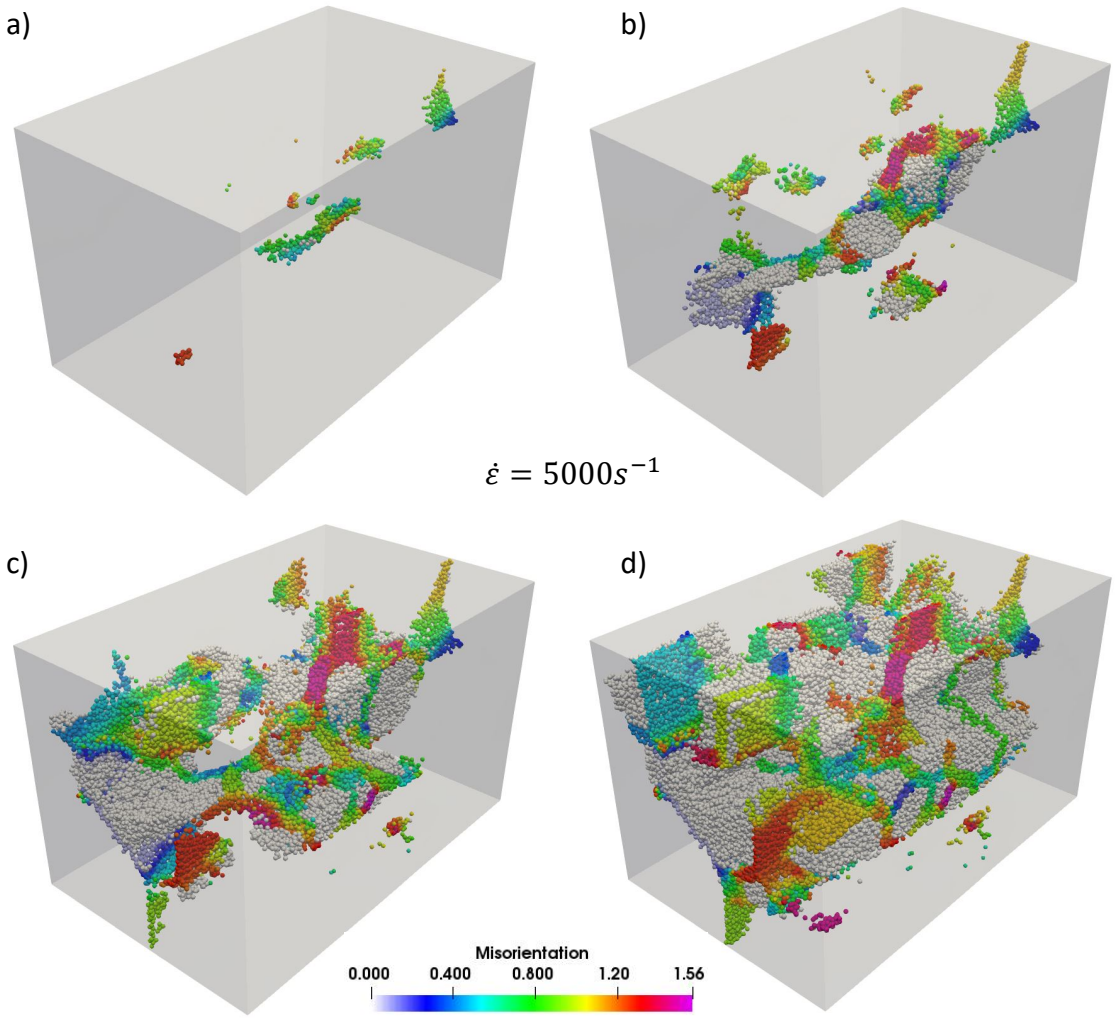

Fig. 5.15. Crack growth in the polycrystallne SiC sample under dynamic compression at strain rate $5000s^{-1}$: a)-d) are taken at uniformly-apart moments from when cracks first appear till the maximum stress is reached.

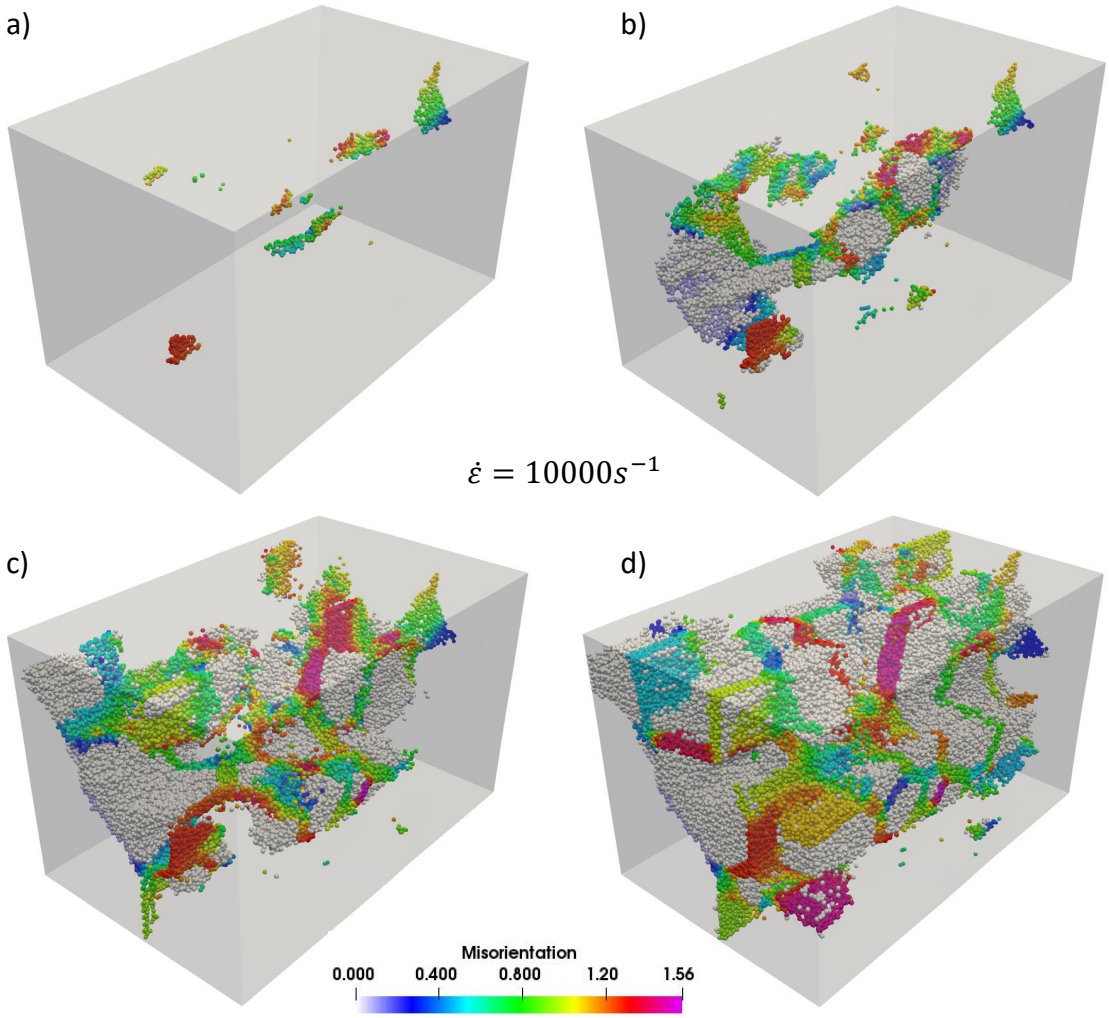

Fig. 5.16. Crack growth in the polycrystallne SiC sample under dynamic compression at strain rate $10000s^{-1}$: a)-d) are taken at uniformly-apart moments from when cracks first appear till the maximum stress is reached.

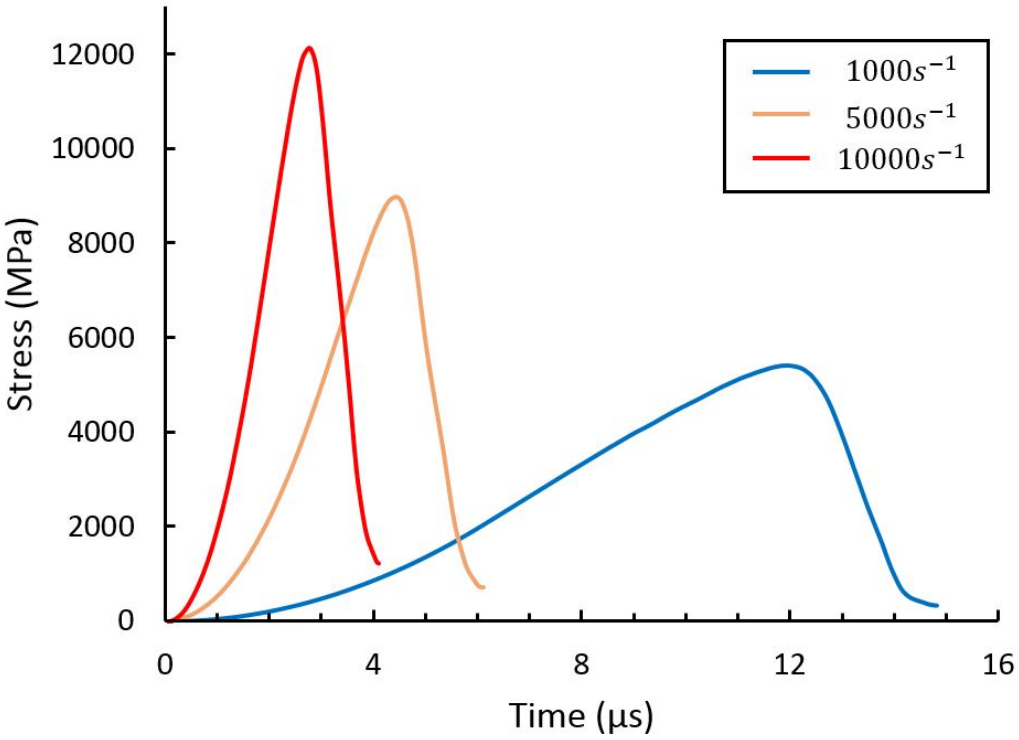

Fig. 5.17. The stress histories at strain rates of $1000s^{-1}$, $5000s^{-1}$ and $10000s^{-1}$.

strain rate dependency predicted by our model is a natural result of the competition between various energy dissipation pathways in the microstructure (i.e., intergranular and transgranular fractures).

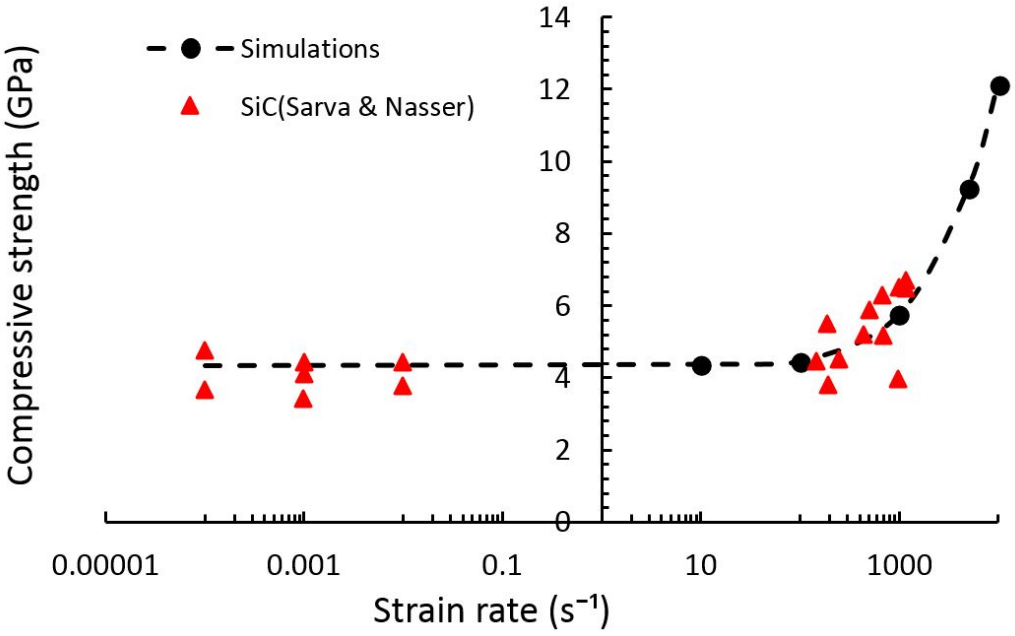

Fig. 5.13. Strain rate dependence of SiC predicted by the model in comparison with the experimental data.

In general, the ceramic material seeks the most effective pathways to dissipate the deposited energy. As a significant amount of energy deposit into the polycrystalline structure in a short time, a transgranular fracture is capable of converting more strain energy in the bulk material into surface energy than an intergranular fracture within a limited time frame, due to the limitation of the crack propagation speed constrained by the Rayleigh surface wave speed. For example, crack front propagation speed converges to 0.6 ~ 0.7 of the Rayleigh wave speed as observed in experimental studies[19,43,110]. Thus, a crack nucleated at the grain boundary may turn its direction towards the interior of grain in order to minimize the total energy of the system more efficiently. Fig. 5.18 demonstrates the volume fraction of failed grain boundaries and inner-grain material

points for strain rates at which the macroscopic strength of the material increases rapidly. The curve takes a record of the area of fracture surfaces from the beginning of loading till the failure point, i.e., the maximum stress point. At the beginning of the failure process, most of the fracture surfaces are inter-granular. As the stress builds up in the material, the volume fraction of the inter- and transgranular fracture surfaces increases linearly. At low strain rates, this trend continues until the material fails. However, as the strain rate is beyond 1000 s^{-1}, the volume fraction of fracture surfaces starts to grow exponentially after a certain stress level. Also, the rate of growth of transgranular fracture surfaces catches up and eventually exceeds the growth rate of intergranular fracture surfaces, which quantitatively demonstrates the preferred energy dissipation pathways of the ceramic material at high strain rates. The competition between inter- and transgranular fracture is also illustrated in Fig. 5.19. At a relatively low strain rate ($< 1000 s^{-1}$), the ratio between trans- and intergranular fracture is low and stable as shown in Fig. 5.19. The intergranular fracture is the dominant fracture mode leading to the failure point. There is a transition zone from $1000 s^{-1}$ to $5000 s^{-1}$ where the transgranular fracture becomes more and more common as the strain rate increases. The fracture mode switches from intergranular dominant towards transgranular dominant.

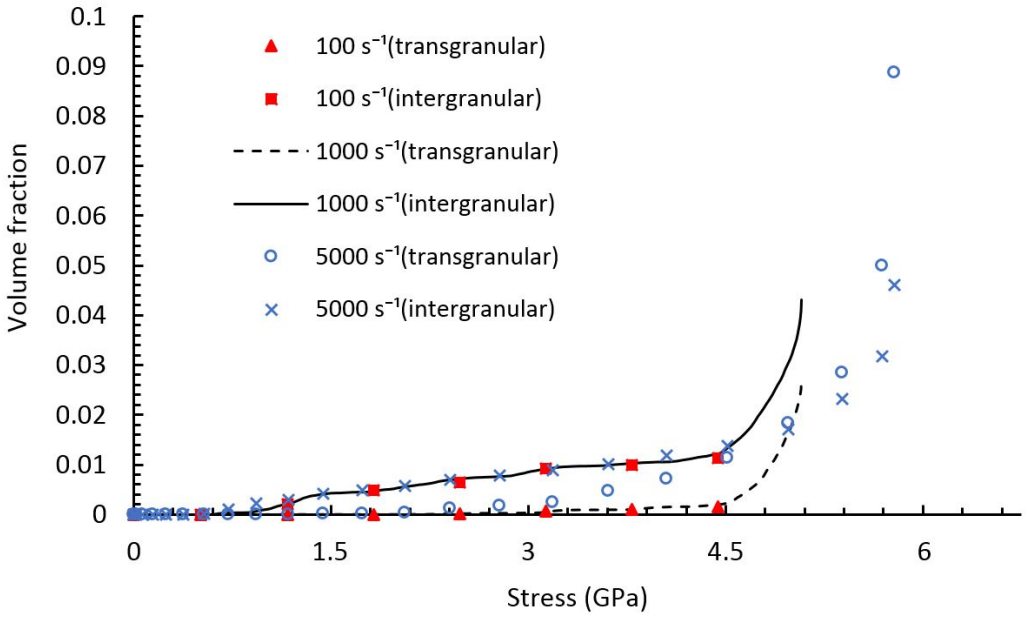

Fig. 5.18. The growing volume fraction of failed grain boundaries and inner-grain material points with the stress build-up under different strain rate.

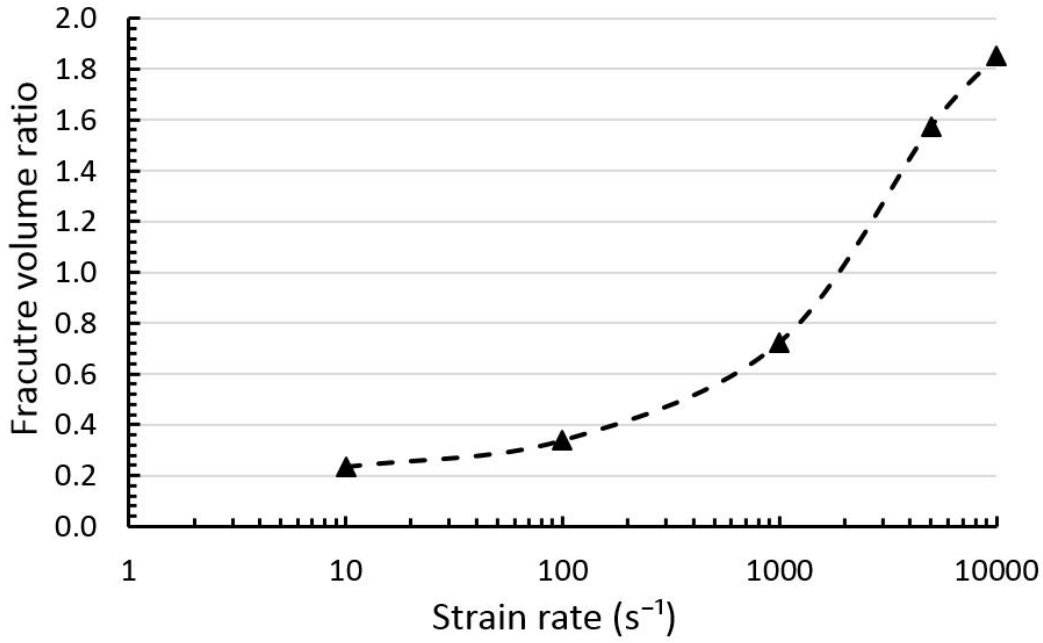

Fig. 5.19. Competition of trans- to inter- granular fractures at different strain rates.

5.2.5 Misorientation distribution

In the previous section, the influence of grain boundaries on the strain-rate dependent strength was investigated. The simulation shows the fracture usually initiates at the grain boundary with a large misorientation angle. This behavior corresponds to the critical energy release rate which is defined as a function of the misorientation angle. Clayton and Knap[28] performed a numerical study on the effects of crystal and grain boundary properties involving grain boundary networks and the anisotropic elasticity. However, the grain boundary properties defined in each simulation are homogeneous for all grain boundaries. With the polycrystalline reconstruction techniques presented in this work, we are able to include the heterogeneity of the grain boundary in terms of the misorientation distribution.

Here three misorientation distributions are tested using the same set of orientation angles. The grain structure is the same one used in the previous studies. It consists of 100 grains and 479 grain boundaries. Fig. 5.20 shows the misorientation distributions for two samples that follow the normal distributions with their peaks at 10 degree(low angle) and 60 degree(high angle), respectively. The normalized critical energy release rate is plotted as a function of misorientations in Fig. 5.21, which decreases with an increase in misorientation angle, which drops more quickly at lower misorientation angles and slows down at higher angles.

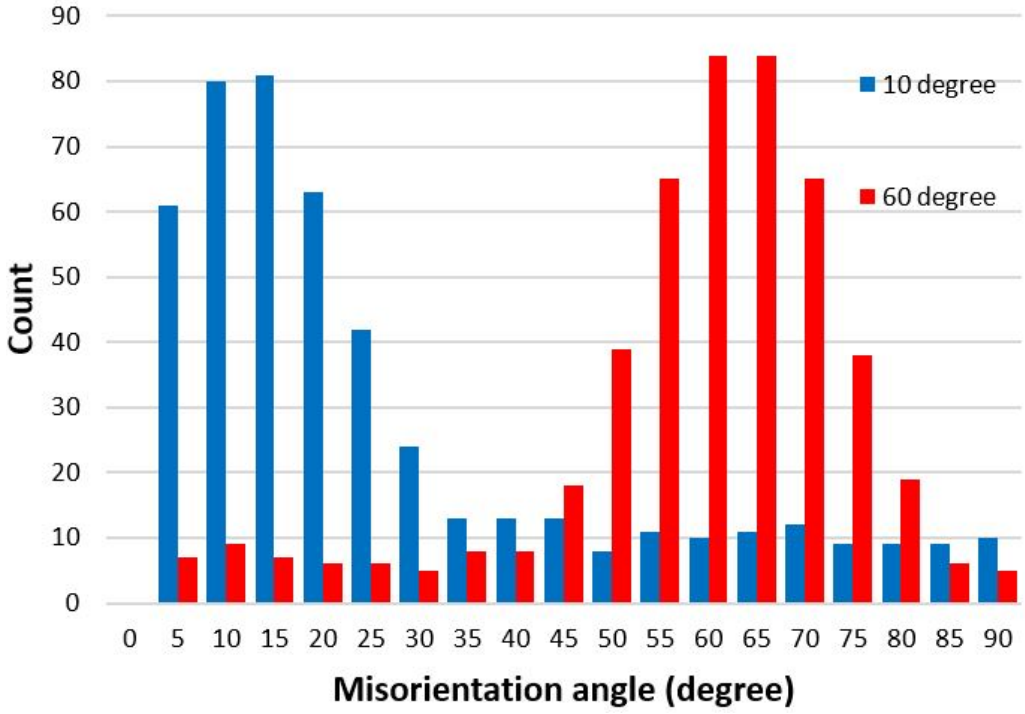

Fig. 5.20. Column: comparison of two misorentation distributions.

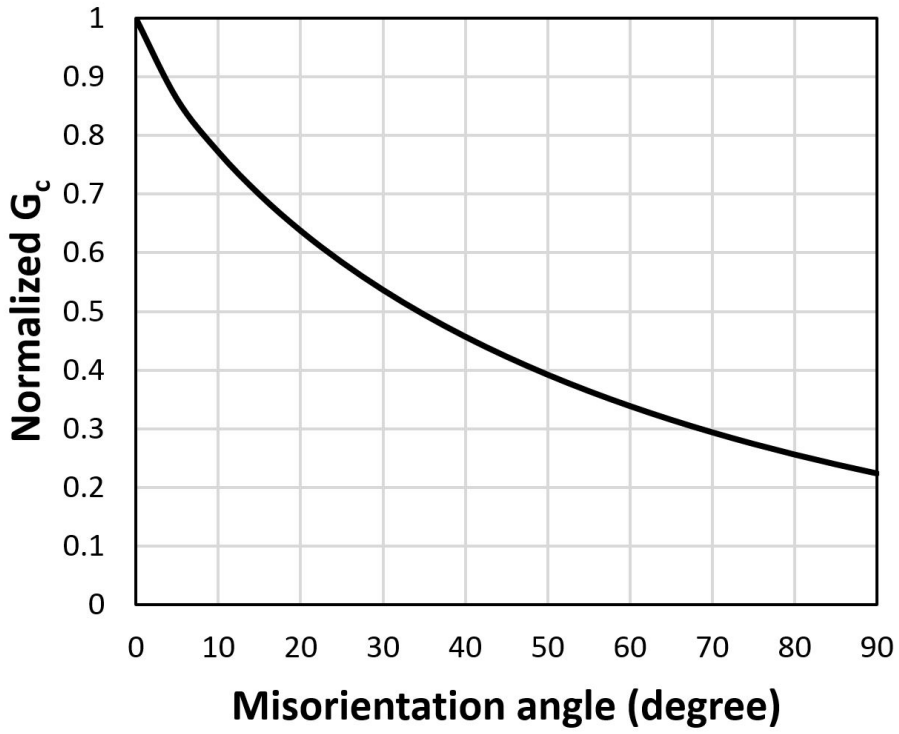

Fig. 5.21. The normalized critical energy release rate as a function of misorientation angles.

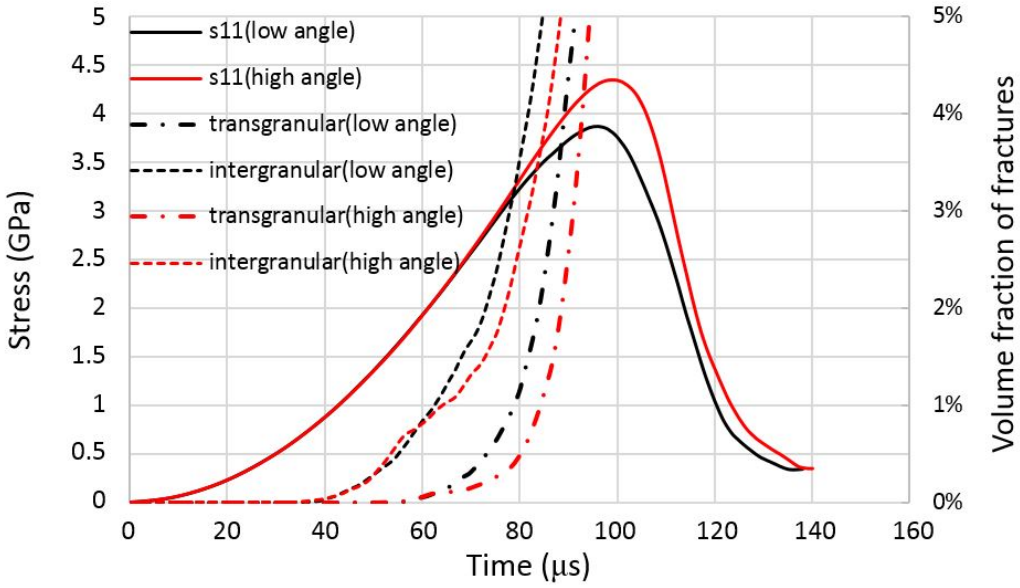

Fig. 5.22. Comparison of strength, transgranular fracture and intergranular fracture between two samples with different misorientation distributions.

The growth of trans- and intergranular fracture for two distributions is demonstrated in Figure 5.22, as well as the corresponding stress histories. Though the discrepancy of the critical energy release rate between two distributions is statistically large ($G_c^{gb}(10) = 70\% G_c^{grain}$ and $G_c^{gb}(60) = 30\% G_c^{grain}$), their stress histories are quite similar. The high angle distribution exhibits a slightly higher final strength than the other two. But it is impossible to draw a general prediction on the relationship between the misorientation distribution and the final strength based on the current results. More samples with different configurations(ODF and MODF) need to be systematically tested in order to derive a statistical conclusion.

5.3 Conclusion

The computational model is validated by directly comparing the predicted compressive strength of 6H-SiC at various strain rates against experimental measurements in the split-Hopkinson pressure bar (SHPB) tests. The mesh-independence of the algorithm is shown in the convergence study by refining the mesh of the polycrystalline structure in SHPB tests. Finally, a quantitative analysis of the influence of the microstructure on the dynamic compressive failure mechanisms of 6H-SiC, including porosity effect and strain-rate dependence, is performed thoroughly by using the proposed computational scheme.

The analysis demonstrates that the ultimate compressive strength of ceramic materials is determined by the competition and combination of intergranular and transgranular fractures in case of high energy density deposition in a short time. The model predicts that the intergranular fracture is dominant at low strain rates, but an increasing tendency for transgranular fracture has been observed as strain rate increases. In our simulations, the brittle polycrystalline material fails structurally once the vital longitudinal transgranular cracks connect all the locally distributed micro-cracks into a network and the material reaches its stress limit. The rate-dependence of the macroscopic fracture property of ceramic arises simply as a particular choice of the crack propagation path in the microstructure. In conventional modeling approaches, loading rate-dependent macroscopic fracture properties, such as the rate-dependent damage model, cohesive law or fracture toughness, are the critical postulate to predict the dynamic

compressive strength of ceramics. By contrast, the proposed computational framework assumes no rate-dependent material properties in the microstructure for strain rates lower than 10^7 s^{-1} and provides a detailed description of the interaction between transgranular and intergranular fractures. As a minimization problem of the total energy of the system, the model enables an automatic selection of the most effective energy dissipation pathways by integrating a topological defect dependent energy release rate function. The rate sensitivity of the macroscopic compressive strength becomes a natural outcome of the simulation, which also sheds light on a mechanistic understanding of the dynamic compressive failure mechanisms in ceramics. In addition, the predicted porosity-strength relation by the model matches well with the empirical models. Our analysis shows that the compressive strength of the material decreases with the increase of the porosity. In the study of ceramics with the different spatial distribution of voids, we also found that a higher percentage of voids at the grain boundaries promotes intergranular fractures and results in lower ultimate strength.

6 Conclusions and future works

We have developed a micromechanical computational framework for the direct meso-scale simulation of dynamic failure mechanisms in ceramics at high strain rates based on the Optimal Transportation Meshfree (OTM) method and the microstructure informed Eigen-fracture approach. The microstructural features, including the grain structure, grain boundaries, and voids, are modeled explicitly in the framework. In specific, a statistically equivalent polycrystal structure of ceramic materials to the experimental measurements (e.g., EBSD) is reconstructed by using the centroid Voronoi tessellation and Monte Carlo annealing algorithm to match the probability distribution functions of the grain size, grain orientation and grain boundary misorientation (or texture). The crystal elasticity model with damage is employed to predict the anisotropic dynamic response of the polycrystalline structure. Interactions between the crack front and the microstructure during the dynamic failure process is indicated in the model by considering the equivalent energy release rate as a function of the local micro-features, such as the grain boundary misorientation angle and the void volume fraction.

The proposed model is validated for both two- and three-dimensional modelings. The two-dimensional modeling is validated by comparing the predicted failure process

of polycrystalline graphene under tension against the results from Molecular Dynamic simulations, while three-dimensional modeling is validated by directly comparing the predicted compressive strength of 6H-SiC at various strain rates against experimental measurements in the split-Hopkinson pressure bar (SHPB) tests.

In conclusion, the proposed computational framework furnishes an effective means of modeling dynamic failure processes in 2D/3D polycrystalline materials under various loading conditions and predicting several primary physical phenomena related to brittle fractures such as strain rate effect, influence of porosity and its distribution. There are still several aspects can be improved in future work.

- The plasticity has not been concerned in our model due to the complexity of dislocation dynamics in polycrystalline structures, especially at the grain boundaries. Therefore, the plasticity-related phenomenons, such as grain size effect and fatigue, cannot be studied by using the current computational framework. Future work will focus on introducing the crystal plasticity model to describe the dynamic response of material points at the interior of grains and on the grain boundaries to study the influence of the competition between plasticity and fracture of the ultimate strength of the material.
- In the study regarding the influence misorientation distribution, the number of numerical tests are not sufficient enough to draw any statistical conclusions. More samples with different configurations should be tested while the spatial distribution of the misorientations should also be included as a variant in this study.

- In order to capture more accurate fracture features, the critical energy release rate for different microstructures in different crystal systems need to be characterized as a function of implementable parameters in the mesoscale. This can be done using first principle calculations.
- Dynamic adaptive mesh refinement would be a great technique to boost the accuracy and effectiveness of the proposed model. However, there are still many difficulties, especially in three-dimensional models.

Complete References

[1] A Abdollahi and I Arias. Numerical simulation of intergranular and transgranular crack propagation in ferroelectric polycrystals. Int J Fract, 174:3–15, 2012.

[2] Deji Akinwande, Christopher J. Brennan, J Scott Bunch, Philip Egberts, Jonathan R Felts, Huajian Gao, Rui Huang, Joon Seok Kim, Teng Li, Yao Li, Kenneth M Liechti, Nanshu Lu, Harold S Park, Evan J Reed, Peng Wang, Boris I Yakobson, Teng Zhang, Yong Wei Zhang, Yao Zhou, and Yong Zhu. A review on mechanics and mechanical properties of 2d materials-graphene and beyond. Extreme Mechanics Letters, 13: 42–77, 2017.

[3] Fadi Aldakheel, BlaÅ¿ Hudobivnik, Ali Hussein, and Peter Wriggers. Phase-field modeling of brittle fracture using an efficient virtual element scheme. Computer Methods in Applied Mechanics and Engineering, 341:443 – 466, 2018.

[4] H Amor, J-J Marigo, and C Maurini. Regularized formulation of the variational brittle fracture with unilateral contact: Numerical experiments. Journal of the Mechanics and Physics of Solids, 57:1209–1229, 2009.

[5] F Armero and K Garikipati. An analysis of strong discontinuities in multiplicative finite strain plasticity and their relation with the numerical simulation of strain localization in solids. International Journal of Solids and Structures, 33:2863–2885, 1996.

[6] Marino Arroyo and Michael Ortiz. Local maximum-entropy approximation schemes: a seamless bridge between finite elements and meshfree methods. Internat. J. Numer. Methods Engrg., 65(13):2167–2202, 2006.

[7] KT Aust, U Erb, and G Palumbo. Interface control for resistance to intergrangular cracking. Materials Science and Engineering A, 176:329–334, 1994.

[8] Sukang Bae, Hyeongkeun Kim, Youngbin Lee, Xiangfan Xu, Jae-Sung Park, Yi Zheng, Jayakumar Balakrishnan, Tian Lei, Hye Ri Kim, Young Il Song, Young-Jin Kim, Kwang S Kim, Barbaros özyilmaz, Jong-Hyun Ahn, Byung Hee Hong, and Sumio Iijima. Roll-to-roll production of 30-inch graphene films for transparent electrodes. Nature Nanotechnology, 5:574–578, 2010.

[9] M.Y. Bal'shin. Relation of mechanical properties of powder metals and their porosity and the ultimate properties of porous metal-ceramic materials. Dokl. Akad. Nauk SSSR, 67:831–834, 1949.

[10] PD Beale and DJ Srolovitz. Elastic fracture in random materials. Physics Review B, 37(10):5500–5507, 1998.

[11] T Belytschko, J Fish, and BE Engelmann. A finite element with embedded localization zones. Computer Methods in Applied Mechanics and Engineering, 70:59–89, 1988.

[12] I. Benedetti and M. H. Aliabadi. A three-dimensional cohesive-frictional grain-boundary micromechanical model for intergranular degradation and failure in polycrystalline materials. computer methods. Applied Mechanics and Engineering, 265:36–62, 2013.

[13] S Bertolazzi, J Brivio, and A Kis. Stretching and breaking of ultrathin mos_2. ACS Nano, 5:9703–9709, 2011.

[14] K. Bhattacharya, M. Ortiz, and G. Ravichandran. Energy-based model of compressive splitting in heterogeneous brittle solids. Journal of the Mechanics and Physics of Solids, 46(10):2171 – 2181, 1998.

[15] Kaushik Bhattacharya. Energy minimization and nonlinear problems in polycrystalline solids. In Computer-aided Design of High-temperature Materials, page 139. Oxford University Press on Demand, 1999.

[16] Jeremy Bleyer and Roberto Alessi. Phase-field modeling of anisotropic brittle fracture including several damage mechanisms. Computer Methods in Applied Mechanics and Engineering, 336:213 – 236, 2018.

[17] JE Bolander Jr and S. Saito. Fracture analyses using spring networks with random geometry. Engineering Fracture Mechanics, 61:569–591, 1998.

[18] Michael J. Borden, Clemens V. Verhoosel, Michael A. Scott, Thomas J.R. Hughes, and Chad M. Landis. A phase-field description of dynamic brittle fracture. Computer Methods in Applied Mechanics and Engineering, 217-220:77–95, 2012.

[19] J. F. Boudet, S. Ciliberto, and V. Steinberg. Experimental study of the instability of crack propagation in brittle materials. EPL (Europhysics Letters), 30(6):337, 1995.

[20] Blaise Bourdin, Gilles A Francfort, and Jean-Jacques Marigo. Numerical experiments in revisited brittle fracture. Journal of the Mechanics and Physics of Solids, 48:797–826, 2000.

[21] Blaise Bourdin, Gilles A Francfort, and Jean-Jacques Marigo. The variational approach to fracture. Springer, 2008.

[22] G T Camacho and M Ortiz. Computational modelling of impact damage in brittle materials. International Journal of Solids and Structures, 33(20):2899–2938, 1996.

[23] A Castellanos-Gomez, M Poot, G A Steele, H S J van der Zant, N AgraÃŕt, and G Rubio-Bollinger. Elastic properties of freely suspended mos_2 nanosheets. Advanced Materials, 24:772–775, 2012.

[24] P.G. Charalambides and R.M. McMeeking. Finite element method simulation of crack propagation in a brittle microcracking solid. Mechanics of Materials, 6(1): 71–87, 1987.

[25] M.Q. Chen, S.S. Quek, Z.D. Sha, C.H. Chiu, Q.X. Pei, and Y.W. Zhang. Effects of grain size, temperature and strain rate on the mechanical properties of polycrystalline graphene - a molecular dynamics study. Carbon, 85:135–146, 2015.

[26] W Chen and G Ravichandran. Failure mode transition in ceramics under dynamic multiaxial compression. International Journal of Fracture, 101(1):141–159, 2000.

[27] Weinong Chen and G. Ravichandran. Static and dynamic compressive behavior of aluminum nitride under moderate confinement. Journal of the American Ceramic Society, 79(3):579–584, 1996.

[28] J. D. Clayton and J. Knap. Phase field modeling of directional fracture in anisotropic polycrystals. Computational Materials Science, 98:158–169, 2015.

[29] J.D. Clayton and J. Knap. Phase field modeling and simulation of coupled fracture and twinning in single crystals and polycrystals. Computer Methods in Applied Mechanics and Engineering, 312:447 – 467, 2016.

[30] WA Curtin and H. Scher. Brittle fracture of disordered materials. Journal of Materials Research, 5(3):535–553, 1990.

[31] WA Curtin and H. Scher. Mechanics modeling using a spring network. Journal of Materials Research, 5(3):554–562, 1990.

[32] Nitin P. Daphalapurkar, K.T. Ramesh, Lori Graham-Brady, and Jean-Francois Molinari. Predicting variability in the dynamic failure strength of brittle materials considering pre-existing flaws. Journal of the Mechanics and Physics of Solids, 59(2): 297–319, 2011.

[33] G Del Piero, G Lancioni, and R March. A variational model for fracture mechanics: numerical experiments. J Mech Phys Solids, 55:2513âĂŞ2537, 2007.

[34] J. M. J. den Toonder, J. A. W. van Dommelen, and F. P. T. Baaijens. The relation between single crystal elasticity and the effective elastic behaviour of polycrystalline

materials: theory, measurement and computation. Modelling and Simulation in Materials Science and Engineering, 7(6):909–928, 1999.

[35] Q Du and M Gunzburger. Grid generation and optimization based on centroidal voronoi tessellations. Applied Mathematics and Computation, 133:591–607, 2002.

[36] Q Du, M Gunzburger, and L Ju. Meshfree, probabilistic determination of point sets and support regions for meshless computing. Computer Methods in Applied Mechanics and Engineering, 191:1349–1366, 2002.

[37] Qiang Du, Vance Faber, and Max Gunzburge. Centroidal voronoi tessellations: Applications and algorithms. SIAM Review, 41(4):637–676, 1999.

[38] EN Dvorkin, AM Cuiti*ñ*o, and G Gioia. Finite elements with displacement interpolated embedded localization lines insensitive to mesh size and distortions. International Journal for Numerical Methods in Engineering, 30:541–564, 1990.

[39] L Eastgate, J Sethna, M Rauscher, and T Cretegny. Fracture in mode i using a conserved phase-field model. Phys Rev E, 65(36):117, 2002.

[40] H. D. Espinosa and P. D. Zavattieri. A grain level model for the study of failure initiation and evolution in polycrystalline brittle materials. part i: Theory and numerical implementation. Mechanics of Materials, 35(3):333–364, 2003.

[41] M L Falk, A Needleman, and Rice J R. A critical evaluation of cohesive zone models of dynamic fracture. Journal of Physics, 11:43–50, 2001.

[42] A Fallahi and A Ataee. Effects of crystal orientation on stress distribution near the triple junction in a tricrystal γ -tial. Materials Science and Engineering: A, 527(18): 4576 – 4581, 2010.

[43] Jay Fineberg, Steven P. Gross, M. Marder, and Harry L. Swinney. Instability in the propagation of fast cracks. Phys. Rev. B, 45:5146–5154, 1992.

[44] F Fritzen, T B*ö*hlke, and E Schnack. Periodic three-dimensional mesh generation for crystalline aggregates based on voronoi tessellations. Computational Mechanics, 43:701–713, 2009.

[45] S Ghosh and L Yunshan. Voronoi cell finite element model based on micropolar theory of thermoelasticity for heterogeneous materials. International Journal of Numerical Methods and Engineering, 38:1361–1368, 1995.

[46] S. Ghosh, Z Nowak, and K Lee. Tessellation-based computational methods for the characterization and analysis of heterogeneous microstructure. Composite Science and Technology, 57:1187–1210, 1997.

[47] A A Griffith. The phenomena of rupture and flow in solids. Philosophical Transactions, Series A, 221:163–198, 1920.

[48] V Hakim and A Karma. Laws of crack motion and phase-field models of fracture. J Mech Phys Solids, 57:342âĂŞ368, 2009.

[49] P J Hazell. Measuring the strength of brittle materials by depth-of-penetration testing. Advances in Applied Ceramics, 109(8):504–510, 2010.

[50] M Hofacker and C Miehe. Continuum phase field modeling of dynamic fracture: variational principles and staggered fe implementation. Int J Fract, 178: 113âĂŞ129, 2012.

[51] Chance C. Holland and Robert M. McMeeking. The influence of mechanical and microstructural properties on the rate-dependent fracture strength of ceramics in uniaxial compression. International Journal of Impact Engineering, 81:34–49, 2015.

[52] EA. Holm. Surface formation energy for intergranular fracture in two-dimensional polycrystals. Journal of the American Ceramic Society, 81(3):455–459, 1998.

[53] Guangli Hu, K T Ramesh, Buyang Cao, and J W McCauley. The compressive failure of aluminum nitride considered as a model advanced ceramic. Journal of the Mechanics and Physics of Solids, 59(5):1076–1093, 2011.

[54] Guangli Hu, C Q Chen, K T Ramesh, and J W McCauley. Mechanisms of dynamic deformation and dynamic failure in aluminum nitride. Acta Materialia, 60(8): 3480–3490, 2012.

[55] C E Inglis. Stresses in plates due to the presence of cracks and sharp corners. Transactions of the Institute of Naval Architects, 55:219–241, 1913.

[56] G R Irwin. Fracture dynamics. Fracturing of Metals, American Society for Metals, pages 147–166, 1948.

[57] A Jagota and SJ Bennison. Spring-network and finite-element models for elasticity and fracture. In Nonlinearity and Breakdown in Soft Condensed Matter, Springer Lecture Notes, volume 437, pages 186–201. Springer Berlin, 1994.

[58] A Jagota and SJ Bennison. Element breaking rules in computational models for brittle fracture. Modelling and Simulation in Materials Science and Engineering, 3 (4):485–501, 1995.

[59] Y Jin, Y Wang, and A Khachaturyan. Three-dimensional phase field microelasticity theory and modeling of multiple cracks and voids. Appl Phys Lett, 79: 3071âĂŞ3073, 2001.

[60] M Jirasek. Comparative study on finite elements with embedded discontinuities. Computer Methods in Applied Mechanics and Engineering, 188:307–330, 2000.

[61] G Jung, Z Qin, and Buehler M J. Molecular mechanics ofpolycrystalline graphene with enhanced fracture toughness. Extreme Mech. Lett., 2:52–59, 2015.

[62] Roopam Khare, Steven L Mielke, Jeffrey T Paci, Sulin Zhang, Roberto Ballarini, George C Schatz, , and Ted Belytschko. Coupled quantum mechanical/molecular mechanical modeling of the fracture of defective carbon nanotubes and graphene sheets. Phys. Rev. B., 75:075412, 2007.

[63] Kawahara M. Kim B-N, Wakayama S. Characteristics of 2-dimensional crack propagation behavior by simulation and analysis. International Journal of Fracture, 75: 247–259, 1996.

[64] P.A. Klein, J.W. Foulk, E.P. Chen, S.A. Wimmer, and H.J. Gao. Physics-based modeling of brittle fracture: cohesive formulations and the application of meshfree methods. Theoretical and Applied Fracture Mechanics, 37(1):99–166, 2001.

[65] Markus Klinsmann, Daniele Rosato, Marc Kamlah, and Robert M. McMeeking. An assessment of the phase field formulation for crack growth. Computer Methods in Applied Mechanics and Engineering, 294:313 – 330, 2015.

[66] J. Knap and J. D. Clayton. A geometrically nonlinear phase field theory of brittle fracture. International Journal of Fracture, 189(2):139–148, 2014.

[67] C Kuhn and R Muller. A continuum phase field model for fracture. Eng Fract Mech, 77:3625âĂŞ3634, 2010.

[68] M Kumar, WE King, and AJ Schwartz. Modifcations to the microstructural topology in f.c.c. materials through thermomechanical processing. Acta Materialia, 48 (9):2081–2091, 2000.

[69] C J Larsen, M Ortiz, and C L Richardson. Fracture paths from front kinetics : relaxation and rate independence. Archive for Rational Mechanics and Analysis, 193 (3):539–583, 2009.

[70] R Larsson, P Steinmann, and K Runesson. Finite element embedded localization band for finite strain plasticity based on a regularized strong discontinuity. Mechanics of Cohesive-frictional Materials, 4(2):171–194, 1999.

[71] C. Lee, X. D. Wei, J. W. Kysar, and J. Hone. Measurement of the elastic properties and intrinsic strength of monolayer graphene. Science, 321:385–388, 2008.

[72] G-H Lee, R C Cooper, S J An, S Lee, A van der Zande, N Petrone, A G Hammerberg, C Lee, B Crawford, W Oliver, J W Kysar, and J Hone. High strength chemical vapor deposited graphene and grain boundaries. Science, 340:1073–1076, 2013.

[73] Jae-Hwang Lee, Phillip E. Loya, Jun Lou, and Edwin L. Thomas. Dynamic mechanical behavior of multilayer graphene via supersonic projectile penetration. Science, 346:1092–1096, 2014.

[74] B Li, F Habbal, and M Ortiz. Optimal transportation meshfree approximation schemes for fluid and plastic flows. Internat. J. Numer. Methods Engrg., 83(12), 2010.

[75] B. Li, A. Kidane, G. Ravichandran, and M Ortiz. Verification and validation of the optimal transportation meshfree (otm) simulation of terminal ballistics. International Journal of Impact Engineering, 42:25–36, 2012.

[76] B Li, A Pandolfi, and M Ortiz. Material-point erosion simulation of dynamic fragmentation of metals. Mechanics of Materials, 80:288–297, 2015.

[77] Li Li and Michel Aubertin. A general relationship between porosity and uniaxial strength of engineering materials. Canadian Journal of Civil Engineering, 30(4): 644–658, 2003.

[78] Q M Li. Strain energy density failure criterion. International Journal of Solids and Structures, 38(38):6997–7013, 2001.

[79] Y Liu, Y Kegayama, and S Murakami. Creep fracture modeling by use of continuum damage variable based on voronoi simulation of grain boundary cavity. International Journal of the Mechancis of Science, 40:147–158, 2008.

[80] Spandan Maiti, Krishnan Rangaswamy, and Philippe H. Geubelle. Mesoscale analysis of dynamic fragmentation of ceramics under tension. Acta Materialia, 53(3): 823–834, 2005.

[81] Robert J. McCann. A convexity principle for interacting gases. Advances in Mathematics, 128(1):153 – 179, 1997.

[82] S A Meguid, A R Alian, and M A N Dewapriya. Atomistic modelling of nanoindentation of multilayered graphene-reinforced nanocomposites. In Micromechanics and Nanomechanics of Composite Solids. Springer Cham, 2018.

[83] C Miehe, M Hofacker, and F Welschinger. A phase field model for rate-independent crack propagation: Robust algorithmic implementation based on operator splits. Comput. Methods Appl. Mech. Eng., 199:2765–2778, 2010.

[84] Alexander Mielke and Michael Ortiz. A class of minimum principles for characterizing the trajectories and the relaxation of dissipative systems. ESAIM: Control, Optimisation and Calculus of Variations, 14(3):494–516, 2008.

[85] Matteo Negri. A finite element approximation of the griffith's model in fracture mechanics. Numerische Mathematik, 95(4):653–687, 2003.

[86] S. Nemat-Nasser and H. Deng. Strain-rate effect on brittle failure in compression. Acta Metallurgica et Materialia, 42(3):1013–1024, 1994.

[87] Parag G. Nittur, Spandan Maiti, and Philippe H. Geubelle. Grain-level analysis of dynamic fragmentation of ceramics under multi-axial compression. Journal of the Mechanics and Physics of Solids, 56(3):993–1017, 2008.

[88] K S Novoselov, Jiang D, F Schedin, T J Booth, V V Khotkevich, S V Morozov, and A K Geim. Two-dimensional atomic crystals. Proc. Natl Acad. Sci., 102:10451–10453, 2005.

[89] K S Novoselov, V I Fal'Ko, L Colombo, P R Gellert, M G Schwab, and K Kim. A roadmap for graphene. Nature, 490:192–200, 2012.

[90] Atsuyuki Okabe, Barry Boots, Kokichi Sugihara, Sung Nok Chiu, and D. G. Kendall. Spatial Tessellations: Concepts and Applications of Voronoi Diagrams. 2000.

[91] E Orowan. Fracture and strength of solids. Reports on Progress in Physics, 12:185, 1948.

[92] M. Ortiz and A. Pandolfi. Finite-deformation irreversible cohesive elements for three-dimensional crack-propagation analysis. International Journal for Numerical Methods in Engineering, 44(9):1267–1282, 1999.

[93] M Ortiz, Y Leroy, and A Needleman. A finite element method for localized failure analysis. Computer Methods in Applied Mechanics and Engineering, 61:189–214, 1987.

[94] Michael Ortiz and Laurent Stainier. The variational formulation of viscoplastic constitutive updates. Computer Methods in Applied Mechanics and Engineering, 171(3-4):419–444, 1999.

[95] A. Pandolfi and M. Ortiz. An eigenerosion approach to brittle fracture. International Journal for Numerical Methods in Engineering, 92(8):694–714, 2012.

[96] T L Paxson, R A Lucas, B Broberg, and A R Kobayashi, A amd Rosenfield. An experimental investigation of the velocity characteristics of a fixed boundary fracture model. In Proceedings of an international conference on Dynamic Crack Propagation. Springer Dordrecht, 1973.

[97] V Péron-lührs, A Jérusalem, F Sansoz, L Stainier, and L Noels. A two-scale model predicting the mechanical behavior of nanocrystalline solids. Journal of the Mechanics and Physics of Solids, 61(9):1895–1914, 2013.

[98] R Quey, P R Dawson, and F Barbe. Large-scale 3d random polycrystals for the finite element method : Generation, meshing and remeshing. Computer Methods in Applied Mechanics and Engineering, 200(17):1729–1745, 2011.

[99] K. T. Ramesh. High rates and impact experiments. In Springer Handbook of Experimental Solid Mechanics, pages 929–960. Springer US, 2008.

[100] Haider I. Rasool, Colin Ophus, William S. Klug, A. Zettl, and James K. Gimzewski. Measurement of the intrinsic strength of crystalline and polycrystalline graphene. Nature Communications, 4:1–7, 2013.

[101] G. Ravichandran and G. Subhash. A micromechanical model for high strain rate behavior of ceramics. International Journal of Solids and Structures, 32(17):2627–2646, 1995.

[102] RA Regueiro and RI Borja. Plane strain finite element analysis of pressure sensitive plasticity with strong discontinuity. International Journal of Solids and Structures, 38(21):3647–3672, 2001.

[103] Gonzalo Ruiz, Michael Ortiz, and Anna Pandolfi. Three-dimensional finite-element simulation of the dynamic brazilian tests on concrete cylinders. International Journal for Numerical Methods in Engineering, 48(7):963–994, 2000.

[104] J Ruppert. A delaunay refinement algorithm for quality 2-dimensional mesh generation. Journal of Algorithms, 18:548–585, 1995.

[105] Eugene Ryshkewitch. Compression strength of porous sintered alumina and zirconia. Journal of the American Ceramic Society, 36(2):65–68, 1953.

[106] Sai Sarva and Sia Nemat-Nasser. Dynamic compressive strength of silicon carbide under uniaxial compression. Materials Science and Engineering:A, 317(1): 140–144, 2001.

[107] David M. Saylor, Joseph Fridy, Bassem S. El-Dasher, Kee-Young Jung, and Anthony D. Rollett. Statistically representative three-dimensional microstructures based on orthogonal observation sections. Metallurgical and Materials Transactions A, 35(7):1969–1979, 2004.

[108] Bernd Schmidt, Fernando Fraternali, and Michael Ortiz. Eigenfracture: an eigendeformation approach to variational fracture. Multiscale Model. Simul., 7(3): 1237–1266, 2009.

[109] G. K. Sfantos and M. H. Aliabadi. Aboundary cohesive grain element formulation formodelling intergranularmicrofracture in polycrystalline brittle. International Journal for Numerical Methods in Engineering, 69(8):1590–1626, 2007.

[110] E. Sharon and J. Fineberg. The dynamics of fast fracture. Advanced Engineering Materials, 1(2):119–122, 1999.

[111] A Shekhawat and Ritchie R O. Toughness and strength of nanocrystalline graphene. Nature Communication, 7:10546, 2016.

[112] JC Simo and J Oliver. Modelling strong discontinuities in solid mechanics by means of strain softening constitutive equations. Computational Modelling of Concrete Structures, pages 363–372, 1994.

[113] JC Simo, J Oliver, and Armero F. An. An analysis of strong discontinuities induced by strain softening in rate- independent inelastics solids. Computational Mechanics, 12:277–296, 1993.

[114] LJ Sluys and AH Berends. Discontinuous failure analysis for mode-i and mode-ii localization problems. International Journal of Solids and Structures, 35:4257–4274, 1998.

[115] G. Subhash and G. Ravichandran. Mechanical behaviour of a hot pressed aluminum nitride under uniaxial compression. Journal of Materials Science, 33(7): 1933–1939, 1998.

[116] N. Sukumar, D. J. Srolovitz, T. J. Baker, and J. H. PrÃl'vost. Brittle fracture in polycrystalline microstructures with the extended finite element method. International Journal for Numerical Methods in Engineering, 56(14):2015–2037, 2003.

[117] Sachin S. Terdalkar, Shan Huang, Hongyan Yuan, Joseph J. Rencis, Ting Zhu, and Sulin Zhang. Nanoscale fracture in graphene. Chemical Physics Letters, 494(4):218 – 222, 2010.

[118] Cédric Villani. Topics in optimal transportation. Number 58. American Mathematical Soc., 2003.

[119] Hong Wang and K. T. Ramesh. Dynamic strength and fragmentation of hot-pressed silicon carbide under uniaxial compression. Acta Materialia, 52(2):355–367, 2004.

[120] T. Watanabe. The impact of grain boundary character distribution on fracture in polycrystals. Materials Science and Engineering A, 176:39–49, 1994.

[121] Yujie Wei, Jiangtao Wu, Hanqing Yin, Xinghua Shi, Ronggui Yang, and Mildred Dresselhaus. The nature of strength enhancement and weakening by pentagon-heptagon defects in graphene. Nature Mater., 11:759–763, 2012.

[122] Mei Xu, Alireza Tabarraei, Jeffrey T. Paci, Jay Oswald, and Ted Belytschko. A coupled quantum/continuum mechanics study of graphene fracture. Int. J. Fract., 173:163–173, 2012.

[123] X P Xu and A Needleman. Void nucleation by inclusion debonding in a crystal matrix. Modelling and Simulation in Materials Science and Engineering, 1(2):111–132, 1993.

[124] X P Xu and A Needleman. Numerical simulations of fast crack growth in brittle solids. Journal of the Mechanics and Physics of Solids, 42:1397–1434, 1994.

[125] B I Yakobson and Ding F. Observational geology of graphene. ACS Nano, 5:1569–1574, 2011.

[126] WH Yang, DJ Srolovitz, GN Hassold, and Anderson MP. Microstructural effects in the fracture of brittle materials. Simulation and Theory of Evolving Microstructures, pages 277–284, 1990.

[127] Lijun Yi, Zhengnan Yin, Yingyan Zhang, and Tienchong Chang. A theoretical evaluation of the temperature and strain-rate dependent fracture strength of tilt grain boundaries in graphene. Carbon, 51:373–380, 2013.

[128] P. D. Zavattieri and H. D. Espinosa. Grain level analysis of crack initiation and propagation in brittle materials. Acta Materialia, 49(20):4291–4311, 2001.

[129] P. D. Zavattieri, P. V. Raghuram, and H. D. Espinosa. Computational model of ceramic microstructures subjected to multi-axial dynamic loading. Journal of the Mechanics and Physics of Solids, 49(1):27–68, 2001.

[130] J Zhai and M Zhou. Finite element analysis of micromechanical failure modes in a heterogeneous ceramic material system. International Journal of Fracture, 101: 161–180, 2000.

[131] P. Zhang, D. Balint, and J. Lin. Controlled poisson voronoi tessellation for virtual grain structure generation : a statistical evaluation. Philosophical Magazine, 91 (36):4555–4573, 2011.

[132] Peng Zhang, Lulu Ma, Feifei Fan, Zhi Zeng, Cheng Peng, Phillip E. Loya, Zheng Liu, Yongji Gong, Jiangnan Zhang, Xingxiang Zhang, Pulickel M. Ajayan, Ting Zhu, and Jun Lou. Fracture toughness of graphene. Nature Communications, 5:1–7, 2014.

[133] Teng Zhang, Xiaoyan Li, Sara Kadkhodaei, and Huajian Gao. Flaw insensitive fracture in nanocrystalline graphene. Nano Lett., 12:4605–4610, 2012.

[134] Huijuan Zhao. Temperature and strain-rate dependent fracture strength of graphene. Journal of Applied Physics, 108:064321, 2010.